

IISc Theses Abstracts

Contents

A specification environment for distributed real-time systems	Rajib Mall	203
Finite element analysis of heat transfer and fluid flow in laser melting and solidification	K. Ravindran	205
Study of some artificial intelligence paradigms for partial discharge pattern recognition	L. Satish	207
Flexure of laminated composite plates—New refined lamination-dependent shear deformation models	Kesari Jawahar	209
Informational asymmetry in agency, bargaining and market contexts	P. Guruswamy Babu	211
Breakage and coalescence of drops in turbulent stirred dispersions	Sanjeev Kumar	213
Experimental measurement techniques with holography and speckle	T. S. Radha Bai	215
Studies on thin film pressure transducers and strain gauges	K. Rajanna	219
Algorithms for some problems on trees and graphs	Naveen Gabrani	222
A stochastic dynamical system for edge detection	K. Uma	224
Creep behaviour of Ti-24Al-11Nb alloy	R. S. Sundar	225
Synthetic, spectroscopic and structural investigations on cyclic and acyclic phosphazanes and their transition metal complexes	R. Murugavel	229
Numerical studies of laminar compressible boundary layer flows with heat and mass transfer	Satyajit Roy	231
Light scattering investigations of reentrant phase transitions of liquid mixtures	B. V. Prafulla	233
A study on generation and characterisation of transverse and longitudinal cracks in thick weldments	C. Mani	236
Studies in stereoelectronic effects at oxygen	C. D. Roy	237
Radical cyclisation and annulation strategies to chiral bi- and tricyclic bridged systems	P. Hemamalini	240
Synthesis of bridged and spiro systems employing 3-exo and 5-exo radical cyclisation reactions	G. Veera Raghava Sharma	245
Labelled clustering and its applications	V. Sridhar	249
Notch fatigue under aircraft spectrum loading	V. Raghu	252
Some investigations on the development of electronic components based on superconducting films	M. V. S. Lakshmi	257
Performance analysis of scheduling strategies in switching and multiplexing of multiclass VBR traffic in an ATM network	N. Lillykutty Jacob	259
Ocean acoustic tomography using the normal mode approach	P. V. Nagesha	262

Supercombinator-based implementation of lazy functional programming languages

Anurag D. Mendhekar

266

Thermal, mechanical and nondestructive characterization of carbon-carbon

A. Ajay Kumar

268

Modelling of maneuvering for wheeled mobile robots

R. Balakrishna

270

Flow in pipes of uniform and non-uniform cross-section with physiological applications

K. Padmavathi

273

IISc THESES ABSTRACTS

Thesis Abstract (Ph.D.)

A specification environment for distributed real-time systems by Rajib Mall

Research supervisor: L. M. Patnaik

Department: Computer Science and Automation

1. Introduction

Real-time computer systems usually find applications in safety-critical areas. Thus, real-time systems need to be extremely reliable. However, most of the real-time systems are 'distributed' in nature. The increased complexity due to the 'distribution' of the system structure compounds the problem of developing reliable systems. It is widely acknowledged that the use of formal specification techniques can contribute towards increasing system reliability. However, the existing specification techniques do not satisfactorily address to the issues of distribution and 'real-time'. In this context, this dissertation reports the work undertaken to develop a suitable specification environment for distributed real-time systems. This specification environment consists of two formal languages to describe the real-time behaviour of systems at the requirements specification and system specification levels. A set of tools is also developed to reason about the specifications.

The dissertation starts by examining the constraints that the issues of distribution and real-time impose on the specification. It turns out that new concepts concerning the underlying semantic model are mandatory. Emphasis is placed on the need for a partial order framework due to the fact that global states are not reasonably obtained in distributed systems and global clocks are very difficult to implement in a distributed environment. For accurate and natural modelling of distributed real-time computations at different levels of abstraction, suitable semantic models are synthesized from the existing ones.

Recent work has shown that complex systems like distributed real-time systems can be proficiently described, modelled, constructed, and managed in terms of their configuration¹. The underlying model associated with this configuration paradigm is a set of processing components loosely connected by communication channels. We advocate the use of the same underlying configuration throughout the system development activity and reflect the same in our two developed specification languages.

Formal specification serves as a basis of contract between the customer who orders the system and the implementation team. From this classical scenario of specification, two distinct views emerge, the customer's view or the requirements specification and the view of the implementation team or the system specification. To support formal specification at both these levels, two specification languages have been developed: one for requirements specification and the other for system specification.

2. Requirements specification

The requirements specification language is based on a timed version of the event structures (TES). We have developed this version by timing the event occurrences, and by associating a timing component with the causality relation. A language shell (named SLATES) for the timed version of the event structure is developed to provide convenient notations and to facilitate easy construction of the requirements specifications. To reason about the requirements specifications, a modal logic (named TESL) patterned after the timed version of the event structures is developed. TESL is a first-order logic augmented with modalities for temporal causality and conflict. A method is provided for automatic translation of the SLATES specifications into TESL formulas. The problem of automatic verification of TESL specifications is discussed and effective solutions are provided as extensions to the classical tableau algorithm. Automatic verification tools are developed using PROLOG language to verify the satisfiability of a restricted class of TESL specifications. These developed tools include one each for checking the model, satisfiability (consistency) of specifications and the conformity of event

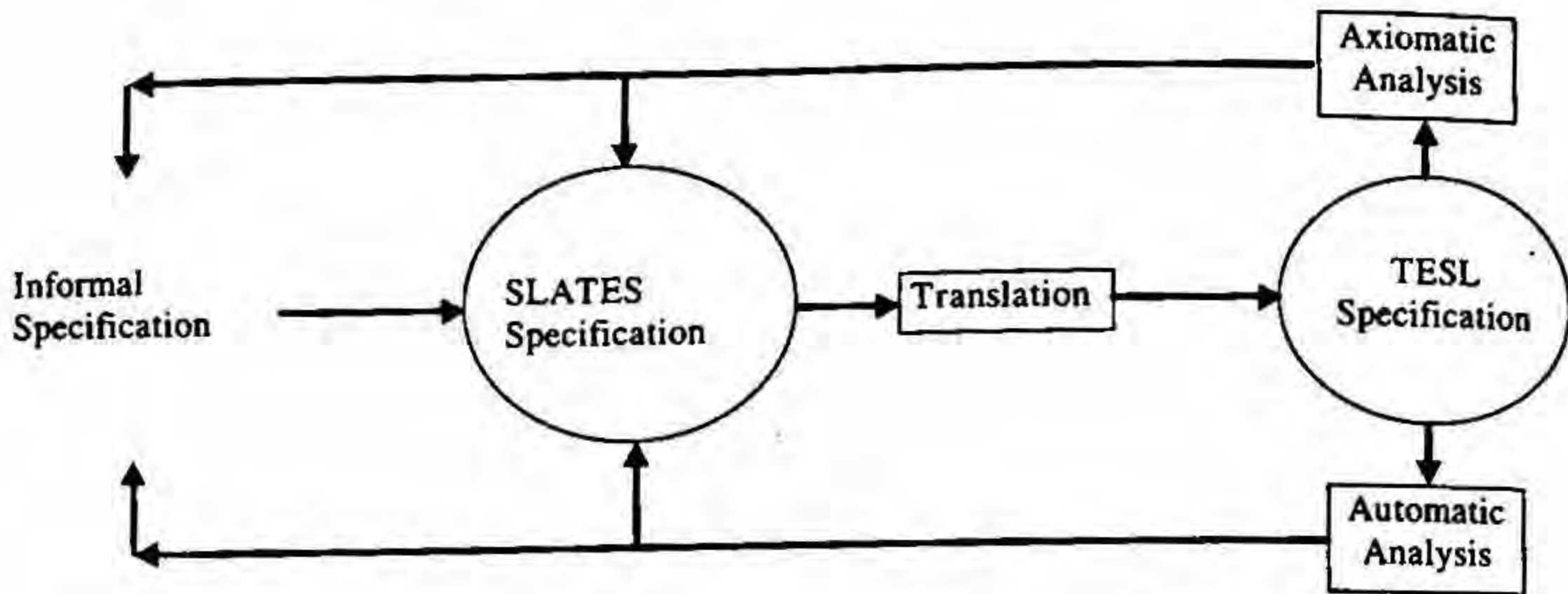


FIG. 1. Requirements specification framework.

traces with the specifications. To reason the unrestricted TES specifications, a sound axiomatic system is developed. The schematics of the developed framework for requirements specification is shown in Fig. 1. A few sample programs have been specified and analyzed to illustrate the use of the developed formalism.

3. System specification

A modal logic called distributed logic (DL) has been developed for system specification². DL is a first-order logic augmented with spatial modal and temporal operators. DL can be used to specify a real-time system with respect to an underlying system configuration. This notion of an underlying system configuration is a set of loosely connected processing components. DL can provide an accurate model of real-time computations by defining a partial order among the states of an ordered set of total order sequences (Fig. 2). The total order sequences represent computations of the individual nodes and the partial order relation allows us to combine the behaviour of the individual nodes to arrive at some global properties of the system.

DL relates the behaviour of the individual nodes of a distributed system by using spatial modal operators to arrive at some global properties. The time values are represented by using an uninterpreted clock predicate. The use of an uninterpreted clock predicate allows DL to accommodate a variety of underlying time structures, ranging from dense to discrete and finite time structures. In particular, dense time domains will be used for developing the axiomatic proofs, and the discrete and finite time structures will be used to develop the automatic verification tools. A precise definition of the syntax and semantics of DL is provided for this purpose. A sound axiomatic system is developed to reason the unrestricted DL specifications. A set of tools has been developed to automatically verify a restricted class of DL specifications. These tools include one each to check DL models, to assess the satisfiability of DL specifications, and to test the conformance of event traces with the corresponding specifications. Most of the related specification formalisms³ (for example, Ghezzi *et al.*³) are not able to specify distribution of system structure and do not permit reasoning about a system with respect to an underlying system configuration.

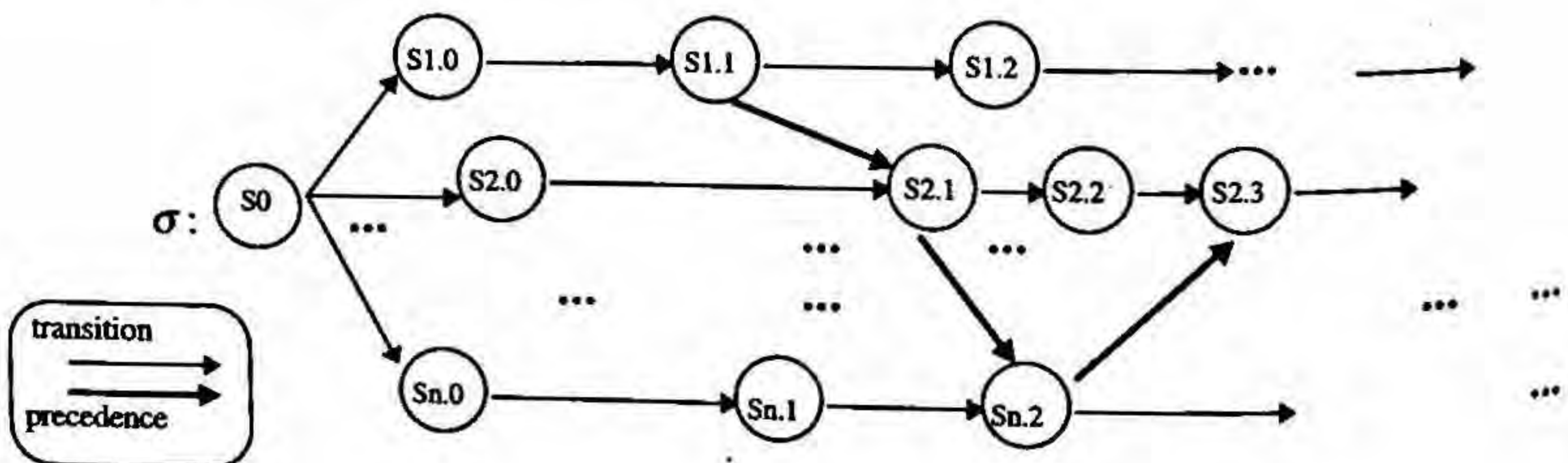


FIG. 2. A computation in DL.

The developed framework has been tested on a number of sample problems. The aim of such experiments is to demonstrate the adequacy of the specification languages and the effectiveness of the developed tools.

References

1. PATNAIK, L. M. AND MALL, R. Specification of real-time systems, *Int. J. Software Engng Knowledge Engng*, 1993, 3, 267-285.
2. MALL, R. AND PATNAIK, L. M. Formal timing analysis of distributed systems, *Int. J. Parallel Prog.*, 1991, 20, 75-93.
3. GHEZZI, C., MANDRIOLI, D. AND MORZENTI, A. TRIO: A logic language for executable specification of real-time systems, *J. Systems Software*, 1990, 12, 107-123.

Thesis Abstract (Ph.D.)

Finite element analysis of heat transfer and fluid flow in laser melting and solidification by K. Ravindran

Research supervisors: J. Srinivasan and A. G. Marathe

Department: Mechanical Engineering

1. Introduction

Laser surface-melting can be used to produce a surface layer with desired properties such as wear and corrosion resistance. A study of heat transfer and fluid flow in surface-melting would help in optimizing the process parameters. A majority of the previous works on welding and laser-melting have been done by the finite difference method¹; upwinding has been employed to get stable solutions. Though upwinding gives physically realistic solutions even on a coarse grid, the results are known to be inaccurate. In this thesis, an explicit finite element method (FEM) has been used to model laser surface-melting and solidification. FEM has been chosen due to its advantages such as higher accuracy, ability to handle unstructured grid, and better approximation of solid-liquid interface.

2. Numerical procedure

The axisymmetric configuration studied in this thesis is given in Fig. 1. The governing equations for the conservation of mass, momentum and energy (for laminar flow) are solved in primitive variable form. Both buoyancy and surface-tension forces are considered. An explicit projection method² is used to solve the governing equations in a sequential manner. First an intermediate velocity field is computed by dropping the pressure gradient terms from the momentum equations. Pressure is then obtained from a Poisson equation. Finally, the velocity is corrected. The Galerkin FEM has been used for discretization as it is more accurate. The latent heat has been added to the specific heat of the two-phase mushy zone. Three-node triangular elements

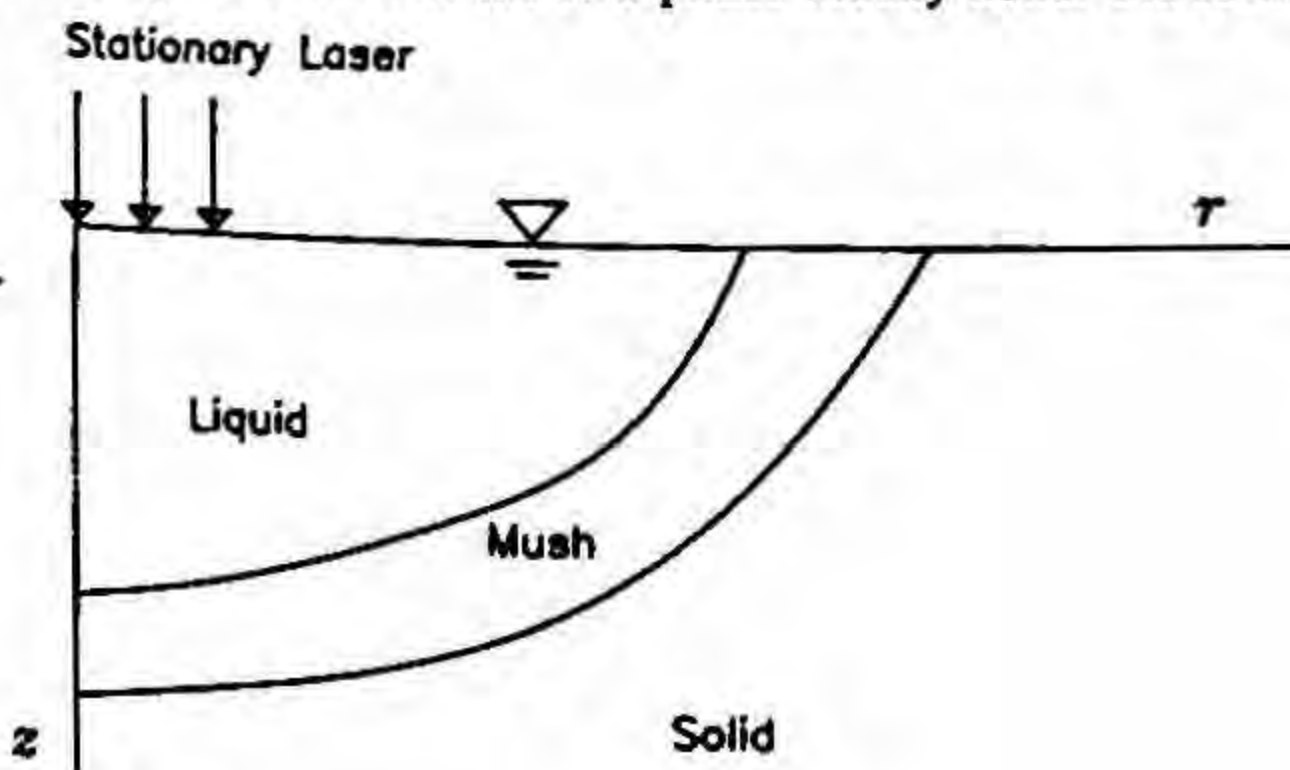


FIG. 1. Laser surface-melting.

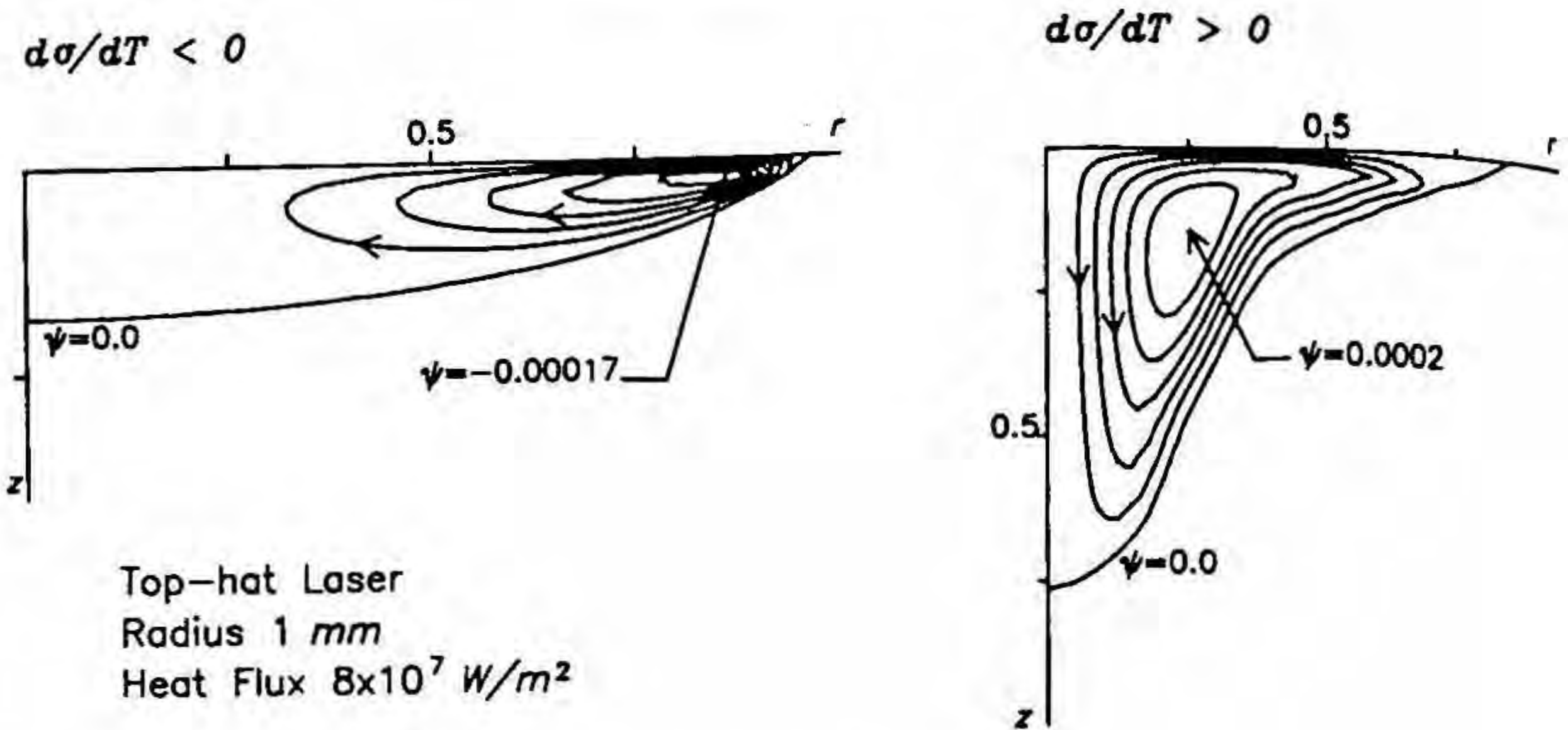


FIG. 2. Results on continuous-wave laser. Steady state streamlines.

have been used with linear interpolation for velocity, pressure and temperature. Numerical results have been presented for various values of the process parameters.

3. Results

Studies on continuous-wave lasers showed that the buoyancy flow is usually weak due to the small dimension of the pool. For steel, which has a high Prandtl number, surface tension forces are very dominant. The nature of flow and its effect on the temperature distribution within the melt depend strongly on the sign and magnitude of the temperature coefficient of surface tension, $d\sigma/dT$. The steady-state results are given for a Reynolds number of 28500 ($|d\sigma/dT| = 10^{-4} \text{ N/mK}$) in Fig. 2; streamlines are given for both negative and positive values of $d\sigma/dT$. For negative values of $d\sigma/dT$, a clockwise convection cell is formed, and hence the melt pool becomes broad and shallow. When $d\sigma/dT$ is positive, an anticlockwise convection cell is formed, which makes the pool narrow and deep. The melt width is essentially governed by the beam radius, while the melt depth depends on heat flux and $d\sigma/dT$. For AlCu (4.5%) alloy, which has a low Prandtl number, the effect of the surface-tension driven convection is not significant. For this alloy, the melt width values obtained from a conduction analysis matched well with published experimental work.

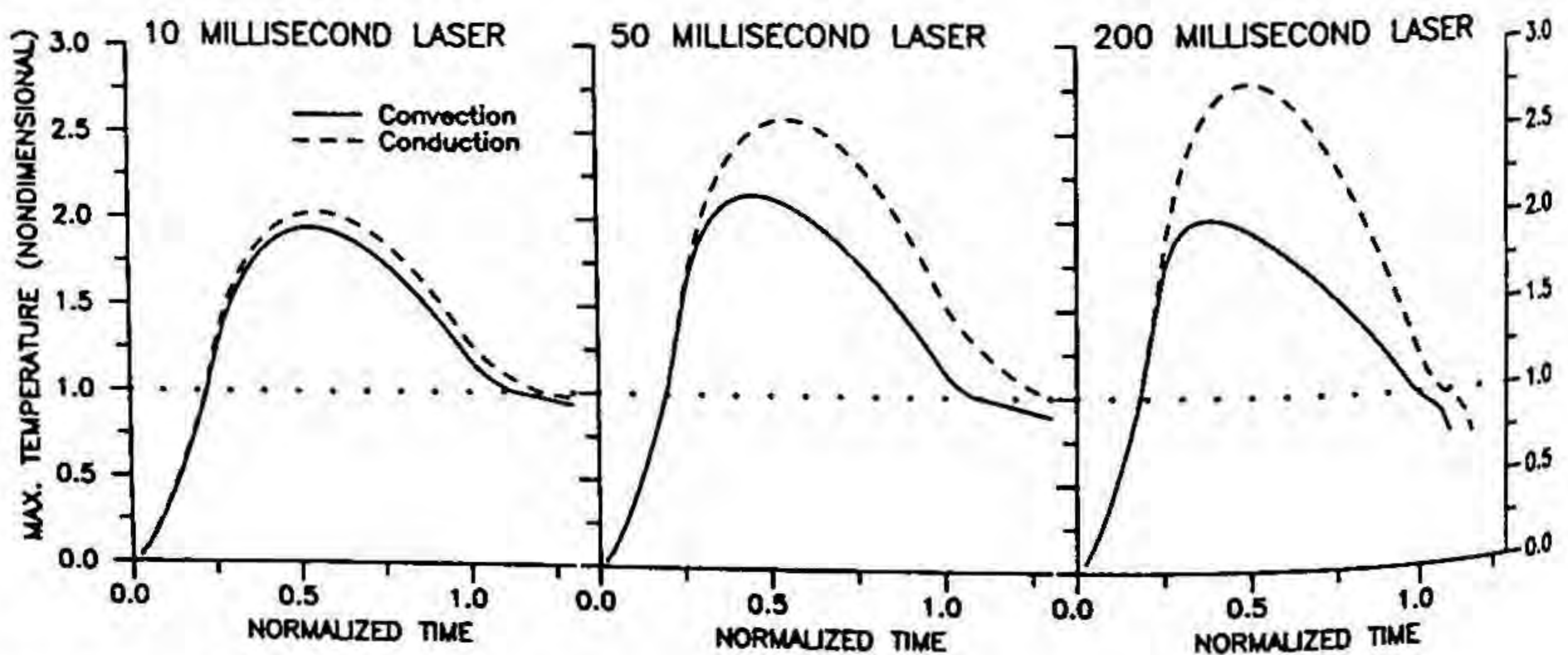


FIG. 3. Results on pulsed laser. Effect of convection on the maximum melt temperature.

Transient solutions have been presented for pulsed lasers of duration 10, 50 and 200 milliseconds. The peak flux has been chosen such that the maximum temperature attained is about the same for all the pulse durations. Computations have been made till the material solidifies. For the 10 millisecond laser, the effect of convection is very less. Even a pure conduction analysis can predict the transient variation of most of the parameters; the maximum difference between the values predicted by convection and conduction is about 13%. For a bismuth substrate heated by a 0.2 millisecond laser, the melt width values obtained by a conduction analysis agreed well with published experimental work. For the 50 and 200 millisecond lasers, the effect of convection is significant. The parameters predicted by the convection program can differ as much as 43% from the pure conduction analysis. The transient variation of the maximum melt temperature is shown in Fig. 3; in order to highlight the role of the surface-tension driven convection, the results obtained for the pure conduction analysis are also given. During resolidification, the solidus interface moves slower than the liquidus due to the finite time required to transfer the latent heat from the mushy zone to the solid substrate. Hence the mushy zone occupies a large volume during the resolidification phase. The study on pulse duration suggested that the melt width is primarily determined by the radius of the laser beam, while the melt depth is determined by pulse duration. Convection increased the temperature gradient across the interface and accelerates the resolidification process. The solidification parameters such as cooling rate and growth rate are generally found to be high when convection is present.

References

1. MILLS, K. C. AND KEENE, B. J. Factors affecting variable weld penetration, *Int. Mater. Rev.*, 1990, 35, 185–216.
2. RAMASWAMY, B. Solution of the Boussinesq equations by the finite element method, *Finite Elements in Analysis Des.*, 1989, 6, 319–335.

Thesis Abstract (Ph. D.)

Study of some artificial intelligence paradigms for partial discharge pattern recognition by L.Satish

Research supervisor: B.I. Gururaj

Department: High Voltage Engineering

1. Introduction

Partial discharges (PSs) can arise due to various situations within the electrical insulation system and give rise to different characteristic patterns during their measurement. These patterns contain vital information regarding the number and amplitude of PD pulses, the phase positions at which they occur, their phase spread, etc. Over the years, experts have used this information together with their experience to interpret PDs on a cause and effect basis^{1,2}. Unfortunately, these PD patterns are inherently complex due to their random nature, and further can be complicated due to interferences in test areas, making the task of interpretations really difficult. Hence the complex nature of various PD patterns, their random behaviour and extensive usage of wideband PD detectors displaying such patterns on the one hand and easy availability of fast personal computers and new paradigms in artificial intelligence (AI) on the other, amply suggest the application of different AI paradigms for PD pattern recognition (PR). From the literature study, it emerges that a system capable of classifying all types of PDs (inclusive of interferences) on a common basis and using only the visual PD pattern information has, so far, not been reported.

2. An overview of the approach

This thesis addresses the applicability of three widely used AI paradigms—Rule-based systems (RBS), Neural networks (NNs) and Hidden models HMMs) for PD PR. This task essentially consists of signal-pattern extraction from that on the PD detector CRT screen. This is captured by a camera and subsequently recognized by the chosen paradigms. Implementation of these paradigms obviously calls for a large number of examples for each type of PD

considered. As it is impractical to obtain all of them using HV equipment and specially prepared models, a synthetic PD pattern generation scheme, comprising a waveform digitizer (Tek-RTD 710A), an instrument controller (Tek-4041) and an oscilloscope, was devised. It enabled generation and display on an oscilloscope, any complicated pattern, whose features could easily be varied. A CCD camera system (Tek-DCS-01) was used to capture the pattern, which was processed to obtain the signal pattern. If the pulses are digitized using A/D converters, this stage can be reached directly. The signal pattern was averaged to obtain a 36-point long sequence, which forms the input to the recognition system. These synthetic patterns were used for training and testing of the paradigms.

A study of the patterns given in references ^{1,2} lead to the identification of 21 key PD patterns. Hereafter, those arising due to insulation-related problems will be referred to as Category A (in all 14 classes). An overall recognition rate of 94, 89, and 90% was obtained for the three paradigms respectively when tested with synthetic PD paradigms.

3. Recognition of actual PD patterns

To further assess the ability of the developed paradigms, recognition tests using actual PD patterns were conducted. The following five types of PDs belonging to Category A (a–e) and three types belonging to Category B (f–h) were chosen.

- a) Void within a dielectric.
- b) Multiple voids in epoxy insulation.
- c) Sharp point on HV conductor.
- d) Surface discharge on cable sample.
- e) Contact noise.
- f) Six-pulse bridge interference.
- g) Radio broadcast interference.
- h) Amplifier noise.

The performance of the three paradigms is described below.

3.1. *RBS*: At the outset, it must be clarified that due to the presence of higher levels of noise and interference in actual patterns and as the stored templates are not derived from them, a lower percentage of template match or even its failure can be expected for some classes. Hence, the ability of this paradigm for actual patterns should not be assessed on the final match alone, but instead, on the ability to correctly recognize the sub-group to which the input belongs. Acceptable results were obtained for Classes A and C. However, lower recognition rates were obtained for Classes B and E due to the failure of template match (however, sub-groups were correctly recognized on each trial). The RBS method is 'brittle' as it breaks down due to the absence of a few more relevant rules, which is a drawback. The two interference patterns, G and H, yielded very good results (100%) since only key features had to be found.

3.2. *NNs*: Among the four trained NNs, two performed well and yielded recognition rates of 78 and 84%, respectively. Even though all had performed well in generalization tests with synthetic patterns, the remaining NNs managed only 53 and 71%. For interference patterns two of the four NNs gave 79 and 78%, while the others could each manage only 57%. A possible reason may be the insufficient generalization acquired. The non-existence of a norm of to verify and or quantify it for any trained NN brings up the need for such tests. Also, higher levels of noise for which NNs have not been specifically trained may be another reason.

3.3. *HMMs*: All the HMMs performed well when fed with actual PD patterns, except Class D. Even though the corresponding HMM had performed well with synthetic patterns, it failed in all trials. This may be attributable to the insufficient generalization or due to a failure to reach the optimal local minima on the error surface. This particular HMM was re-trained with a training set containing a few extracts from the actual PD patterns as well. It performed well thereafter. An overall recognition rate of 84% was obtained for Category A patterns. With similar steps for Classes G and H, a recognition rate of 81% was achieved.

4. Conclusions

The ability of the three paradigms when fed with actual examples of simple and complex PD patterns has been demonstrated. It emerges that NN and HMM are better suited to handle practical conditions when compared to RBS.

References

1. CIGRE Working Group 21.03 Recognition of discharges, *Electra*, 1969, No. 11, 61-98.
2. NATTRASS.D.A. Partial discharge measurement and interpretation, *IEEE EI Mag.* May/June 1988, 4(3), 10-23.

Thesis Abstract (Ph.D.)

Flexure of laminated composite plates—New refined lamination-dependent shear deformation models by Kesari Jawahar Reddy

Research supervisor : K.Vijayakumar

Department : Aerospace Engineering

1. Introduction

Extensive use of fiber-reinforced composites in engineering structures has evoked considerable interest in the accurate prediction of response characteristics of laminates. Most of these composites in use to date possess relatively small transverse shear modulus resulting in transverse shear deformation effects becoming more pronounced, thus reducing the effective flexural stiffness of laminated plates. In spite of idealizing each ply as an equivalent orthotropic homogeneous medium, the complexity of three-dimensional elasticity approach has resulted in the development of several two-dimensional approximate models.

It is known that classical laminate plate theory (CLPT) cannot account for the warping and zig-zag in-plane deformation of adjacent layers in thick laminated composites¹. As such, several new theories have been developed to overcome these deficiencies (*e.g.*, see Nor and Burton²). Most of these theories based on method of hypothesis and variational methods can be broadly classified into three groups:

- Group I: Models based on thicknesswise ply-independent displacement distributions. These models are referred to as extended homogeneous plate models (EHPM).
- Group II: Discrete layer models (DLM).
- Group III: Models based on a priori assumed/derived lamination-dependent displacement distributions. It is appropriate to call these models as smeared laminate models (SLM).

The theories based on extension of homogeneous plate theories to laminates (EHPM) do not reflect properly the response characteristics of laminates, particularly bending strains and stresses. In most of the homogeneous plate theories, shear corrective terms in displacements correspond to those obtained from thicknesswise distributions of statically equivalent transverse stresses. In the case of laminates, a systematic development in arriving at such displacement distributions is, generally lacking in the literature.

This thesis is an attempt towards the systematic development of new refined shear deformation models for the analysis of flexure of laminates. Here, Group III type of modelling is considered, since models in Group III retain the simplicity of Group I models in using reference plane variables (so that they are independent of the number of plies) but take into account material discontinuities.

A systematic approach to derive lamination-dependent displacement distributions was presented by Valisetty and Rehfield³, in which statically equivalent transverse shear stresses and transverse normal strain from constitutive

relations expressed in terms of CLPT stress resultants were used. Later, Vijayakumar and Krishna Murthy⁴ adopted the iterative concept inherent in terms of reference plane displacement variables and their derivatives.

Whitney⁵ pointed out that the large discontinuities in the gradient of the transverse shear stress at the adjacent layers as displayed in elasticity solution do not occur in assumed transverse shear stress distributions due to the fact that the magnitude of such a discontinuity for a cross-ply plate is a function of the ratio G_{LT}/G_{TZ} . He, however noticed that, if the equilibrium equations are used instead of assumed functions, to calculate transverse shear stresses, the discontinuity would be determined by E_L/E_T and that it would be in good agreement with the elasticity solution. Based on Whitney's observation and an iterative approach, new lamination-dependent higher-order shear deformation models are developed in this thesis.

To start with, thicknesswise distributions for thicknesswise gradients of transverse shear stresses based on elasticity equilibrium equations in each ply are assumed. These distributions are obtained using CLPT or CLSDT (generally referred to as FSDT) in-plane stresses in 3-D elasticity equilibrium equations. Derivatives of displacement variables in these equations are replaced by new unknown variables. Higher-order shear corrective terms in the in-plane displacements are derived from the following steps:

1. Integration of thicknesswise gradients of transverse shear stresses, maintaining continuity across the interfaces and satisfying shear-free surface conditions.
2. Transverse shear strains are obtained from constitutive relations using the transverse shear stresses of step (1).
3. Shear corrective terms are obtained from integration of transverse shear strains in step (2), and maintaining continuity across interfaces.

By adding the above shear corrective terms to CLPT or CLSDT (generally referred to as FSDT) in-plane displacements, new lamination-dependent shear deformation models are developed.

2. Results and discussion

Initially, models are developed for cross-ply plates in cylindrical bending and are subsequently extended to finite plates. Although the development of models for symmetric laminates is straightforward in the present approach⁶, development of corresponding models for unsymmetric laminates requires the consideration of above models as special cases. Simple models⁷ for cross-ply plates based on extension of models for cylindrical bending of cross-ply laminates in either direction are also presented. Performance of the present models is evaluated by comparing the solutions from the present models with those from exact elasticity solutions for simply supported plates subjected to sinusoidal loading.

Similar models for angle-ply laminates in cylindrical bending are also developed. Assumed linear thicknesswise distributions for the gradients of transverse shear stresses with respect to thickness coordinate, obtained using CLPT in-plane stresses in elasticity equilibrium equations, are different from those obtained using CLSDT in-plane stresses, except in the special case of antisymmetric laminate. Using these gradients of transverse shear stresses, two kinds of lamination-dependent shear corrective terms are derived. Adding these corrective terms to CLPT and CLSDT displacements, four new shear deformation models are developed. Performance of these models is evaluated by comparing the results from these models with those from exact elasticity solutions for antisymmetric 2-ply laminates and for 4-ply $[15/-15]_s$ laminates. The present models yield good estimates for maximum values, interface values and thicknesswise distributions of displacements and stresses even for thick plates with span-to-depth ratio up to 3 and Young's modulus in fiber direction as large as forty times the Young's modulus in the transverse direction to the fiber. In general, the model with shear corrective terms based on CLPT and added to CLSDT displacements is sufficient and predicts good estimates both qualitatively and quantitatively for all displacements and stresses.

Keeping in view the models developed for the special cases like symmetric laminates, cross-ply laminates, antisymmetric laminates, cylindrical bending of laminates in either direction and to have the minimum number of

variables, models for general laminates have also been developed. Closed-form solutions from these models are obtained for antisymmetric angle-ply laminates under sinusoidal load for a type of simple supported boundary conditions. Results obtained from the present models are compared with those reported in the literature.

References

1. PAGANO, N. J. Exact solutions for rectangular bidirectional composites and sandwich plates, *J. Compos. Mater.*, 1970, 4, 20-34.
2. NOOR, A. K. AND BURTON, W. S. Assessment of shear deformation theories for multilayered composite plates, *Appl. Mech. Rev.*, 1989, 42, 1-13.
3. VALISETTY, R. R. AND REHFELD, L. W. A refined theory for stress analysis for stress analysis of composite laminates, *AIAA J.*, 1985, 1111-1117.
4. VIJAYAKUMAR, K. AND KRISHNA MURTY, A. V. Iterative modeling for stress analysis of composite laminates, *Compos. Sci. Technol.*, 1988, 32, 165-181.
5. WHITNEY, J. M. The effect of transverse shear deformation on the bending of laminated plates, *J. Compos. Mater.*, 1969, 3, 534-547.
6. JAWAHAR REDDY, K., NAGARAJ, K. S. AND VIJAYAKUMAR, K. A new approach for the analysis of flexure of symmetric laminates, *AIAA J.*, 1991, 1960-1966.
7. JAWAHAR REDDY, K. AND VIJAYAKUMAR, K. Bending and vibration of symmetric cross-ply laminated plates using ply dependent shear deformation model, *J. Sound Vibration*, 1992, 158, 257-265.

Thesis Abstract (Ph.D.)

Information asymmetry in agency, bargaining and market contexts by P. Guruswamy Babu

Research supervisor: B. G. Raghavendra

Department: Management Studies

1. Introduction

The standard micro-economic theory, as epitomized by Walras-Arrow-Debreu's 'General equilibrium theory'¹, assumes that all the economic agents have complete information about their environment. But one comes across many real-world institutions such as labour, insurance, stock and auction markets as well as common place interactions such as those between a buyer and a seller, a physician and a patient, a plaintiff and a defendant, which are characterized by varying degrees of informational asymmetries. These asymmetries arise due to the private knowledge available to one or both of the parties. Research into these informational aspects of the economic activity is a major pre-occupation of the present-day economic theorists and this broad spectrum comes under the rubric of 'economics of information'.

This thesis attempts to address issues related to three of the major constituents of information economics viz., agency theory, bargaining theory and the theory of rational expectations. Each one of these branches, though connected by a common thread, requires different modelling tools and differs considerably in detail. We developed a common framework for studying informational asymmetries using classic examples from the literature. Agency, bargaining and rational expectations theories are linked to the common programme of general equilibrium theory through an appraisal of historical antecedents of information economics.

2. Results and discussion

2.1. Agency theory

In the standard agency model², a risk neutral principal employs a risk averse agent to put efforts in realizing a goal. The agent's actions might be unobservable (hidden action) or he may have some private knowledge relevant to the contractual relationship with the principal (hidden knowledge) or both his actions and knowledge might be hidden³. In such cases, the principal should devise his optimal incentive contracts based on some imperfect indicators of the agent's effects. We present a new framework for the construction of such optimal contracts in static and dynamic contexts.

Traditionally, the static agency problem has been formulated as a constrained optimization problem and the existence of an optimal contract is shown using Karush–Kuhn–Tucker conditions⁴. What is missing in literature is a constructive method of proof to find the optimal contract. Using nonlinear functional analytic methods, such a method is developed for the infinite dimensional case.

Multi-period agency relationship are observed in many economic contexts such as labour market. One needs to analyse the reasons behind the existence as also the nature of such dynamic contracts. Whether such contracts lead to first best optimal solutions and whether they could be replaced by a sequence of short term contracts are some of the prominent questions that arise. We develop a framework using stochastic dynamic programming methods to study the learning possibilities of the principal in the dynamics contexts marked by hidden action, hidden knowledge as well as a combination of the two. For all the three cases we show that the principal could achieve the first-best outcome when there is discounting.

We then apply the agency theory results to study the important problem of intergenerational sharing of a fixed exhaustible resource. Given an exhaustible resource whose size of stock is unknown, a major normative problem is to distribute this stock over different generations⁵. This normative problem can be stated as follows: The present generation has inherited an exhaustible resource which is a common good. It has to extract the resource optimally and also invest a large amount of its wealth and effort in R&D to improve this resource usage. Alternatively, it should invest in R&D to find a technological alternative or substitute. Ethically, it may be argued that risk and uncertainty should be shared by the posterity, which is to benefit from such investments. After a succinct review of various ethical rules involved, we formulate this problem as an agency model and characterize the optimal resource sharing mechanism taking into account the informational asymmetries.

2.2. Bargaining theory

From the contractual relationship we move on to bargaining models. We consider a two sided non-cooperative bargaining model with infinite time horizon and incomplete information, between a buyer and a seller who bargain over the price of an object to be sold. In general, such a model would yield multiple Nash equilibria⁶. We try to circumvent this problem by modelling the above bargaining problem as a non-zero sum Dynkin game wherein the player's strategies are stopping times. These strategies satisfy the properties of a lattice and hence using the lattice theoretic methods we are able to characterize the multiple Nash equilibrium set. For a special case, we construct the subgame perfect equilibrium strategies.

2.3. Rational expectations equilibrium

The issue of the existence of the rational expectations equilibrium for the case of agents with different priors is then considered. According to the rational expectations equilibrium paradigm⁷, agents with lesser information can learn about the private information of the more informed by observing a market aggregate such as price. We show that such learning can take place only under very restrictive conditions.

2.4. Economics of law

We analyze a real-world legal case between the Government of India and the Union Carbide Corporation, arising out of the Bhopal gas disaster, using the concepts of information economics. Many issues such as the choice of the

the delay in the settlement, bargaining inefficiency, the nature and form of lawyer's contracts as well as the choice of the legal standards are analyzed. As an offshoot, we disprove Coase's conjecture on the efficiency of bilateral bargaining. The relevance of information economics in general and bargaining models in particular to the economics of law are brought out. Also, these analyses help to illustrate the practical relevance of the theoretical models developed in this thesis.

Finally, some specific open problems and issues which could become topics of future research such as bounded rationality, learning in games, the role of experimental techniques in game theory and robust bargaining protocols are pointed out.

References

1. **ARROW, K. J.** The role of securities in the optimal allocation of risk-bearing, *Rev. Econ. Stud.*, 1964, 31, 91-96.
2. **HOLMSTROM, B.** Moral hazard and observability, *Bell J. Econ. Mgmt.*, 1979, 10, 74-91.
3. **ROGERSON, W. P.** The first order approach to the principal-agent problem, *Econometrica*, 1985, 53, 1357-1367.
4. **ARROW, K. J.** The economics of agency. In *Principals and agents: The structure of business* (Pratt, J. W. and Zeckhauser, R., eds), 1985, pp. 37-51, Harvard University Press.
5. **SOLOW, R. M.** Intergenerational equity and exhaustible resources, *Rev. Econ. Stud.*, *Symposium on the Economics of Exhaustible Resources*, 29-45.
6. **OSBORNE, M. J. AND RUBINSTEIN, A.** *Bargaining and markets*, 1990, Academic Press.
7. **BRAY, M. AND KREPS, D. M.** Rational learning and rational expectations. In *Arrow and the ascent of modern economic theory* (Feiwel, G. R., ed), 1987, pp. 597-625, New York University Press.

Thesis Abstract (Ph.D.)

Breakage and coalescence of drops in turbulent stirred dispersions by Sanjeev Kumar Gupta

Research supervisors: R. Kumar and K. S. Gandhi

Department: Chemical Engineering

1. Introduction

Turbulent stirred liquid-liquid dispersions are frequently employed in chemical industry to carry out operations such as extraction, heterogeneous reactions, direct contact heat-transfer, etc. The efficiency of these operations strongly depends on the drop size distribution and the state of mixing of the dispersed phase, both of which are determined by the breakage and coalescence of drops in the stirred dispersion. An improved efficiency of these operations is possible only through the understanding of these basic processes, and the present work constitutes an effort in this direction.

2. Alternative mechanisms of drop breakup in stirred vessels

Drop breakage in stirred vessels has been hitherto assumed to occur due to the interaction of a drop with a single eddy of the same size. Inertial stress tends to deform the drop while interfacial tension and viscous stresses resist it. The drop is assumed to break if it reaches a critical deformation within the lifetime of the eddy¹. As the drop size decreases, inertial stress and lifetime of eddy decrease whereas the total resistive stresses increase. Thus, there

exists a drop size d_{max} such that drops smaller than this do not break. As the dispersed phase holdup, ϕ , increases, the turbulence intensity decreases and the d_{max} is predicted to increase. Experimental data however show that d_{max} first increases with ϕ , passes through maximum and begins to decrease at high ϕ . This cannot be explained through the hitherto known mechanisms of drop breakage in stirred dispersions. The present work proposes two additional mechanisms of drop breakage involving flow at the impeller blade itself to explain these unexpected results. The mechanisms are: drop breakup in accelerating flow field around the blade tip and in the shear flow held in the boundary layer on the blade. It is shown that in a stirred vessel, all the three mechanisms operate simultaneously and the experimentally observed d_{max} corresponds to the smallest of the d_{max} values obtained through the three mechanisms. It is found that at low values of ϕ , turbulent mechanisms gives smallest d_{max} and at high ϕ , drop breakup in blade tip region due to accelerating flow yields smallest value of d_{max} . The unusual trends are predicted quite well for low as well as high dispersed phase viscosities.

3. A multi-stage model for drop breakup

At very low value of ϕ and for large dispersed phase viscosity, μ_d , the existing models¹ predict drop size to become independent of interfacial tension, σ , and to increase as $3/4$ power of μ_d . Reported experimental data^{2,3} however show that drop size does not become independent of σ and the dependence on μ_d is quite weak. A new model has been proposed which divides the stirred vessel into two zones: one near the impeller where dissipation rates are high and the other away from the impeller where they are low. The model assumes that a drop deforms in the impeller zone and retracts partially or completely in the circulation zone. The drop can thus break through many cycles of deformation and relaxation. The drop is considered to be stable if, starting with zero deformation in its first cycle, it reaches a steady state where its deformation in the impeller zone is exactly equal to its retraction in the circulation zone. If the drop fails to reach such a steady state, it is assumed to break. The model successfully explains the hitherto unexplained results. In comparison with existing empirical correlations, which apply only in a part of the range, the present model applies in full range of variables and predicts data very well.

Based on possible simplifications of this model, a simple procedure has been developed to predict d_{max} . It is shown that these simplifications cover the entire range of variables investigated so far.

4. A new model for coalescence efficiency

Coalescence of drops is assumed to occur when two drops come sufficiently close to each other and intervening film separating them ruptures. Various models are available in literature for this phenomenon; however, they result in contradictory predictions and require either unrealistic empirical constants or unknown parameters. A new model is therefore proposed which takes into account various physical processes. The model considers two drops embedded in an eddy, approaching each other at an arbitrary angle. The drop pair is permitted to undergo rotation, while the intervening film drains. The model permits the deformation of the tip regions and evaluates the time of rupture of the thin film based on stability considerations. If the film ruptures within the available contact time, coalescence is assumed to occur. The coalescence efficiency is defined as the fraction of the total range of possible approach angles that yields coalescence. The model shows that coalescence can occur in a variety of ways: head-on, non-head-on and drop shapes undergoing none, one or two transitions in shape. It predicts that coalescence efficiency can go through a maximum with variation in drop size and stirrer speed and thus reconciles the contradictory predictions made by the earlier models. It brings out the important role of several new variables such as dispersed phase viscosity, starting film thickness and Hamaker constant. The model further predicts that in general coalescence between unequal size drops is more efficient and the dispersions involving pure phases can be stabilized at high rotational speeds. It predicts that path history can play an important role in the evolution of drop size distribution. The model also provides explanations for some hitherto unexplained data reported in literature.

5. Phase inversion

Interfacial area for transport processes can be easily increased by increasing ϕ . However, at high ϕ , pure systems become unstable and invert. The present work deduces from the experimental evidence that the dependence of ϕ on rotational speeds at phase inversion shown by oil in water and water in oil dispersions involving the same oil and water system is exactly the opposite in nature. The consideration that phase inversion occurs due to the catastrophic coalescence in bulk alone is unlikely to explain these observations. An additional mechanism involving wetting character-

istics of the phases involved is suggested. It is proposed that if dispersed phase is heavier than the continuous phase and if it can wet the impeller material, the dispersed phase drops would coalesce with the impeller forming a layer on the blade. This layer would shred at the blade tip and would therefore affect hold-up values at inversion. The hypothesis was tested experimentally and validated.

6. Conclusion

The present work shows that in addition to hitherto accepted single shot breakup of drops due to turbulent flow field in stirred vessel, there are several other mechanisms operating simultaneously. These are: drop breakup in the blade tip region due to accelerating flow, in the shear layer on the blade, breakup in more than one cycle due to turbulent mechanism itself and shredding of a film of wetting dispersed phase from the blade. At low ϕ , turbulent mechanism dominates; however, at high ϕ , additional mechanism proposed here take on controlling role.

The work on coalescence shows that it can occur in a variety of ways. Drops can also coalesce with the impeller affecting inversion characteristics. The model reconciles contradictory predictions made by the earlier models, explains reported data⁴ and makes some interesting predictions.

It has further been shown that wetting character of the impeller material can influence inversion characteristics.

References

1. LAGISETTY, J. S., DAS, P. K., KUMAR, R. AND GANDHI, K. S. Breakage of viscous and non-Newtonian drops in stirred dispersions, *Chem. Engng Sci.*, 1986, 41, 65-72.
2. CALABRESE, R. V., CHANG, T. P. K. AND DANG, P. T. Drop breakup in turbulent stirred contactors, I: Effect of dispersed phase viscosity, *AIChE J.*, 1986, 32, 657-666.
3. WANG, C. Y. AND CALABRESE, R. V. Drop breakup in turbulent stirred-tank contactors; II: Relative influence of viscosity and interfacial tension, *AIChE J.*, 1986, 32, 667-676.
4. KONNO, M., ARAI, K. AND SAITO, S. The effect of stabilizer on coalescence of drops in suspension polymerization of styrene, *J. Chem. Engng Jap.*, 1982, 15, 131-135.

Thesis Abstract (Ph.D.)

Experimental measurement techniques with holography and speckle by T. S. Radha Bai

Research supervisors: B. S. Ramprasad and E. S. Raja Gopal

Department: Instrumentation and Services Unit

1. Introduction

Thermal stress is an important factor in the design and fabrication of thin films for many scientific and industrial applications. Almost all thin films are in a state of stress irrespective of the method of preparation. The stress manifests itself by being the substrate. Hoffman¹ has analysed that the total stress in a thin film consists of the contribution due to the differential thermal expansion of the substrate and thin film material and the stress induced due to the various parameters of nucleation and growth, which is usually termed as the intrinsic stress. Thermal stress can be measured by heating the thin film and measuring the deflection at the free end of the substrate fixed as a cantilever.

Theoretical considerations

Thermal stress is given by the equation

$$\sigma_T = \frac{E_f(\alpha_f - \alpha_s)\Delta T}{1 - \gamma_f} \quad (1)$$

where E_f is the Young's modulus of elasticity of the thin film, ν_f , the Poisson's ratio of the film, α_f , the thermal expansion coefficient of the thin film, α_s , the thermal expansion coefficient of the substrate, and ΔT , the difference in temperature.

The thermal stress is independent of the thickness of the thin film and varies directly as the difference in the thermal expansion coefficients.

It is observed from the reported work that in some cases there is a change in the nature of the stress when the substrate is heated and cooled over a wide range of temperature. The films used for measurement are mostly deposited on a thin substrate (0.5 mm thick) with the thickness of the film ranging from 0.1 to 15 μm . The film has an initial stress which induces a curvature on the substrate. While making a measurement on the thermal behaviour of the thin film the variation of the total stress with temperature is measured. When the intrinsic stress forms a large portion of the total stress, the effect of heating is to first overcome the bending due to the intrinsic stress. On further heating the thin film exhibits the effect of thermal stress. The thermal stress can only be inferred from the conventional measurements. In order to measure the thermal stress independently, it is necessary to minimize the intrinsic stress of the thin film. This is achieved by choosing a thick substrate and a thin film coating.

In the present investigation, experimental thermal stress is calculated using the following formula suggested by Ramprasad and Radha². The thermal stress is given as

$$\sigma_T = \frac{E_s t_s^3 \Delta}{4l^3 t_f} \quad (2)$$

where E_s is the Young's modulus of elasticity of the substrate, t_s , the thickness of the substrate, t_f , the thickness of the thin film, l , the length of the cantilever, and Δ , the maximum deflection at the free end of the cantilever. In deriving this formula it is assumed that the substrate is sufficiently thick and the thin film is having minimum intrinsic stress.

2. Experimental details

Real-time hologram of the cantilever substrate with coating can be taken by *in-situ* processing using monobath and liquid gate³. Any displacement of the object gives rise to interference fringes in a real-time situation. It is difficult to measure the thickness, stress and thermal stress of specularly reflecting films using reflected light. With divergent object and reference beams, it is observed that when one views through the hologram, a bright spot which is a reconstruction of the pinhole of the object beam is seen but the fringe pattern is not discernible. This problem is overcome by interposing a diffuser in between the specularly reflecting film and the hologram, which makes it possible to obtain good-quality holographic fringes.

A thin glass plate coated with the thin film is mounted on the substrate holder. A copper constantan thermocouple is attached to the film side of the sample to monitor its temperature during heating. Real-time hologram is taken. A radiant heater is used to heat the substrate. The change in temperature is measured by measuring the thermo emf. As the temperature increases, the temperature is noted down and the number of fringes localised on the ground glass plate are counted. As the temperature decreases and as the substrate attains room temperatures, the number of fringes tends to zero. It was found convenient to use a closed circuit television system to count the fringes and photograph them.

3. Results

The thermal stress is measured for several film-substrate combinations. The experimental stress is calculated using eqn 2. Some of the results are presented and analysed.

Figure 1 shows typical interference fringes representing the deflection of the cantilever for different temperatures of heating of aluminium film on glass substrate.

The measured thermal stress is calculated using well-defined values of the Young's modulus of elasticity of the substrate material, its thickness, the length, the film thickness and of the measured deflection. The observed results show that there is a discrepancy in the experimental and theoretical thermal stress values. The possible explanation

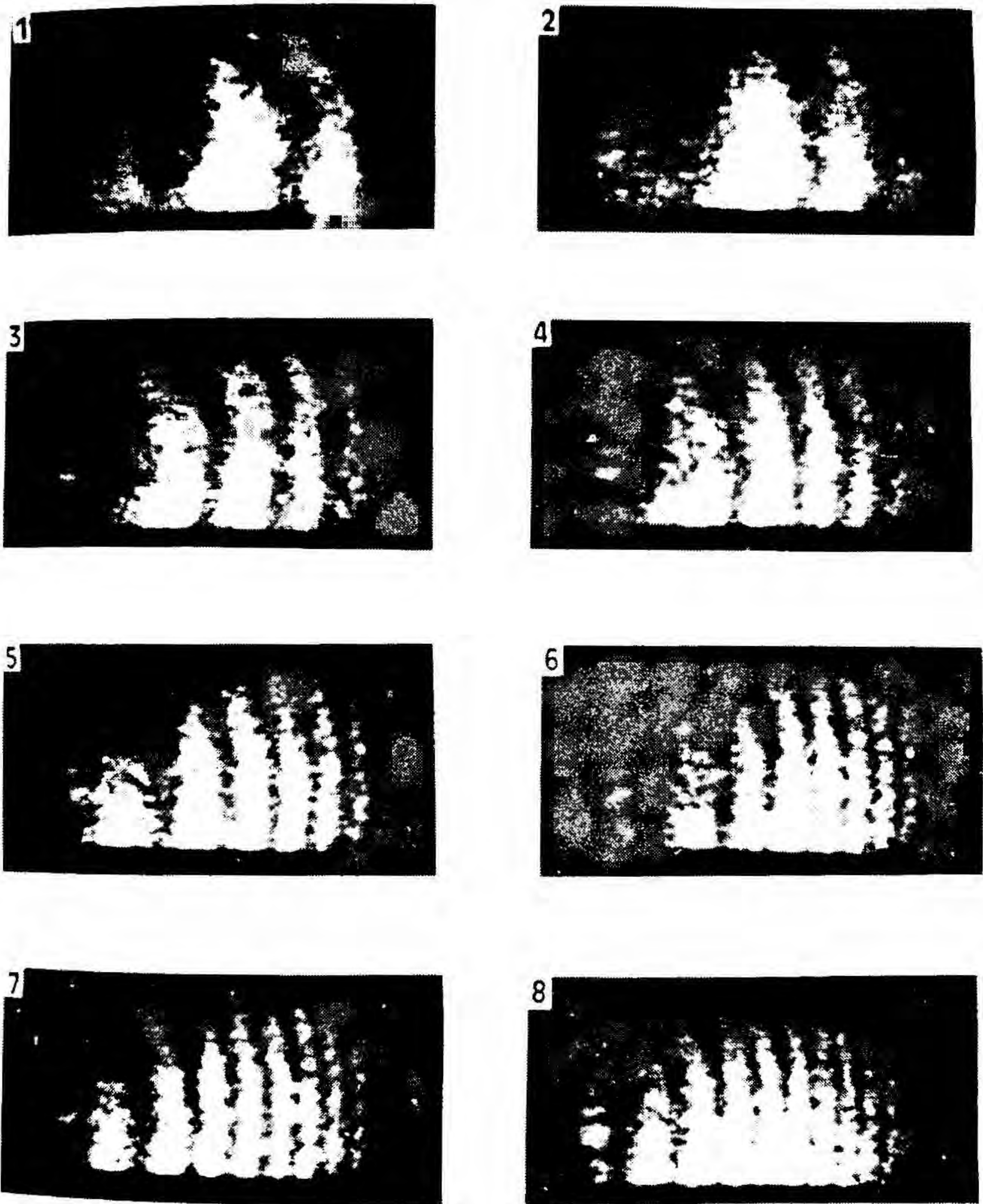


FIG. 1. Real-time holographic fringes: Aluminium film on glass substrate: Deflection of the cantilever at ΔT of: (1) 1.5, (2) 2, (3) 5.5, (4) 8.5, (5) 11, (6) 19.5, (7) 21 and (8) 24°C.

for the large discrepancy can be attributed to the error in the calculation of the theoretical stress. It is assumed in the theoretical calculation that the thermal expansion and Young's modulus of the thin film are the same as that of the

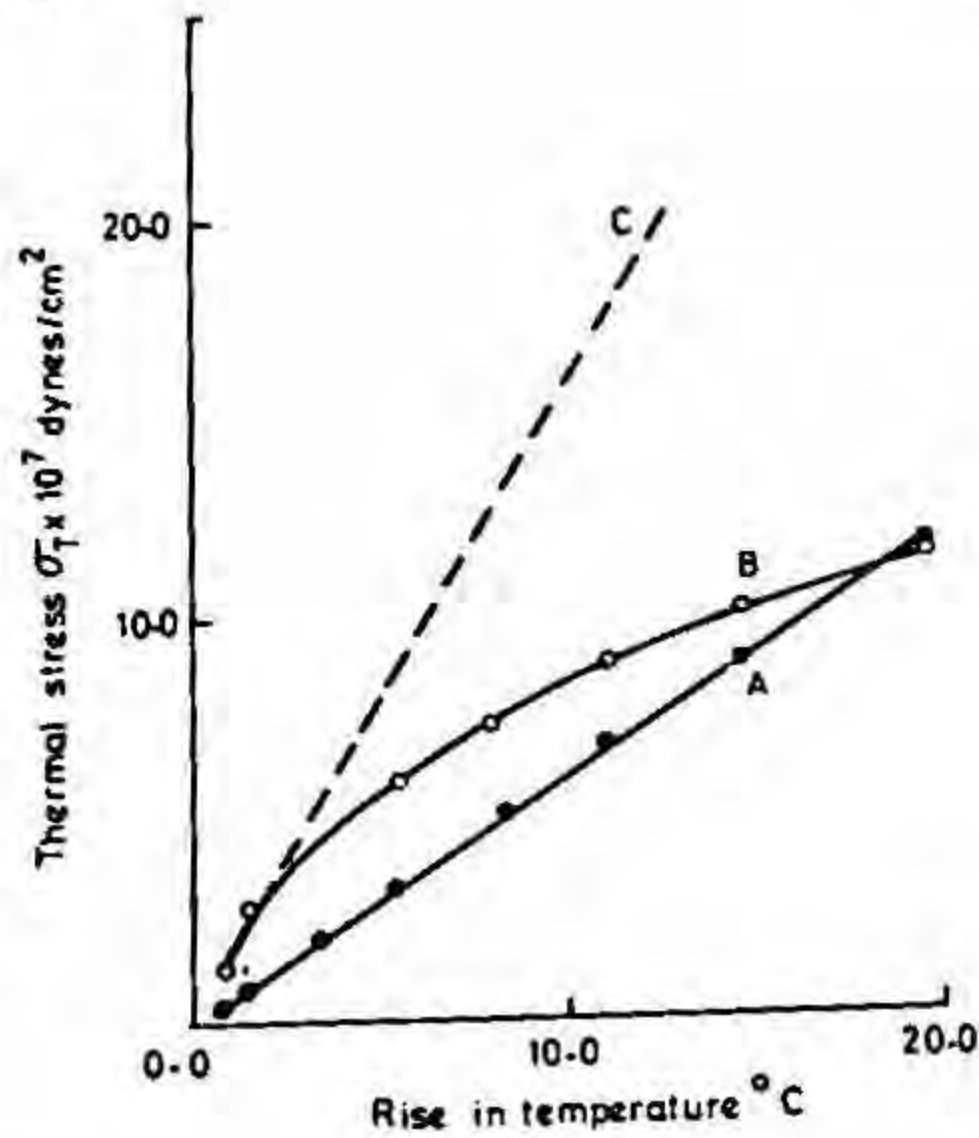


FIG. 2. Thermal stress against rise in temperature above ambient; $0.02 \mu\text{m}$ thick aluminium film. A. Theoretical σ_{T2} with $E_f/(1-\gamma_f)$ for film; B. σ_{Texp} experimental measured from deflection; C. Theoretical σ_{T1} with $E_f/(1-\gamma_f)$ for bulk material.

bulk material. This assumption is not usually true and probably gives rise to the discrepancy. Kuroda and Clyne⁴ have measured the thermal expansion coefficient of spray-coated aluminium films. It is reported that the thermal expansion coefficient is not drastically different from the bulk value, whereas the Young's modulus of elasticity is about 1/3 the value of the bulk material. It can be inferred from this that the use of the value of the Young's modulus of the bulk material for calculating the theoretical values is most likely to give higher thermal stress values than the measured value which does not assume the Young's modulus of elasticity of the film.

The thin film whose Young's modulus of elasticity is to be determined is coated on two different substrates under similar conditions. The thermal stress of the film on substrate 1 and 2 is plotted against ΔT in the same graph. The $E_f/(1-\gamma_f)$ value is determined graphically from the plot. This value is used to calculate the theoretical thermal stress.

Figure 2 gives a plot of the thermal stress σ_{T1} calculated using $E_f/(1-\gamma_f)$ of the bulk material, σ_{T2} calculated using the $E_f/(1-\gamma_f)$ of the film material obtained by the graphical method and σ_{exp} calculated from the measured deflection. It is seen from the graph that σ_{T2} and σ_{exp} agree closely. This reinforces the statement that the knowledge of the Young's modulus of elasticity of the thin film is essential for the correct prediction of the thermal stress using the theory.

4. Speckle-based fibre optic sensor

Speckle pattern is generated at the output end of a multimode optical fibre as a result of interference between different modes propagating within the fibre when coherent light is transmitted through it. If a physical parameter to be measured can cause a displacement of the speckle pattern in a multimode fiber, the two patterns can be recorded on a high-resolution photographic plate. The specklegram can now be analysed for measuring the displacement, from which one can measure the physical parameter. Speckle can be used as a sensitive indicator for sensing many parameters.

So far single-mode optical fibres, and interferometric sensing have been used for current and magnetic field sensing. In this work, speckle generated at the exit end of a multimode optical fibre is used for sensing current by measuring the speckle displacement.

A multimode pyrex glass fibre is fixed as a cantilever. A nickel jacket is mounted on the fibre at a suitable distance from the free end. A solenoid having a soft iron core is energised. When the coil is energised, the cantile-

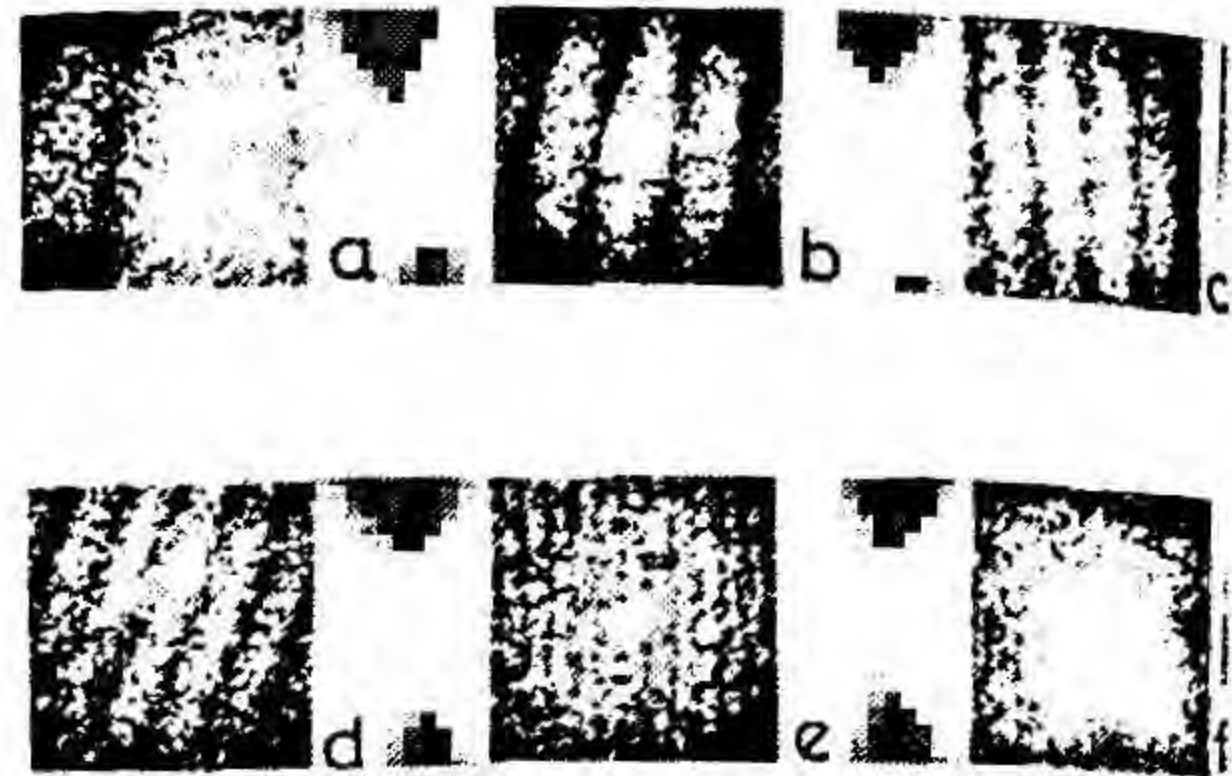


FIG. 3. Specklegram showing the Young's fringes for different currents, (a) 10, (b) 20, (c) 30, (d) 40, (e) 50 and (f) 60 mA.

ver bends. The photographic plate is exposed twice, once when the cantilever is static and the second time with the coil is energised. The developed photographic plate is a record of two superimposed speckle patterns. When the specklegram is placed in an unexpanded laser beam, Young's interference fringes are seen on a screen, placed a little distance away. When the current is high, the displacement of the cantilever is also high and the spacing between the fringes is small. As the current decreases the fringe spacing increases.

The current is raised from 10 to 60 mA for a fixed position of the nickel jacket and the gap between the core and the jacket. Some typical Young's fringes obtained from the doubly exposed specklegrams are shown in Fig. 3. It can be seen that the fringe spacing decreases as the current increases. The sensitivity could be increased by altering the loading distance and the gap.

The feasibility of a novel method of using fibre optic speckle for the measurement of current has been demonstrated.

References

1. HOFFMAN, R. W. The mechanical properties of thin condensed films. In *Physics of thin films*, Vol. 3, p. 211 (Hass, G. and Thun, R. E., eds.) 1966, Academic Press.
2. RAMPRASAD, B. S. AND RADHA, T. S. Thermal stress in thin films using real-time holographic interferometry, *Proc. Second Int. Conf. on Holographic Systems, Components and Applications*, IEE publication, No. 311, London, 29-32, 1989.
3. HARIHARAN, P. AND RAMPRASAD, B. S. Rapid *in-situ* processing for real-time holographic interferometry. *J. Phy. E. Sci. Instrum.*, 1973, 6, 699-701.
4. KURODA, S. AND CLYNE, T. W. The quenching stress in thermally sprayed coatings, *Thin Solid Films*, 1961, 200, 49-66.

Thesis Abstract (Ph.D.)

Studies on thin film pressure transducers and strain gauges by K. Rajanna

Research supervisor: S. Mohan

Department: Instrumentation and Services Unit

1. Introduction

Pressure transducers are electro-mechanical systems used to measure fluid pressure. The primary function of the pressure transducer is to sense fluid pressure and provide an electrical output proportional to the input pressure. Strain gauges¹ form an important component of the pressure transducers.

The present work involves the attempt made in the direction of preparation and study of pressure transducers with thin film strain gauges (having metal and alloy films as sensing films) as sensors. This work forms the major portion of the thesis. In addition, the preliminary investigations carried out on the suitability of Mn-SiO₂ cermet films and oxygen ion-implanted manganese films from strain gauge application are also included in the thesis. The necessary background information (on strain gauges and pressure transducers) and other related aspects of this film deposition are given.

2. Experimental

Part I: Design, fabrication and performance study of thin film pressure transducers

The various steps followed to prepare and study the behaviour of a thin film pressure transducer are: (i) Design and fabrication of the diaphragm assembly, (ii) Surface preparation, (iii) Deposition of insulating layers,

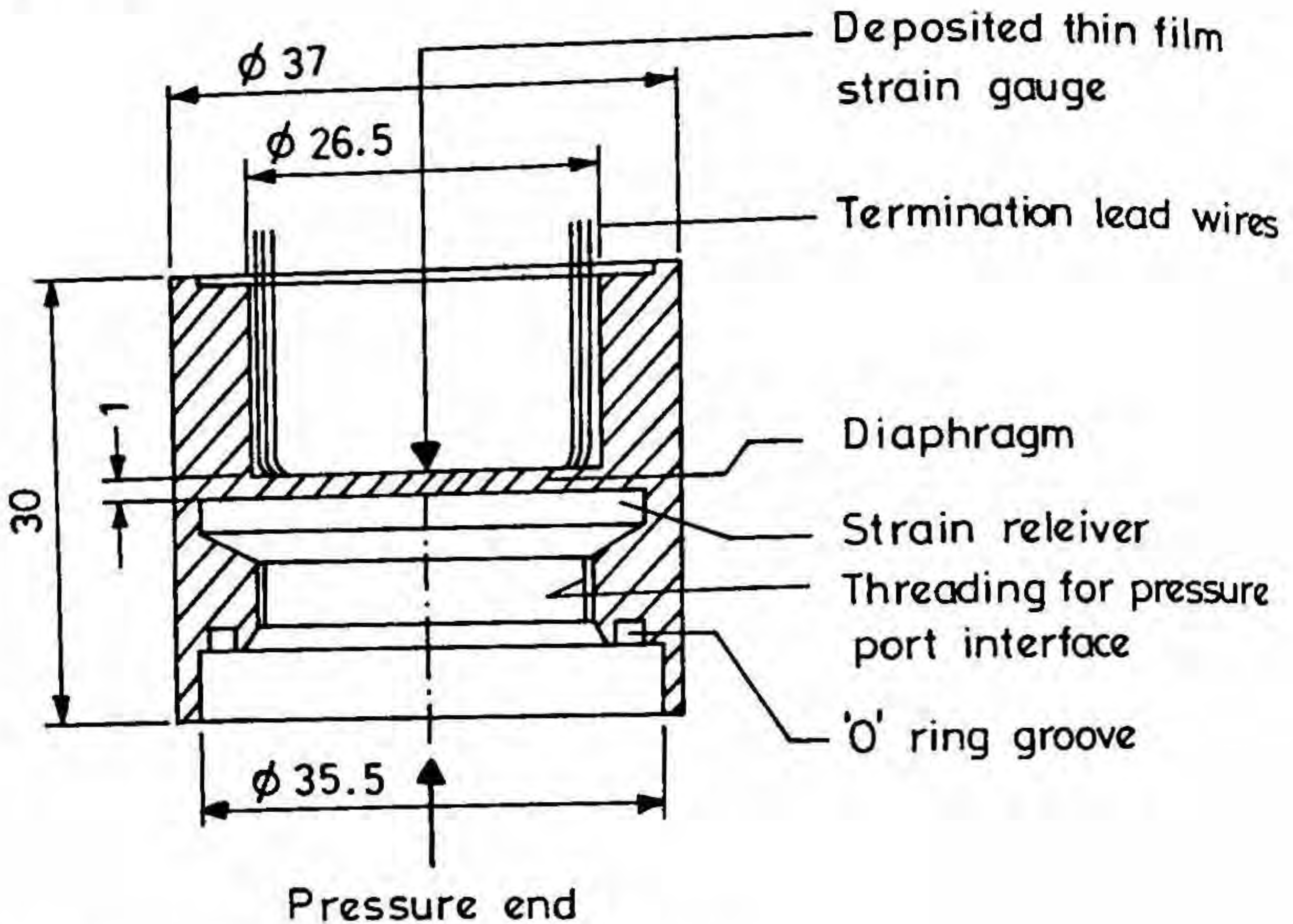


FIG. 1. Schematic of the diaphragm assembly (dimensions in mm).

(iv) Deposition of bonding pads and interconnecting pad films, (v) Deposition of sensing film (strain gauge film) and the protective overlayers, and (vi) Performance study of the thin film pressure transducer. For the sensing film manganese² and gold-nickel³ alloy films were used. Since very thin and discontinuous films are known to exhibit the problems of reproducibility and stability⁴ thin film strain gauges (sensing films) are prepared with a film thickness $\sim 1000 \text{ \AA}$. However, for Au-Ni film, because of its lower resistivity, in order to get adequate gauge resistance, film thickness $\sim 650 \text{ \AA}$ was maintained. The integrated diaphragm assembly (Fig. 1) is fabricated out of low carbon martensitic stainless steel. A special feature of this diaphragm design is the incorporation of strain-relieving cavity to take care of the strain due to mechanical handling, mounting or assembly process. The insulating oxide layers (Fig. 2) were deposited on the diaphragm in order to electrically isolate the sensing film from the metal diaphragm of the pressure transducer. The schematic of the optimised thin film strain gauge pattern deposited on the diaphragm is shown in Fig. 3. All the four gauges were made active by connecting them in a wheatstone bridge configuration and the output characteristics of the pressure transducer was studied.

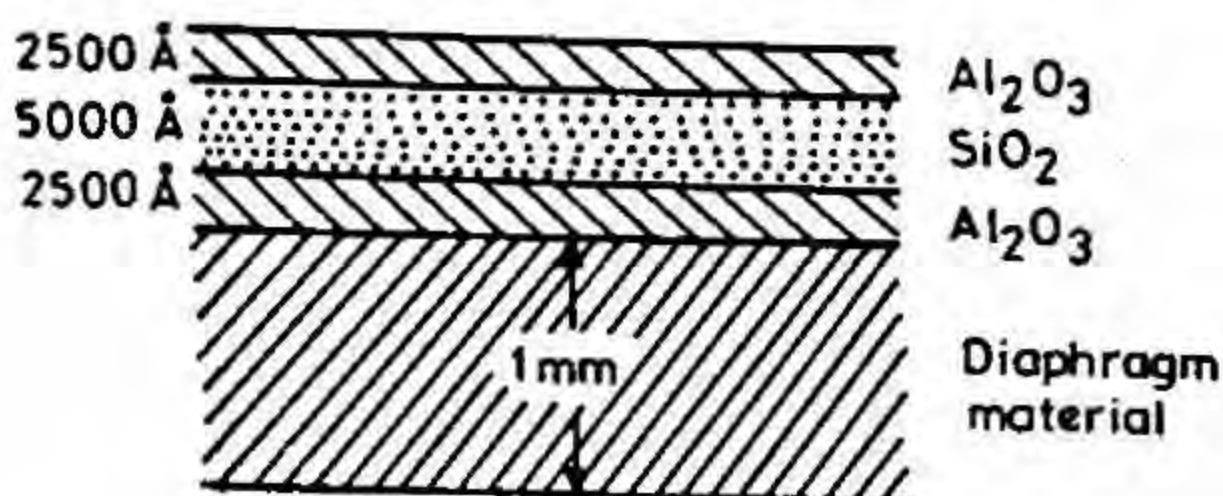
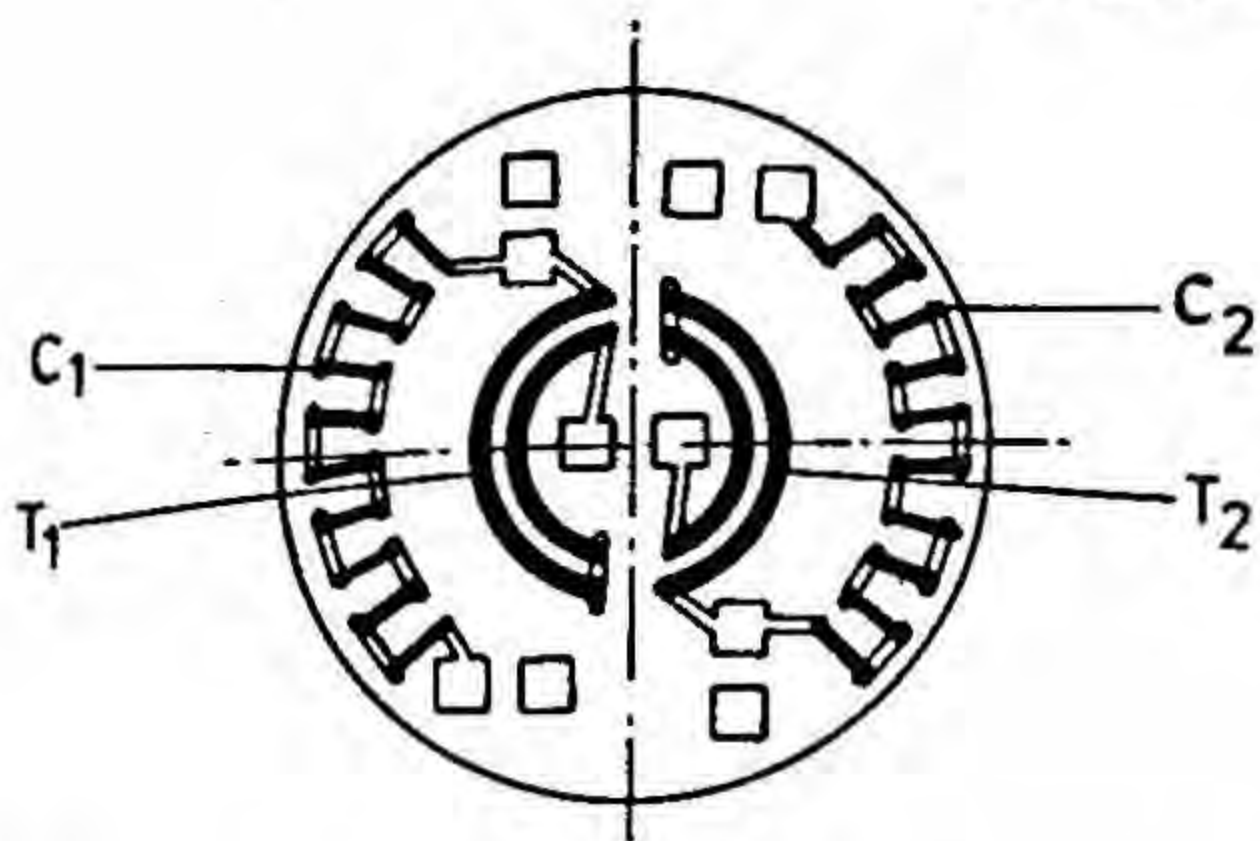


FIG. 2. Cross-sectional view of the insulating oxide layers on a pressure transducer diaphragm.



- Bonding pad for attaching the electrical leads;
- ≡ Interconnecting pads
- Sensing film

FIG. 3. Schematic diagram of the thin film strain gauge pattern.

Part II: Study on the suitability of Mn-SiO₂ cermet films for strain gauge applications

Mn:SiO₂ Cermet films of different compositions were prepared using co-evaporation method. The TCR (temperature coefficient of resistance) measurement of the films was carried out *in situ*. In order to study the resistance-strain characteristics and to measure the gauge factor of the Mn:SiO₂ cermet films, the four-point bending set up was used.

Part III: Study of ion-implanted Mn films with respect to strain gauge application

Manganese films of thickness $\sim 1000 \text{ \AA}$ were prepared by resistive evaporation. Oxygen ion implantation was carried out in a 150 keV ion implantation system at the Indira Gandhi Atomic Research Centre, Kalpakkam, India. Films were characterized using X-ray diffraction and electron microscopy techniques. Also, the gauge factor and TCR measurement was carried out for the films.

3. Results and discussion

Part I: Studies on thin film pressure transducers

For the thin film pressure transducer with four gauges active the maximum output achieved is $\sim 20 \text{ mV}$. An insulation resistance as high as $15000 \text{ M}\Omega$ was obtained in the case of insulating layers deposited by maintaining the diaphragm at 200°C . The maximum nonlinearity + hysteresis is in the range of 0.14 to 0.16% FSO (full scale output). The maximum deviation in all the above readings (nonlinearity + hysteresis) is within 0.04%. Further, it was found that the nonlinearity and hysteresis improved with the number of pressure cycles carried out over a period of eight months. The typical data obtained after 1000 cycles is 0.06% FSO. This is thought to be due to stress-relieving effects⁵.

Part II: Studies on Mn:SiO₂ cermet films

It was observed that the variation of resistivity of Mn:SiO₂ films is similar to that of other metal/SiO or SiO₂ cermet films⁶. It was found that the TCR value decreases considerably with the reduction of Mn percentage (to a value as low as $3.17 \times 10^{-5}/^\circ\text{C}$ for a Mn:SiO₂ composition of 40:60) and the sign gets changed (becomes negative) at 30:70 composition. The gauge factor value of Mn:SiO₂ cermet films was around 3 for films of composition up to 40:60 and a linear variation of relative change in resistance $\Delta R/R$ versus strain (ϵ) was observed⁷.

Part III: Studies on oxygen ion-implanted manganese films

It was found that the gauge factor value of oxygen ion-implanted Mn films increases with the increase in ion dosage. However, the increase in gauge factor is not very significant. Similar increase in gauge factor with ion dosage has been reported by Stroud⁸ in the case of oxygen ion-implanted titanium films. From the TCR measurement (by

annealing the film at different temperature intervals) it was found that: (i) the linear range (resistance versus temperature) gets enhanced as the annealing temperature is increased, (ii) TCR value is low at lower annealing temperatures, and (iii) gauge factor value does not change appreciably due to annealing.

References

1. RESINO, P. R. Thin film strain gauge transducers, *Instrum. Control Systems*, 1965, 38, 119-121.
2. RAJANNA, K., MOHAN, S., NAYAK, M. M. AND GUNASEKARAN, N. Thin film pressure transducer with manganese film as the strain gauge. *Sensors Actuators A*, 1990, 24, 35-39.
3. RAJANNA, K., MOHAN, S., NAYAK, M. M., GUNASEKARAN, N. AND MUTHUNAYAGAM, A. E. Pressure transducer with Au-Ni thin film strain gauges, *IEEE Trans.*, 1993, ED-42, 521-524.
4. CHOPRA, K. L. AND KAUR, I. *Thin film device applications*, p. 169, 1983, Plenum Press.
5. PARKER, R. K. AND KRINSKY, A. Electrical resistance strain characteristics of thin evaporated metal films, *J. Appl. Phys.*, 1963, 34, 2700-2708.
6. NEGEBANER, C. A. Resistivity of cermet films containing oxides of silicon, *Thin Solid Films*, 1970, 6, 443-447.
7. RAJANNA, K., SRINIVASULU, S., NAYAK, M. M. AND MOHAN, S. Suitability of Mn:SiO₂ cermet films for strain gauge applications, *J. Mater. Sci. Lett.*, 1993, 12, 37-39.
8. STROUD, P. T. Some effects of strain and temperature on the resistance of oxygen ion implanted titanium thin films, *Thin Solid Films*, 1972, 10, 205-215.

Thesis Abstract (M. Sc. (Engng))

Algorithms for some problems on trees and graphs by Naveen Gabrani

Research supervisor: Priti Shankar

Department: Computer Science and Automation

1. Introduction

Design and analysis of graph algorithms is an active area of research in computer science. Trees form an important subclass of graphs and have vast applications. In this thesis, we present some new algorithmic results on trees. We also present certain additional results in algorithmic graph theory.

2. Construction of a binary tree from its traversals

Given the inorder and preorder traversals of a binary tree, the original binary tree can be uniquely identified. We present a very simple linear time algorithm for the problem of constructing a binary tree from its inorder and preorder traversals¹. The algorithm leads to an optimal $O(\log n)$ time parallel algorithm on the EREW PRAM model. Independently, other authors have also given optimal sequential and parallel algorithms for the problem^{2,3}, but our algorithm is the simplest known algorithm for the problem.

3. 321-avoidable permutations

A permutation of number $1, 2, \dots, n$ is a 321-avoidable permutation, if it has no subsequence $p_i p_j p_k$ such that $p_k < p_j < p_i$. 312-avoidable and 231-avoidable permutations are similarly defined. The number of binary trees of n nodes is known to be equal to the number of 321-avoidable permutations of size n . However, no direct correspon-

dence is known for this interesting result. We give a simple one-to-one correspondence between binary trees of n nodes and 321-avoidable permutations of size n . We give new characterizations of 321-avoidable permutations in terms of data structure queue. Using this characterization, we give a one-to-one correspondence between 321-avoidable permutations of size n and legal parenthesis sequences of size $2n$. The properties of 312-avoidable and 231-avoidable permutations are well known⁴. By giving new characterizations of 321-avoidable permutations, we have tried to fill a gap in the literature.

4. Generation of combinatorial objects in constant time

A generation algorithm is called loopless, if the amount of computation to go from one object to the next is bounded by a constant. Recently, Baronaigien has given a loopless algorithm for the problem of generation of all binary trees of n nodes⁵. We give the first loopless algorithms for the following problems.

- (a) generation of all k -ary trees of n nodes.
- (b) generation of all binary trees with a given degree sequence.
- (c) generation of all legal parenthesis sequences of size $2n$.

To our knowledge these are the first loopless generation algorithms for all of these problems⁵. All the existing algorithms for the generation of k -ary trees, take $O(n)$ time in the worst case⁵.

5. Repair of tree generating regular systems

The tree-to-tree correction problem has been designed by Tai⁶ who has also given an algorithm that computes the minimum cost edit sequence needed to transform one tree to another. Zhang and Shasha⁷ have improved upon this algorithm. An extension of this problem is the problem of repair of tree generating regular systems. The problem is formally defined as follows: Given a binary tree α and a binary tree automation M , the problem is to compute a binary tree β of the tree language defined by M which is 'nearest' (in number of edit operations) to α . Using a dynamic programming approach, we present an algorithm which takes time linear in number of vertices of the tree, assuming that the number of states of the tree automation is constant.

6. Permutation graphs and memory allocation

Recently Kim⁸ has given an $O(n \log n)$ time algorithm for the problem of computing a maximum independent set of a permutation graph. We give a much simple $O(n \log n)$ time algorithm for the problem. We use this algorithm to solve a problem in memory allocation in $O(n \log n)$ time. This compares favourable with the earlier known $O(n^2)$ time algorithm for the problem⁹.

7. Infinite line problem

We give two simple randomized algorithms for the problem of online traversal of layered graphs of width two. The algorithms achieve competitive ratios of 5.5 and 7. The previous best algorithm for the problem was the optimal deterministic algorithm, which achieves a competitive ratio of 9¹⁰. We also prove a lower bound of 2.5 on the competitive ratio of any randomized algorithm for the problem.

References

1. GABRANI, N. AND SHANKAR, P. A note on the construction of a binary tree from its traversals, *Inform. Process. Lett.*, 1992, 42, 117-119.
2. OLARIU, S., OVERSTREET, C. AND WEN, Z. An optimal parallel algorithm to construct a binary tree from its traversals, *Proc. Int. Conf. on Computing and Information*, Ottawa, 1991.
3. VAN DE SNEPSCHEUT Inversion of a recursive tree traversal, *Inform. Process. Lett.*, 1991, 39, 265-267.
4. MAKINEN, E. A survey on binary tree codings, *Comput. J.*, 1991, 34, 438-443.

5. ROELANTS VAN BARONAIGIEN, D. A loopless algorithm for generating binary tree sequences, *Inform. Process. Lett.*, 1991, 39, 189-194.
6. KUO-CHUNG TAI The tree-to-tree correction problem, *JACM*, 1979, 26, 422-433.
7. ZHANG, K. AND SHASHA, D. *On the editing distance between trees and related problems*, NYU Computer Center, Technical report 310, August 1987.
8. KIM, H. Finding a maximum independent set in a permutation graph, *Inform. Process. Lett.*, 1990, 36, 19-23.
9. EVEN, S., PNUELI, A. AND LEMPEL, A. Permutation graphs and transitive graphs, *JACM*, 1972, 19, 400-410.
10. PAPADIMITRION, C. H. AND YANAKAKIS, M. Shortest paths without a map, *Theor. Comput. Sci.*, 1991, 84, 127-150.

Thesis Abstract (M. Sc. (Engng))

A stochastic dynamical system for edge detection by K. Uma

Research supervisor: V. S. Borkar

Department: Electrical Engineering

1. Introduction

Increasing interest in pattern recognition and its use in various fields have necessitated the availability of faster and better techniques of edge detection. The conventional methods of edge detection are not reliable in the presence of noise. Stochastic techniques, which perform well under noise, have been found to be too slow to be of practical use.

2. Contributions of the thesis

In this thesis, we propose a different approach to edge detection. The algorithms proposed are stochastic and hence perform well even in the presence of noise. In contrast to conventional algorithms, we define the state space to be the pixel array so that any point of the state space is a single pixel instead of an entire edge configuration. This results in a drastic reduction in time taken.

We first define a time-homogenous Markov chain over the state space. The transition probability of the Markov chain is the same as the one used in Monte Carlo algorithms. The edge detection algorithm is based on the limiting behaviour of this Markov chain¹. The cost is defined in a suitable manner so that the invariant distribution has high mass at edge points, thereby facilitating the detection of edges. The invariant distribution of the Markov chain is approximated by the long-run mean fraction of time that the chain spends at any pixel². Thus, a count is maintained to keep track of the number of visits that the Markov chain makes to each site. The edges are finally detected by a simple thresholding. A simple heuristic has been used to determine the threshold.

In order to overcome some of the shortcomings of the sequential algorithm, an independent parallel algorithm has been proposed. A Markov chain is started at every pixel of the state space. Each of these chains is allowed to select a site from one of its neighbouring sites and accept it according to prescribed selection and acceptance probabilities, which are the same as those employed in the sequential algorithm. If, however, two or more processes enter a site, the processes coalesce and move thereafter as a single process. Thus, for a fixed chain, the process is a copy of the process defining the sequential version described earlier and therefore exhibits the same dynamics as the sequential algorithm. The different chains, however, are not independent and are, in fact, highly correlated. A new quantity is defined at each site, viz., the number of processes currently at a site. If a neighbouring site is 'accepted', all the processes currently at the site are transferred to the new site. If it is not accepted, the processes remain at the current site. It has been shown that the limiting distribution of such a system exists and is proportional

to the invariant distribution of a single chain. It has also been shown that the sequential and the parallel algorithms are asymptotically equivalent. The advantages of the parallel algorithm are the following:

1. No *ad hoc* modifications are required to take care of initial conditions or non-zero gradient along the edge.
2. No explicit count is required to be maintained with respect to time.
3. The threshold on the number of processes has been set to 0. This simplifies any hardware implementation of the edge detector.

The parallel algorithm with its localised interactions facilitates the casting of the problem as a neural network³. The structure of the neural network consists of three layers—an input layer, an intermediate layer which computes the number of processes at each site and the output layer which detects edges through a simple thresholding.

3. Results and conclusions

The algorithms proposed provide a much faster technique of edge detection while preserving the advantages of stochastic algorithms with respect to robustness in the presence of noise. The algorithms were found to perform much better than the Canny's and the Marr-Hildreth operator while taking comparable time for execution. On the other hand, they were found to perform much better than other stochastic algorithms like simulated annealing in terms of time taken. Possible extensions of this technique to other problems like segmentation, pattern classification, etc., have also been discussed.

References

1. MITRA, D., ROEMO, F. AND SANGIOVANNI-VINCENTELLI, A. Convergence and finite-time behaviour of simulated annealing. *Adv. Appl. Probab.*, 1986, 18, 747-771.
2. SENETA, E. *Non-negative matrices and Markov chains*, 2nd edn, 1980, Springer-Verlag.
3. HOPFIELD, J. J. Neural networks and physical systems with emergent collective computational abilities, *Proc. Natn. Acad. Sci. USA (Biophysics)*, 1982, 2554-2558.

Thesis Abstract (M. Sc. (Engng))

Creep behaviour of Ti-24Al-11Nb alloy by R. S. Sundar

Research supervisor: D. H. Sastry

Department: Metallurgy

1. Introduction

In recent years efforts have been made to develop alloys based on Ti_3Al ¹. Of these, Ti-24Al-11Nb (at%) is very attractive in view of its high strength and optimum combination of low-temperature ductility and creep resistance. However, it is necessary to optimize the microstructure of this two-phase alloy to yield the best mechanical properties. The aim of the present work is to investigate the effect of microstructure on the creep deformation of this alloy.

2. Experimental

The Ti-24Al-11Nb alloy was received in the form of 12 mm-dia rod. Specimens of 5 mm height were subjected to heat treatments (Table I). Microstructures were observed by optical microscopy and standard quantitative metallography was employed to estimate the volume fraction of the phases. The preferred orientation

Table I
Heat treatments

-
- (i) $\alpha_2 + \beta$ Heat treatments
- a) 1333 K/4 h/WQ + 1173 K/24 h/AC
 - b) 1333 K/4 h/AC + 1173 K/24 h/AC
 - c) 1333 K/4 h/FC + 1173 K/24 h/AC
- (ii) β Heat treatments
- a) 1403 K/1 h/AC + 1173 K/24 h/AC
 - b) 1423 K/1 h/CC + 1173 K/24 h/AC
 - c) 1423 K/1 h/FC + 1173 K/24 h/AC
-

WQ—water quenched; AC—air cooled;
FC—furnace cooled; CC—controlled cooled (0.1°/s).

developed in the as-received material during processing was identified by X-ray diffractometry. The impression creep technique^{2,3} was employed, wherein tungsten carbide indenters of 1.5 mm dia and with a flat bottom were used. The depth of penetration of the indenter was continuously monitored with an LVDT with a sensitivity of $\pm 1 \mu\text{m}$. The creep testing was carried out in the range of 923–1053 K and at each temperature the dependence of the steady-state creep (*i.e.*, the steady-state impression velocity of the indenter) on the applied stress was determined.

3. Results and discussion

3.1. Microstructure

The examination of the surface which is parallel to rolling direction (RD), in as-received condition, reveals the aligned fine $\alpha_2(\text{Ti}_3\text{Al})$ grains along the RD in β (high temperature bcc phase) matrix. Heat treating in the two-phase region, *i.e.*, $\alpha_2 + \beta$ heat treatment, results in the formation of equiaxed α_2 . Furnace cooling and aging (FC) results in the formation of transformed β at α_2 grain triple points. In air-cooled and aged samples (AC) transformed β is found as ribbons around the primary α_2 grains. The microstructure in water-quenched and aged samples (WQ) is similar to that of AC condition with higher amount of transformed β . In the case of β heat treatment, furnace cooling (β -FC) from β phase region and aging at 1173 K results in coarse aligned α_2 laths with less amount of β between the laths. Intermediate cooling rate (0.1 K/s) results in the formation of basket weave microstructure (β -CC) and fast cooling from the single-phase region results in the formation of fine α_2 laths with higher amount of β .

Impression creep curves, *i.e.*, impression depth vs time curves in all the microstructural conditions are similar to those of conventional creep curves in that the indenter penetrating velocity initially decreases with time and thereafter reaches a steady state. The indenter velocity and stress in impression creep test are transformed into the equivalent tensile creep rate and uniaxial stress following the relationships given by Chu and Li² and Murthy and Sastry³.

3.2. Creep behaviour in as-received material

To bring out the possible effect of texture on creep behaviour, tests were carried out at 923 K on the as-received material with the indenter axis a) perpendicular to the RD, and b) parallel to rolling direction. The stress dependence of creep rate is presented in Figs 1a and b shows the corresponding X-ray diffractograms. The sample when tested with indenter axis perpendicular to the RD shows better creep resistance compared to the one when the stress axis is parallel to RD. Texture developed during processing results in the orientation of (0002) planes along, and (20 $\bar{2}$ 0) planes perpendicular, to RD. These are the main operating slip planes in Ti_3Al . The resolved stress in these planes is low when indentation is made in the surface containing the RD.

Hence, the dislocation motion in the above planes is restricted, which results in better creep resistance in this specimen compared to the specimen with indentation in the surface perpendicular to RD.

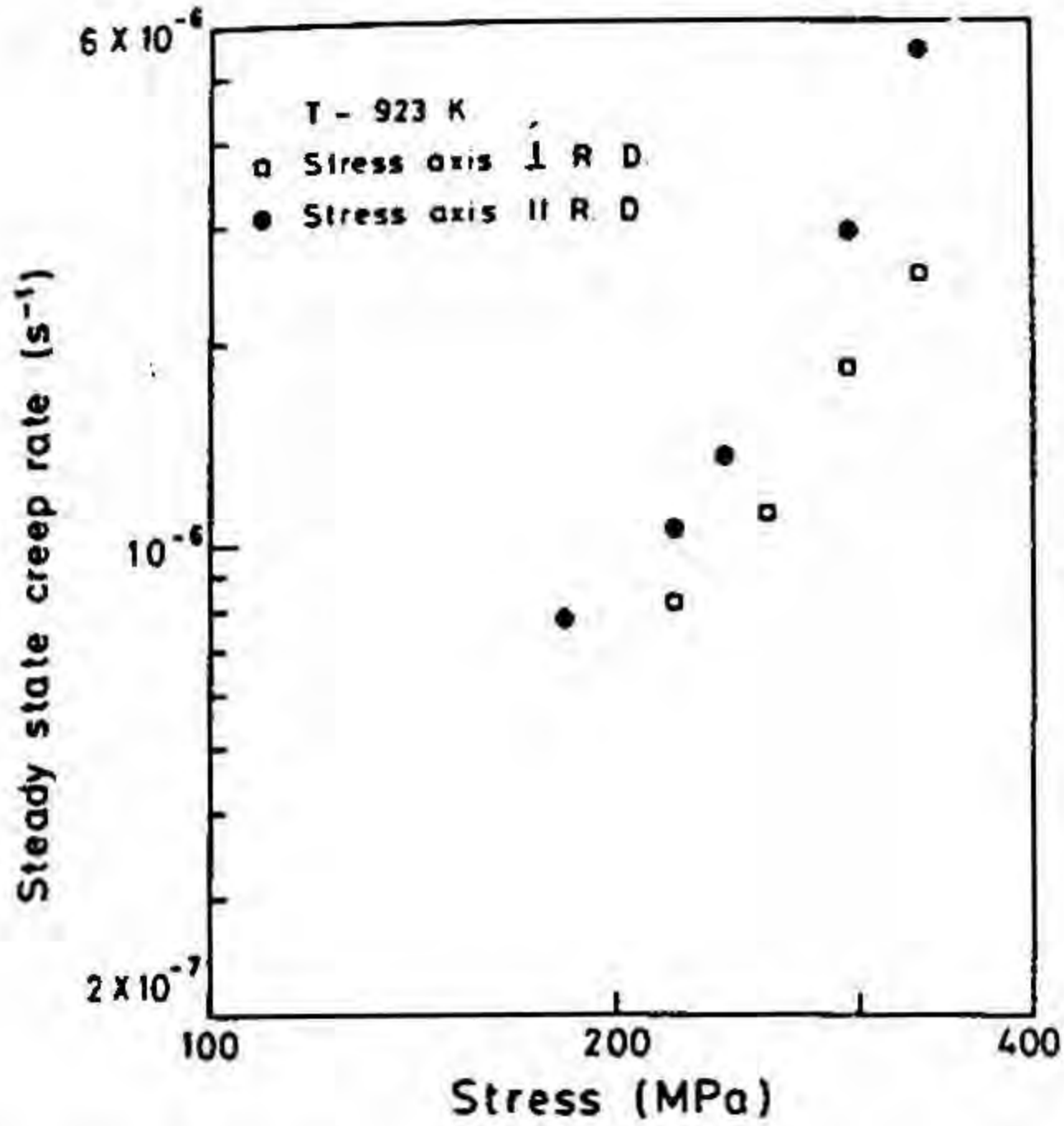


FIG. 1a. Stress dependence of steady-state creep rate in the as-received condition.

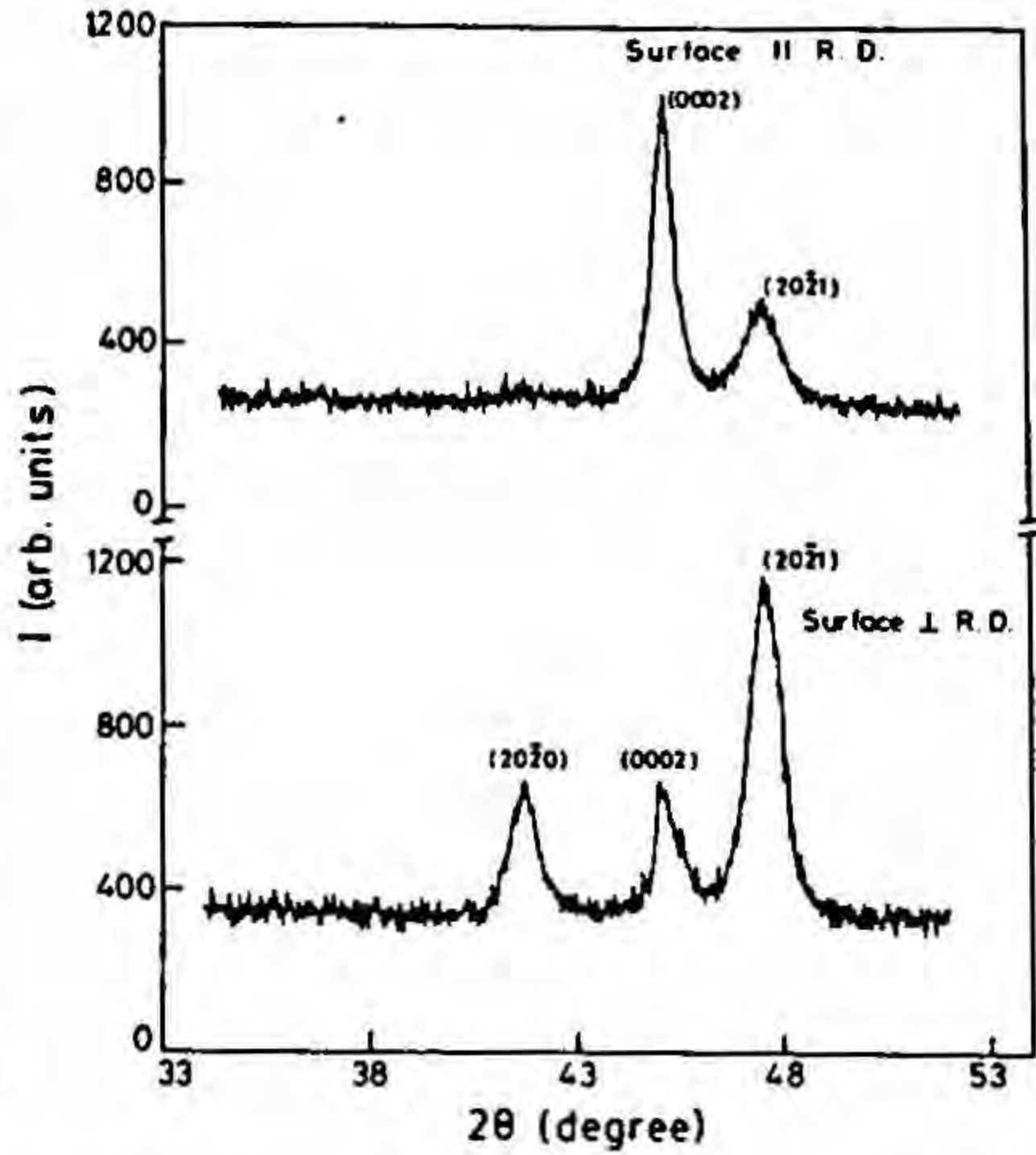


FIG. 1b. X-ray analysis of the as-received alloys exhibiting texture in the α_2 phase.

3.3. Creep behaviour in $\alpha_2 + \beta$ heat-treated condition

The stress dependence of steady-state creep rate for AC condition is presented in Fig. 2. Generally, a power law creep is obeyed with a stress exponent for steady-state creep rate (n) greater than 3. However, a change in slope with $n \approx 1$ is observed in the low stress region especially at higher temperatures. Similar trend is ob

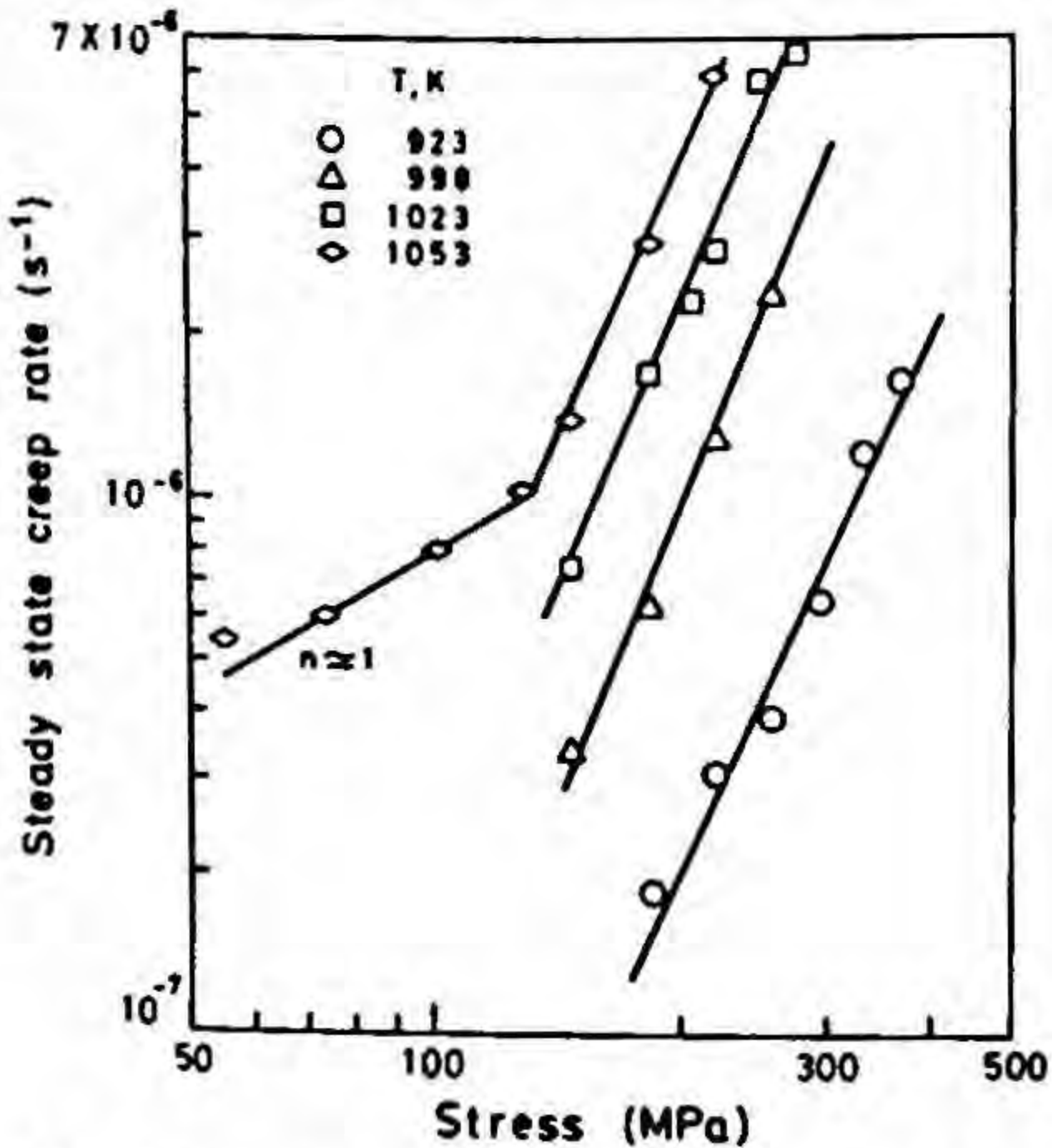


FIG. 2. Stress dependence of steady-state creep rate in the $\alpha_2 + \beta$ AC condition.

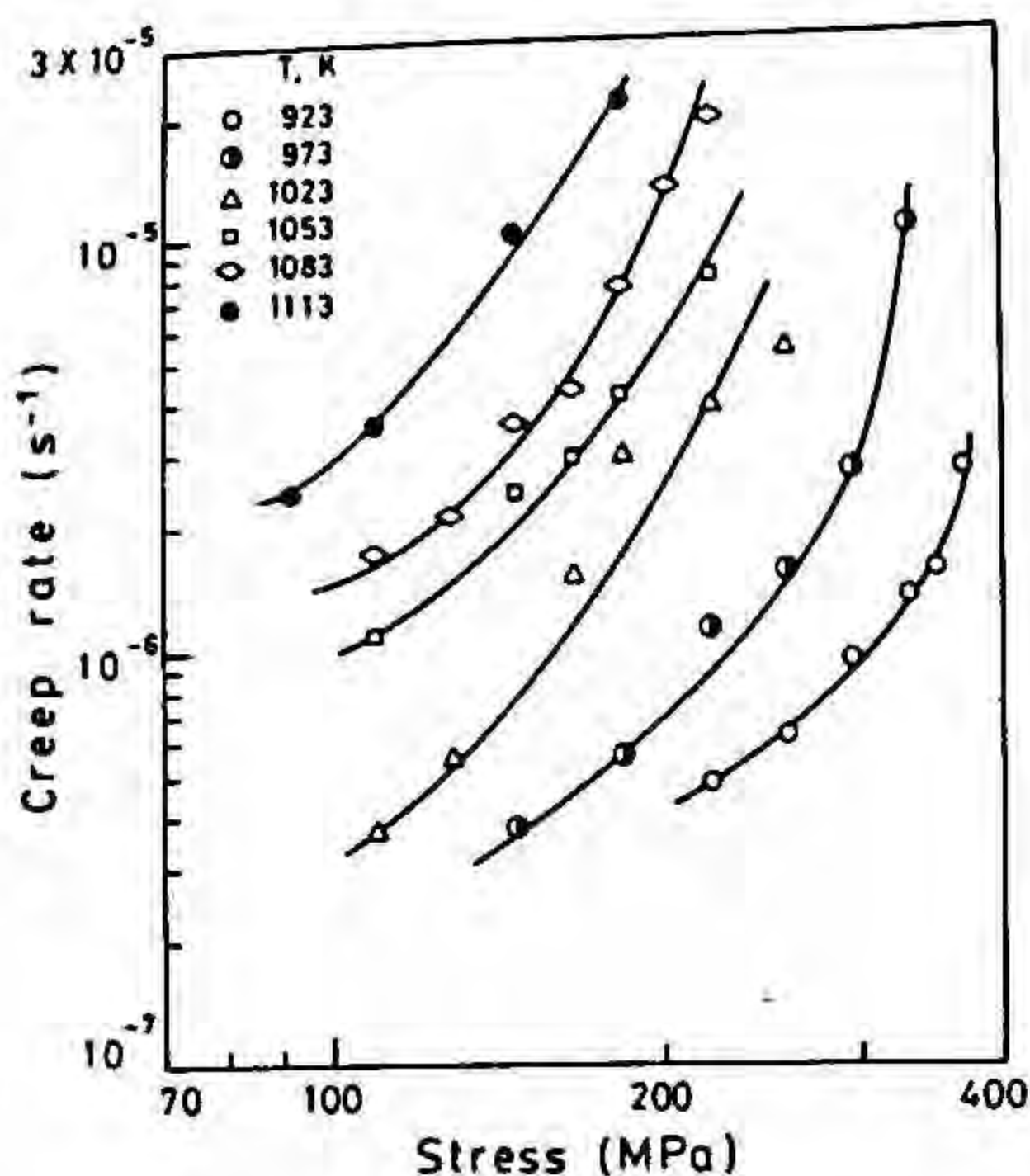


FIG. 3. Stress dependence of steady-state creep rate in the $\alpha_2 + \beta$ FC condition.

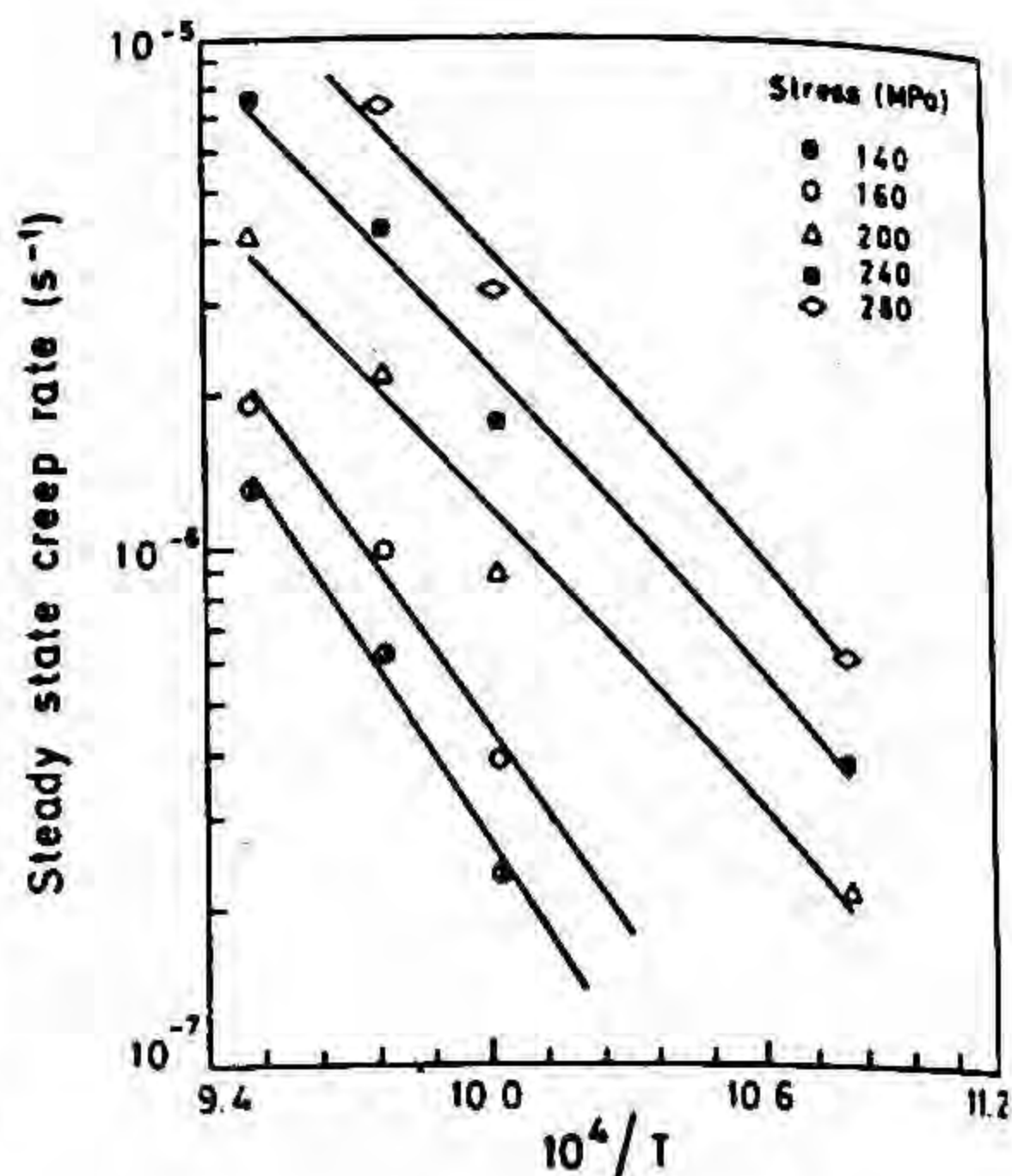


FIG. 4. Arrhenius plot showing the temperature dependence of the steady-state creep rate in $\alpha_2 + \beta$ AC condition.

served in WQ condition also. But in the FC condition, the data showed a nonlinear behaviour (Fig. 3). This behaviour may be attributed to the variation of pre-exponential factor, P , in the Arrhenius rate equation ($\dot{\epsilon} = P \exp(-Q/RT)$) or to possible microstructural changes that occur with time/stress/temperature. However, optical microscopic observation of the sample before and after testing did not reveal any appreciable change in microstructure. For further clarification of this point TEM examination is required. The temperature dependence of the steady-state creep rate in AC condition is shown in Fig. 4. The Arrhenius plot yields an apparent activation energy (Q_c) in the range 190–270 kJ/mole. Similarly, in the WQ condition the activation energy lies between 200 and 260 kJ/mole. In both the cases, the activation energy shows a stress dependence; Q_c decreases with stress and the activation energy at zero stress is between 500 and 600 kJ/mole.

The cooling rate from the two-phase region has a definite effect on the creep behaviour. At 923 K, the WQ sample shows better creep resistance in comparison with AC-cooled samples and FC treatment results in minimum creep resistance. This may be attributed to the strengthening effect of the β phase. It is present in highest portion in WQ condition which shows minimum creep rate among the three microstructures at 923 K. It is reported by Gittis and Kross⁴ that the β phase starts deforming easily above 923 K probably owing to its open structure. Thus, easy deformation of β nullifies the difference between WQ and AC condition at 1023 K. However, at 1053 K, the presence of higher amount of β increases the creep rate in the WQ condition compared to AC condition. FC heat-treated microstructure shows poor creep resistance throughout the temperature range of present investigation. This can be explained on the basis of the role of the interphase boundaries in deformation. In FC the interphase boundaries are restricted to grain boundary triple points compared to the continuous interphase boundaries in the other two heat-treatment conditions. These interphase boundaries act as effective barriers to dislocation motion⁵. Hence, FC condition which has less number of interphase boundaries showed poor deformation resistance.

3.4. Creep behavior in β heat-treated condition

Creep tests were conducted in β -CC at four different temperatures, namely, 923, 973, 1023 and 1053 K and over a stress range of 140–440 MPa. Also to bring out the effect of cooling rate from β solutionizing temperature,

creep tests were conducted on β -AC and β -FC samples at 923 K and 370 MPa. In β -CC condition also a power law creep is seen to be observed with n values ranging between 6.7 and 8.4. The calculated apparent activation energy lies in the range 340–400 kJ/mole, decreasing with stress.

Among the β heat-treated samples, the intermediate cooling rate (β -CC) yields maximum creep resistance. This is attributed again to the overall contribution of two opposing microstructural factors which change with cooling rate, namely, inferior creep resistance due to a large amount of β phase and the beneficial effect of smaller α_2 plate size. Microstructure produced by intermediate cooling rate possesses optimum combination of these two factors and thus shows better creep resistance compared to the other two.

3.5. Rate-controlling mechanism of creep

At lower stresses, the observed stress exponent of unity is indicative of a diffusional mechanism such as Nabarro–Herring creep. At higher stresses, the stress exponent is greater than 3. The activation energy for creep is stress dependent and the activation energy for the barrier at zero stress is greater than that of self diffusion in Ti. The results are not in agreement with the dictates of diffusion-controlled mechanisms such as dislocation climb. The data suggest that a cross slip mechanism or a mechanism based on the unpinning of attractive junctions may control the steady-state creep rate at high temperatures.

4. Conclusions

The creep behaviour of Ti–24Al–11Nb alloy is found to be sensitive to the crystallographic texture as well as to the details of microstructure. Best creep resistance is shown when the microstructure contains smaller α_2 plates and a lower β volume fraction. In general, a power law creep behaviour is observed in all the microstructures. At lower stresses, a diffusional mechanism seems to be operating. At higher stresses either a cross slip mechanism or a mechanism involving unpinning of the attractive junctions controls the creep rate.

References

1. ROWE, R. G. *In High temperature aluminides and intermetallics*, (Whang, S. H. and Liu, C. T. and Pope, D., eds), 1990, Warrendale, TMS.
2. CHU, S. N. G. AND LI, J. C. M. *J. Mater. Sci.*, 1977, 12, 2200–2208.
3. MURTHY, G. S. AND SASTRY, D. H. *Phy. Stat. Sol. (a)*, 1983, 70, 63–71.
4. GITTIS, S. J. AND KOSS, D. A. *In High temperature ordered intermetallic alloys III* (Liu, C. T., Tabu, A. I., Stoloff, N. S. and Koch, C. C., eds), Vol. 133, 1988, p. 323–328, MRS, Boston.
5. CHO, W., THOMPSON, A. W. AND WILLIAMS, J. C. *Met. Trans. A*, 1990, 21, 641–651.

Thesis Abstract (Ph.D.)

Synthetic, spectroscopic and structural investigations on cyclic and acyclic phosphazanes and their transition metal complexes by R. Murugavel

Research supervisor: S. S. Krishnamurthy

Department: Inorganic and Physical Chemistry

1. Introduction

A wide variety of phosphorus–nitrogen compounds are known with the coordination number around the phosphorus atom varying from two to six¹. Cyclic and acyclic P(III)–N compounds have proven to be useful ligands in transition metal chemistry². The present study deals with synthetic, spectroscopic and structural investigations on a range of phosphorus–nitrogen compounds and their transition metal complexes in order to probe and understand

the nature of the P-N bond which is one of the most intriguing in chemistry. In particular, the six-membered P_3N_3 ring compounds (λ^3 -cyclotriphosphazanes) are investigated extensively owing to their interesting conformational and structural features³. Moreover, this class of compounds would be useful ligands in transition metal chemistry as they possess three tricoordinate phosphorus atoms in close proximity. The present investigation also deals with the synthesis of a new λ^5 -bicyclic phosphazane, the reactions of $[MeNPCI_3]_2$ with primary aromatic amines and X-ray crystal structures of two transition metal complexes formed by acyclic λ^3 -diphosphazanes.

2. Results and discussion

2.1. λ^3 -Cyclotriphosphazanes

A series of new aryloxy- and trifluoro-ethoxy λ^3 -cyclotriphosphazanes, $[EtNP(OR)]_3$ ($R = C_6H_5$, 1; C_6H_4Br -4, 2; $C_6H_3Me_2$ -3,5, 3; $C_6H_3Me_2$ -2,6 4; CH_2CF_3 , 5; have been prepared as *cis-trans* isometric mixtures from the reactions of chlorocyclotriphosphazane⁴ $[EtNPCI_3]$ with the respective phenols or trifluoroethanol. The new compounds have been characterized by IR and NMR spectroscopy. The molecular conformations of *cis* and *trans* isomers of $[EtNP(OC_6H_4Br-4)]_3$ (2) have been established by X-ray crystallography. The *cis* isomer exhibits a flattened chair conformation and the *trans* isomer a boat conformation with the substituents on phosphorus occupying axial positions. The *cis* and *trans* isomer of λ^3 -cyclotriphosphazanes on oxidation with either Me_3NO or H_2O_2 yield λ^5 -trioxocyclotriphosphazanes.

Ab-initio calculations on the model ring compounds $[XPNH]_3$ ($X = H, F$) suggest that the pseudo-axial form for the P-X group is favoured over the equatorial form. The conformational preferences of these molecules are mainly determined by the lone pair-lone pair and electrostatic dipolar repulsions and negative hyperconjugative interactions resulting from the interaction of the nitrogen lone pair with an adjacent P-X σ^* orbital⁵⁻⁷. The calculations further indicate that the axial \rightarrow equatorial conversion has a high energy barrier.

2.2. Transition metal complexes of λ^3 -cyclotriphosphazanes

The 2,6-dimethylphenoxy derivative, *trans*- $[EtNP(OC_6H_3Me_2-2,6)]_3$ (4) reacts with $[Mo(CO)_4(NBD)]$ to yield the chelate complex, $[Mo(CO)_4]$ (6) while *cis*- $[EtNP(OCH_2CF_3)]_3$ (5) yields the dinuclear complex $[Mo(CO)_4(\mu-5)]_2$ (7). These complexes represent the first examples of organometallic derivatives of λ^3 -cyclotriphosphazanes. Crystal structures of both the complexes have been determined. A pyramidal geometry observed around the nitrogen atom flanked by the coordinated phosphorus atoms in $[Mo(CO)_4(4)]$ (6) is unprecedented among λ^3 -phosphazanes.

2.3. Bicyclic phosphazanes

The treatment of 2,6-dimethylphenol with the λ^3 -bicyclic phosphazane $Cl_2P_4(NEt)_5$ yields a mixture of tetraphosphazane oxides, $[P_4O_n(NEt)_5(OC_6H_3Me_2-2,6)_2]$ ($n = 0, 1$ or 2). This mixture on treatment with H_2O_2 in THF yields the tetroxide, $[P_4O_4(NEt)_5(OC_6H_3Me_2-2,6)_2]$ (8). The structure of this compound has been determined by X-ray crystallography; the molecule is made up of two P_3N_3 rings fused by a common PNP fragment.

2.4. (Amino)bisphosphinimines

The hexachlorocyclodiphosphazane, $[MeNPCI_3]_2$ reacts with primary aromatic amines to yield the bisphosphinimine hydrochlorides, $[(MeNH)(ArNH)_2P(NMe)P(NAr)-(NHAr)_2]^+Cl^-$ ($Ar = C_6H_5$, 9; C_6H_4Me -4, 10; $C_6H_4(OMe)$ -4, 11). The crystal structure of the *p*-toluidino derivative 10 has been determined; the molecule displays very short P-N bonds (av. 1.633 Å). Dehydrohalogenation of these products by methanolic KOH yields the free bisphosphinimines. The high basicity of (amino)phosphinimines has been verified by an *ab-initio* calculation of the proton affinity of the model compound, $(NH_2)_3P = NH$. The results indicate that (amino)phosphinimines are stronger bases compared to organic super bases such as guanidine.

2.5. Molecular structures of transition metal complexes of acyclic diphosphazanes

The crystal structures of two transition metal complexes formed by acyclic diphosphazanes, viz., $[\text{Mo}(\text{CO})_4(\text{Ph}_2\text{PN})(\text{Pr}^i)\text{PPh}_2(\text{O})]$ (12) and $[\text{PdCl}(\text{PhN}(\text{P}(\text{OPh})_2)_2)]_2$ (13) have been determined. In the molybdenum complex, a rare heterofunctional, P, O-coordination is observed. The dipalladium complex shows the shortest Pd(I)–Pd(I) distance (2.620(1) Å) among this type of dinuclear palladium complexes⁸.

3. Conclusion

Structural studies on different kinds of phosphorus–nitrogen compounds throw light on the nature of P–N bond. The P–N multiple bonding can be explained mainly on the basis of negative hyperconjugative interactions between the nitrogen lone pair and a P–X σ^* orbital. These interactions are cumulative in some instances leading to very short P–N bonds. The P–N–P angles vary over a wide range and in spite of these large variations, the nitrogen atom attached to a phosphorus atom invariably assumes planar geometry. The pyramidal geometry around the nitrogen atom observed in a few instances is probably a result of the inability of the nitrogen lone pair to take part in 'negative hyperconjugation'.

4. Experimental

The aryloxy and trifluoroethoxy λ^3 -cyclotriposphazanes were synthesized by treating the chlorocyclotriposphazane⁴ $[\text{EtNPCl}_3]$ with phenols in the presence of diazabicyclooctane (DABCO) or with sodium trifluoroethoxide in benzene in solution and purified by passing the product through a silica gel column. The λ^5 -trioxocyclotriposphazanes were prepared by treating the corresponding λ^3 -cyclotriposphazanes with Me_3NO in CH_2Cl_2 or with 20% aq. H_2O_2 in THF. The reactions of Group 6 metal carbonyl precursors with λ^3 -cyclotriposphazanes were carried out under dry nitrogen atmosphere in *n*-hexane. The bicyclic tetroxotetraphosphapentazane was prepared by treating $[\text{Cl}_2\text{P}_4(\text{NEt})_5]$ with 2,6-dimethylphenol and DABCO in benzene followed by oxidation of the product by H_2O_2 in THF. Bisphosphinimine hydrochlorides were prepared from $[\text{MeNPCl}_3]_2$ and primary aromatic amines in boiling benzene and dehydrohalogenated to neutral bases by treating them with methanolic KOH.

References

1. HEAL, H. G. *The inorganic heterocyclic chemistry of sulfur, nitrogen and phosphorus*, 1980, Academic Press.
2. BALAKRISHNA, M. S., *et al.*, *Coord. Chem. Rev.*, 1994, **129**, 1–90.
3. KEAT, R. *Top. Curr. Chem.*, 1982, **102**, 89–116.
4. GEMMIL, J. AND KEAT, R. *Inorg. Synth.*, 1988, **25**, 13–15.
5. KORKIN, A. A. *Russ. Chem. Rev.*, 1992, **61**, 473–483.
6. BIDDLESTONE, M., KEAT R., PARKES, H. G., ROSE, H., RYCROFT, D. S. AND SHAW, R. A. *Phosphorus, Sulfur*, 1985, **25**, 25–31.
7. LEHN, J. M. AND WIPFF, G. *J. Chem. Soc. Chem. Commun.*, 1975, 800–802.
8. BALAKRISHNA, M. S., *et al.* *J. Chem. Soc. Dalton Trans.*, 1993, 477–482.

Thesis Abstract (Ph.D.)

Numerical studies of laminar compressible boundary layer flows with heat and mass transfer by Satyajit Roy

Research supervisor: G. Nath

Department: Mathematics

1. Introduction

The boundary layer theory was first developed for the case of laminar incompressible fluids but, later, it was extended to include compressible flows also. The first contribution in this direction came from Busemann¹ in 1931. The development of the theory of boundary layer flow in a compressible stream was stimulated by the progress in aeronautical engineering and, in recent times, by the development of rockets and artificial satellites. In this case of compressible flow, the work of compression and energy dissipation produces considerable increase in temperature as the flight velocities are attained to the value of the order of multiples of velocity of sound. Thus, thermal effects play an essential part and adjacent to a body moving in compressible fluid there is not only a velocity boundary layer, but there is also a thermal boundary layer, across which the temperature undergoes a rapid variation, in a manner analogous to the velocity boundary layer. Since the flow phenomena and thermal phenomena interact to a high degree, the momentum and energy equations are coupled and need to be solved simultaneously.

2. Present analysis

The present work involves a numerical study of some steady and unsteady laminar compressible boundary layer flows with heat and mass transfer. The unsteadiness is assumed to be due to the free stream velocity varying arbitrarily with time. The first problem deals with an unsteady laminar compressible boundary layer flow of an electrically conducting fluid at the stagnation point of an axisymmetric blunt-nosed body with vectored mass transfer (both tangential and normal velocity components at the wall are non-zero) and an applied magnetic field². In the second problem, the simultaneous effects of large injection and transverse curvature in an unsteady laminar boundary layer flow of a compressible fluid with variable properties over a slender axisymmetric body have been investigated³. Later, in a different study, the effect of massive blowing on an unsteady laminar swirling compressible boundary layer flow of an axisymmetric body of arbitrary cross-section has also been investigated⁴. The type of swirl considered here is that of a free-vortex superimposed on the longitudinal flow of a compressible fluid with variable properties. The analysis is applicable to external flow over a body as well as internal flow along a surface. In all the above three problems, semi-similar solutions have been obtained for accelerating/decelerating free stream and fluctuating free stream. The last problem deals with non-similar solution for the steady compressible boundary layer flow over two-dimensional (cylinder) and axisymmetric body (sphere)⁵. The effects of non-uniform slot injection (mass transfer occurs in small porous section of the body surface and the remaining part of the body surface is solid) and non-uniform total enthalpy at the wall (wall cooling or heating takes place in the slot and the rest of the body surface has a constant value of the total enthalpy) have been studied in detail.

For each problem, the nonlinear partial differential equations governing the flow have been solved by using an implicit finite difference scheme in combination with the quasilinearization method⁶ except for the massive blowing cases in which quasilinear implicit finite difference scheme with variable step size has been used for the numerical stability⁷.

3. Results and discussion

The effect of various parameters on skin friction and heat transfer have been considered for the above problems. From the results of the first problem, it is observed that the vectored injection is more effective in reducing skin friction compared to the injection applied normal to the surface but the heat transfer is less affected by vectored injection. Results also show that the heat-transfer rate can be reduced by applying magnetic field. In the case of large injection problem, the skin friction and heat transfer can be reduced remarkably by injecting a large amount of fluid (coolant) into the boundary layer whereas the transverse curvature, swirl and longitudinal pressure gradient parameters increase both the skin friction and heat transfer. The location of the dividing stream line is displaced from the boundary by the blowing rate but the transverse curvature and swirl parameters tend to bring it nearer the boundary. The effect of the variation of the density-viscosity product across the boundary layer is becoming less with the increase of mass injection into the boundary layer. Results of the last problem show that the non-uniform slot injection moves the point of separation downstream but the non-uniform slot suction has the reverse effect. The increase of Mach-number shifts the point of separation upstream due to the adverse pressure gradient. The increase of total enthalpy at the wall causes the separation to occur earlier while cooling delays it.

References

1. BUSEMANN, A. *Handbuch der experimental physik*, 1931, p. 341.
2. ROY, S. AND NATH, G. Unsteady laminar compressible boundary layers with vectored mass transfer and an applied magnetic field, *Int. J. Engng Sci.*, 1992, 30, 15-24.
3. ROY, S. AND NATH, G. Unsteady hypersonic boundary layers for slender axisymmetric bodies with large injection rates, *Int. J. Engng Sci.*, 1992, 30, 793-803.
4. ROY, S. AND NATH, G. Unsteady laminar compressible swirling flow with massive blowing, *AIAA J.*, 1992, 30, 2604-2605.
5. ROY, S. AND NATH, G. Non-uniform slot injection (suction) or wall enthalpy into a steady nonsimilar compressible laminar boundary layer, *Acta Mech.*, 1994, 103, 45-61.
6. INOUE, K. AND TATE, A. Finite-difference version of quasilinearization applied to boundary-layer equations, *AIAA J.*, 1974, 12, 558-560.
7. LIU, T. M. AND CHIU, H. H. Fast and stable numerical method for boundary layer flow with massive blowing, *AIAA J.*, 1976, 14, 114-116.

Thesis Abstract (Ph.D.)

Light scattering investigations of reentrant phase transitions of liquid mixtures

by B. V. Prafulla

Research supervisors: A. Kumar and A.K. Sood

Department: Physics

1. Introduction

The reentrant phase transitions (RPT) imply that a system reenters a state, macroscopically identical to the initial one, when a suitable thermodynamic field variable is altered monotonically¹. Among the diverse systems exhibiting RPT, the quasibinary mixtures are a prime example¹⁻⁵. In these liquid mixtures, reentrance is manifested by a closed loop miscibility curve with upper and lower consolute points (T_U and T_L), respectively. The two-phase region in these systems is represented by the loop size ($\Delta T = T_U - T_L$) and the double critical point (DCP) is signified by the limit $\Delta T = 0$.

The 3-D Ising like critical behaviour near a T_U or T_L , when ΔT is sufficiently large, is well understood⁶. Thus, it is interesting to examine the nature of DCP as it is formed by the coalescence of T_U and T_L . The intermediate phases in an RPT can be suppressed by employing a thermodynamic field variable such as pressure, electric field, magnetic field, third component. . . , etc. In a liquid mixture exhibiting RPT, ΔT can be controlled with the aid of a suitable third component^{1-5, 7}.

The theoretical models^{8,9} concerning RPT predict a doubling of critical exponents (CEs) in the close vicinity of a DCP. The intent of earlier endeavours was to explore the *gross* features of the evolution of the critical behaviour in the limit $\Delta T \rightarrow 0$. Broadly, it was shown that CEs [ν , γ , ϕ , θ and β] increased sharply as ΔT was reduced and as T_L (or T_U) was neared. However, *exact* doubling of CEs was not noticed due to the fact the DCP was not probed close enough.

The present investigation is aimed at (i) confirming the crucial assumption of the geometrical picture of phase transitions, namely, the parabolic nature of the line of critical points (joining T_{Us} and T_{Ls}), especially in the close

vicinity of the DCP, (ii) observing an *exact* doubling of CEs, by approaching the DCP closer than it had been done so far, (iii) discerning the phenomenon underlying the approach to double criticality, (iv) recovering the universal CEs for any ΔT , by employing an alternate field variable that represents the true experimental path, (v) gaining insight into the ionic critical behaviour in liquid mixtures where an electrolyte induces the re-entrant miscibility, and (vi) to study the response of the correlation-to-scaling exponent (Δ) near DCP.

The quasibinary systems studied are: 3-methylpyridine (MP) + water (W) + Heavy water (HW) and MP + W + NaCl. The thermophysical property studied is the osmotic compressibility (χ) and it is extracted from the scattered laser light.

2. Experimental

The quasibinary mixtures were made using MP (99%, Aldrich), HW (isotopic purity 99.6%, BARC, India), freshly prepared W in an all-quartz triple distiller and analytical grade NaCl (Ranbaxy, India). The chemicals were transferred to light-scattering cells with air tight syringes fitted with millipore filters.

To attain temperature stability with good precision, a thermostat with good thermal isolation from its surroundings and sensitive temperature controller (PID) were fabricated. The temperature stability experienced by the sample is ± 3 mK in the range (35–90°C) of over 6–8 h. A light scattering setup which enables the measurement of scattered light (at 90°) and the transmitted light was designed. A typical run scanned the temperature range $1.5^\circ\text{C} \lesssim (T_L - T) \lesssim 25^\circ\text{C}$. The duration of each run was 35–45 h and it yielded 40–50 data points. All the data were collected in one phase region as T_L was approached.

The major experimental difficulties^{1,10} encountered are the temporal instability in ΔT and obtaining the proper critical composition x_c for each sample. In addition to the problem of stability, there is an intrinsic difficulty in the preparation of samples of small ΔT s due to the parabolic¹⁰ nature of the line of critical points. The quadratic shape of the line of critical points and its continuity was confirmed by probing DCP very closely¹⁰ ($\Delta T = 0.239^\circ\text{C}$).

3. Results

The scattered intensity (I_s), after correcting for turbidity, is given by^{1,11}

$$\frac{I_s}{T} = \frac{At^{-\gamma}}{(1 + q^2\xi^2)^{1-\eta/2}} \quad (1)$$

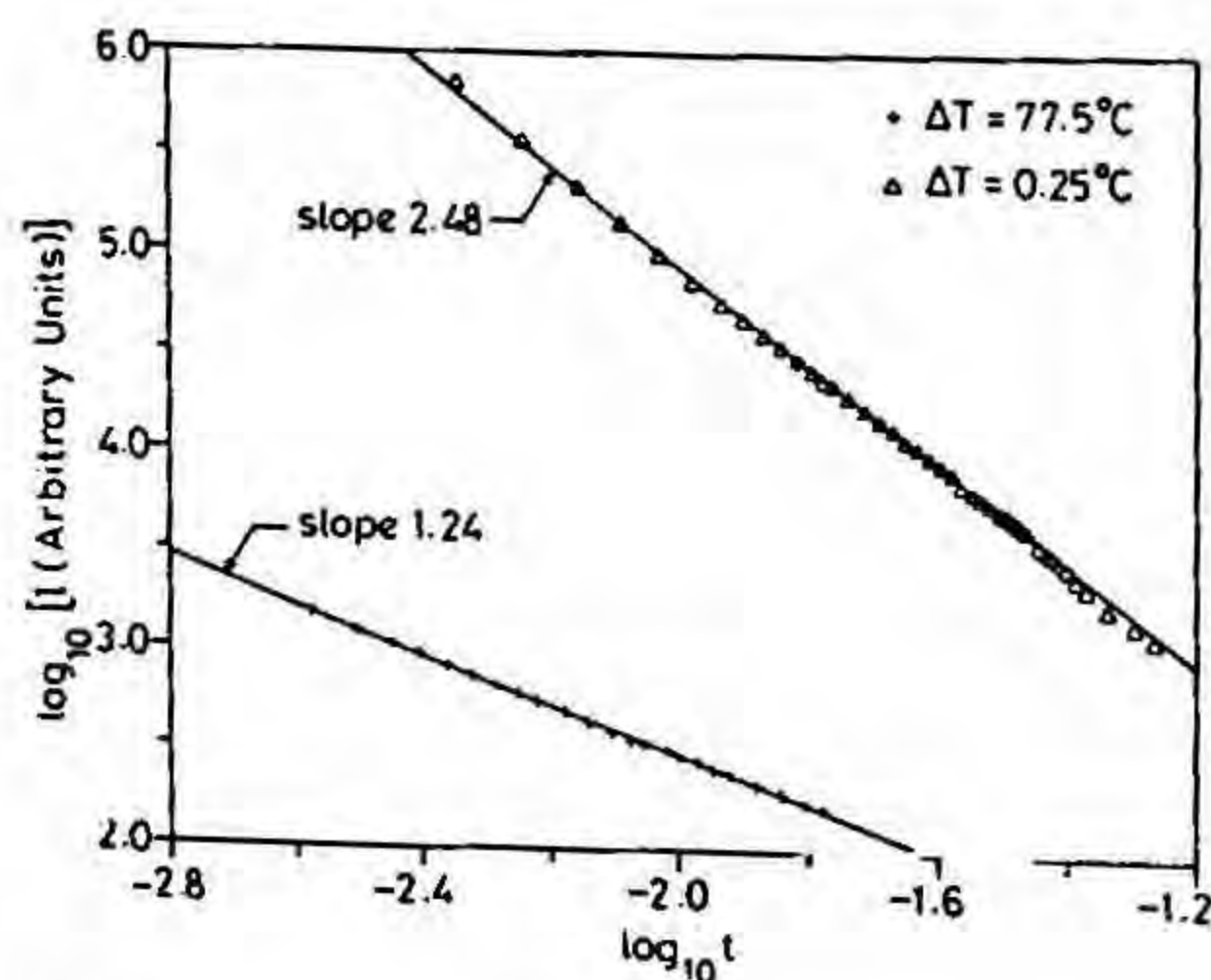


Fig. 1. The normalized scattered intensity (I) vs reduced temperature (t) for the two extreme cases ($\Delta T = 77.5$ and 0.25°C).

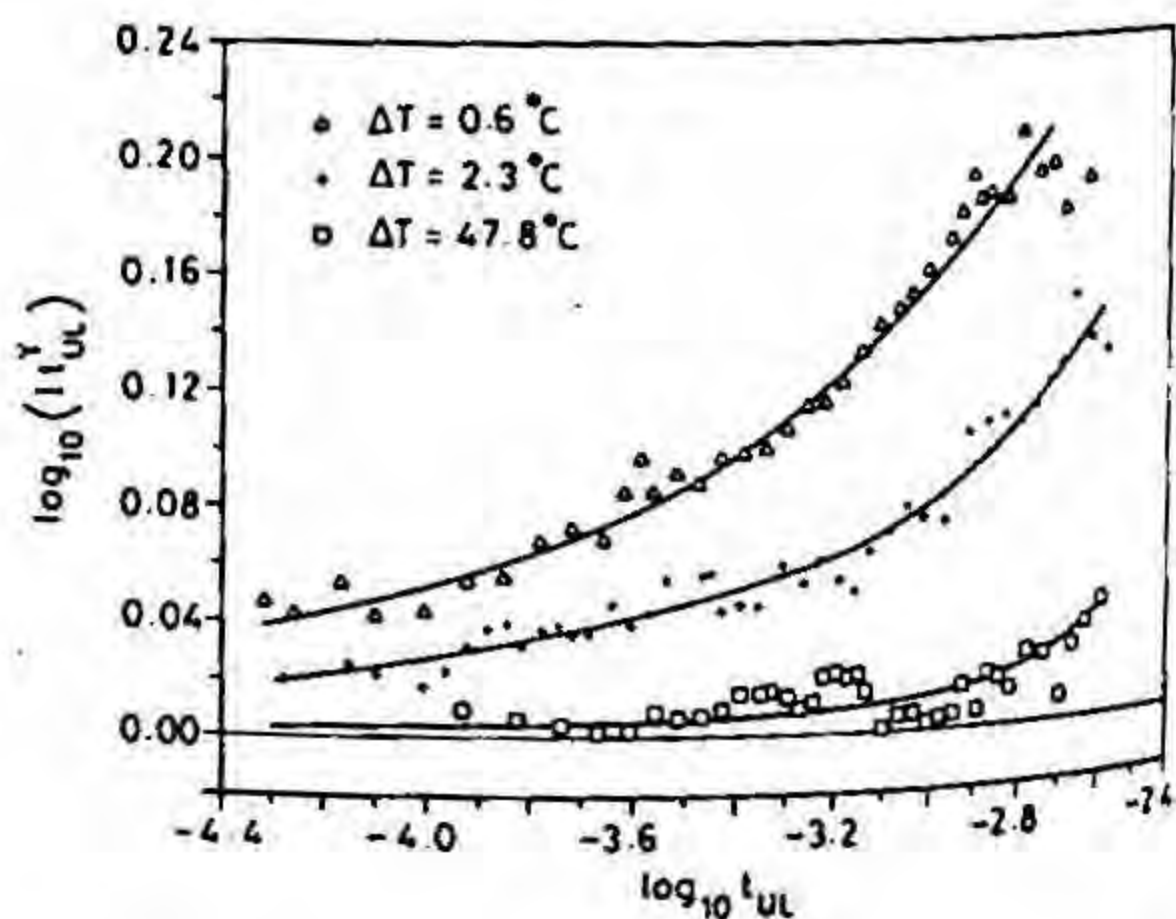


Fig. 2. Pictorial representation of the recovery of the universal CE $\gamma (= 1.24)$ for any ΔT . The line for (MP + W + HW) has been shifted for the sake of clarity.

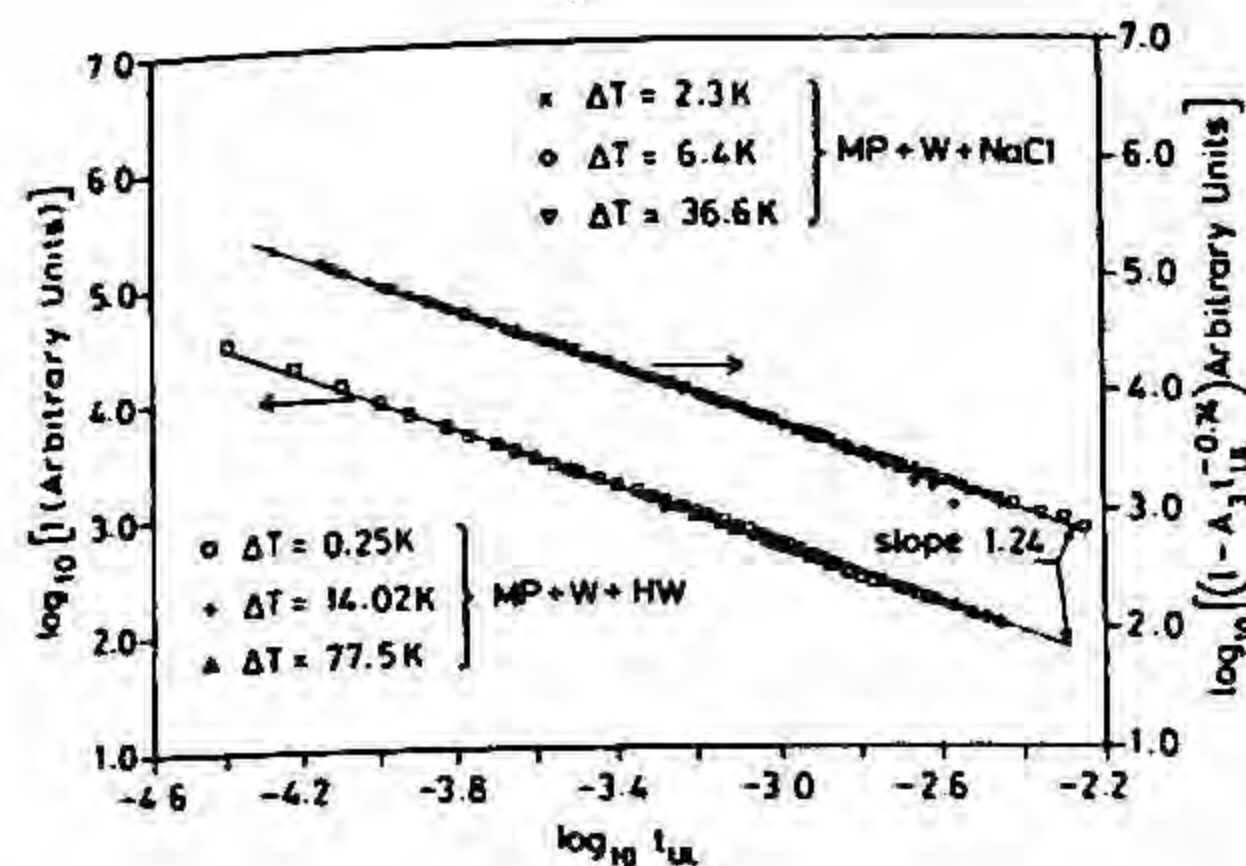


Fig. 3. Log-log plot of normalized intensity (in arbitrary units) multiplied by t_{UL} (to neutralize the temperature dependence of I_s) vs t_{UL} . The increasing importance of the extended scaling term (Δ), as $\Delta T \rightarrow 0$, is emphasized by the marked departure of the curves from the horizontal axis. The continuous curve is a guide to the eye.

where A is the critical amplitude, γ , the CE that describes the divergence in χ , $\xi (= \xi_0 t^{-\nu})$ is the correlation length. The renormalization group estimates of CEs γ , ν and η are 1.241, 0.63 and 0.03, respectively. The scattering wave vector q is given by $(4\pi n/\lambda)\sin(\theta/2)$, where n is the refractive index of the mixture and λ , the wavelength of incident light in vacuum. A nonlinear least squares fit program (CURFIT)¹² was used to fit the data. Analyzing the data of (MP + W + HW) with the usual field variable $t (= |(T_c - T)/T_c|)$, T_c being T_L , yielded an *exact doubling*¹ of the 3-D Ising value for $\Delta T = 250$ mK, as elucidated in Fig. 1. The approach to double criticality is featured by a smooth *crossover* of the CE (γ) from the doubled to its single limit for intermediate ΔT s as $t \rightarrow 0$. This crossover aspect¹ coupled with some infirmities of the fit to eqn (1) led us to adopt a new field variable $t_{UL} (= |(T_U - T)(T_L - T)/T_U T_L|)$, which takes into account the *simultaneous* approach to T_U (or T_L) as T_L (or T_U) is neared. Figure 2 illustrates the most significant finding—the recovery of the universal¹ CE ($\gamma = 1.24$) as ΔT varies by more than a factor of 300 (from 0.250 to 77.5°C). The increase of an effective CE as DCP is approached as a function of t is implied by t_{UL} .

The non-phase-separating sample of (MP + W + HW) was examined as it was heated towards the DCP temperature (T_D). The data were analyzed with the thermodynamic field $t_D (= |(T_D - T)/T_D|)$. The access to DCP is marked by the doubled CE (2γ) (for large t_D) merging into a saturating divergence¹³ (as $t_D \rightarrow 0$).

The data of (MP + W + NaCl) were analyzed using eqn (1) with t_{UL} as the field variable. Fit to a pure power law yielded progressively smaller γ s as $\Delta T \rightarrow 0$, which is a typical index of the existence of correction-to-scaling terms⁷. This infirmity coupled with the progressive departure of the data from simple power law, as depicted in Fig. 2, guided us to incorporate the extended scaling term (Δ),

$$\frac{I_s}{T} = \frac{A_1 t_{UL}^{-\gamma}}{(1 + q^2 \xi^2)^{1-\eta/2}} (1 + A_2 t_{UL}^{\Delta}). \quad (2)$$

The simultaneous doubling of *both* the leading and the extended scaling exponents^{7,13} (γ and Δ) at DCP ($t_{UL} = t_D^2$) is illustrated in Fig. 3.

4. Discussion

Most of the results of our research can be rationalized on the basis of the phenomenological theories^{3-5,13} and model calculations^{8,9}. However, a rigorous theoretical attempt to unravel the behaviour of the extended scaling CE (Δ) is called for.

References

1. PRAPULLA, B. V., NARAYANAN, T. *Phys. Rev. A*, 1992, 45, 1266–1269. AND KUMAR, A.

2. NARAYANAN, T., KUMAR, A. AND GOPAL, E. S. R. *Phys. Lett. A*, 1990, 144, 371-375.
3. JOHNSTON, R. G., CLARK, N. A. WILTZIUS, P. AND CANNELL, D. S. *Phys. Rev. Lett.*, 1985, 54, 49-52.
4. SORENSEN, C. M. AND LARSEN, G. A. *J. Chem. Phys.*, 1985, 83, 1835-1842.
5. DAVIDOVICH, L. A. AND SHINDER, I. I. *Sov. Phys. JETP Lett.*, 1989, 68, 742-750.
6. KUMAR, A., KRISHNAMURTHY, H. R. AND GOPAL, E. S. R. *Phys. Rep.*, 1983, 98, 57-143.
7. PRAFULLA, B. V., NARAYANAN, T. AND KUMAR, A. *Phys. Lett. A*, 1992, 164, 443-446.
8. GOLDSTEIN, R. E. AND WALKER, J. S. *J. Chem. Phys.*, 1983, 78, 1492-1512.
9. WHEELER, J. C. AND ANDERSEN, G. R. *J. Chem. Phys.*, 1980, 73, 5778.
10. NARAYANAN, T., PRAFULLA, B. V., KUMAR, A. AND GOPAL, E. S. R. *Ber Busenges. Phys. Chem.*, 1991, 95, 12-14.
11. GOLDBURG, W. I. *Light scattering near phase transitions* (Cummins, H. Z. and Levanyuk, A. P., eds) pp. 531-581, 1983, North-Holland.
12. BEVINGTON, P. R. *Data reduction and error analysis for physical sciences*, 1969, McGraw-Hill.
13. PRAFULLA, B. V., NARAYANAN, T. AND KUMAR, A. *Phys. Rev. A*, 1992, 46, 7456-7465.

Thesis Abstract (M. Sc. (Engng))

A study on generation and characterization of transverse and longitudinal cracks in thick weldments by C. Mani

Research supervisors: Kishore, C. R. L. Murthy and V. P. Raghupathy

Department: Metallurgy

1. Introduction

Defects, in particular cracks in welded constructions, degrade the structure and in some cases lead to catastrophic failures. Thus, the detection and characterization of cracks in welds are of great importance. As the evaluation has to be performed nondestructively conventionally suitable nondestructive testing (NDT) methods are utilised. Hence, a complete qualitative and quantitative assessment of these defects is an areas of considerable significance. Most of the conventional NDT techniques rely upon results on a comparative basis¹, rather than on an absolute measurement; for example, standard reference blocks used in ultrasonics contain artificially drilled holes/notches. While these can be used to provide an approximate assessment, quantification and characterization need specimens with natural defects depicting the geometry, morphology and microstructural features as encountered in real-life situations. A survey of the published literature and available standards though indicates certain methodologies

for homogeneous materials and thin sections, the same are not available for thick weldments. This will be an area of considerable interest and immediate relevance to the welding industry.

2. Experimental details

The experiments were conducted on carbon-manganese steel (SA: 299/ASTM Standard) used in boiler fabrication. Cracks of specific features were introduced in weldments of thicknesses ranging from 16–225 mm using manual metal arc and submerged arc welding processes. Cracks were generated in a controlled way using the special hardfacing electrode developed by the Welding Research Institute. The microstructure of the weldment was changed by hardfacing electrode deposition. Microstructural features will be one of the important factors that will ultimately affect the mechanical properties of the weldment.

The defects introduced were detected and characterized using volumetric NDT methods like radiography and ultrasonic testing. Special NDT techniques like high-energy radiography using linear accelerator and immersion ultrasonic testing were also performed to characterize the defect².

Further each millimeter thickness of the specimen in which the defects were introduced was sectioned by machining and the crack morphology was traced for comparing with the NDE results obtained.

A computer model was developed in FORTRAN-IV for imaging the crack in the weldment at different sections which helps in visualizing morphological changes from section to section through the thickness.

3. Results and conclusions

Weld defects like longitudinal and transverse cracks could be generated in reproducible manner by manual metal arc and submerged arc welding processes employing a special technique and controlling the welding parameters. Close tolerance in the length of the cracks could be obtained. The reason for the weldmetal cracking are faster cooling and brittle metallurgical structure from special hardfacing electrode. Conventional NDE methods are generally reliable for locating and positioning the cracks, but the crack dimension in through thickness direction is not precise³, whereas the defect characterization technique using advanced NDE is better and resolution in the depth direction is accurate.

Efforts were made to reconstruct the defect by computer graphics and from the results obtained it is observed that this approach is very promising. The NDT techniques are limited in characterization of defects in higher thickness welds and the use of more than one technique to complement the results is recommended⁴. The study reveals that with increase in heat input the weldmetal toughness decreases.

References

1. *Welding handbook* Vol. II; 7th edn, pp. 22.1–22.26 and 24.1–24.66, American Welding Society.
2. KRAUTKRAMER, J. AND KRAUTKRAMER, H. *Ultrasonic testing of materials*, 3rd edn, pp. 144–149, Springer-Verlag.
3. COFFEY, J. M. AND DATES, G. *Problems in interpreting ultrasonic echoes from weld defects*, IIW document No. XIII-1260A-87 of Commission-V, pp. 3–8.
4. The significance of defects in welds; *Proc. 2nd Conf.*, Welding Institute, UK, Vol. I, pp. 140–150, 1968.

Thesis Abstract (Ph. D.)

Studies in stereoelectronic effects at oxygen by C. D. Roy

Research supervisor: Sosale Chandrasekhar

Department: Organic Chemistry

1. Introduction

Stereoelectronic effects are of much current interest in organic and bio-organic chemistry^{1,2}. Although various types of stereoelectronic effect have been proposed since even the early days of organic chemistry, modern versions rely largely on conformational concepts. With stereochemistry being centre-stage in modern organic chemistry, whether synthetic or mechanistic, it is hardly surprising that stereoelectronic effects have been recognised to be of fundamental importance.

In this work, stereoelectronic effects at oxygen have been studied in various systems, the results obtained being of both mechanistic and synthetic interest. A necessarily brief historical survey of the conceptual development of stereoelectronic effects is to be found in the opening chapter.

2. Results and discussion

In the Baeyer–Villiger reaction, the breakdown of the Criegee intermediates is expected to be under stereoelectronic control. However, the problem is that Criegee intermediates are generally not isolable, so that direct mechanistic studies are not possible. The strategy adopted in this work is a novel one, and makes use of a hitherto unknown intramolecular Baeyer–Villiger reaction to generate a Criegee intermediate of predictable and fixed geometry, the products of its fragmentation depending on whether stereoelectronic control is obtained or not.

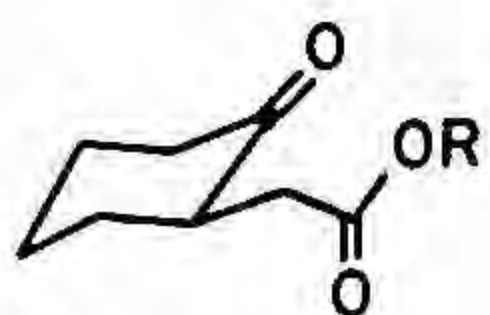
Application³ of this strategy to (2-oxocyclohexane)acetic acid (1a) resulted in the formation of succinic acid (3), rather than the octanedioic acid (4). This is best explained by the intermediacy of (2) and its stereoelectronically controlled fragmentation. The usual migratory-aptitude control is absent, secondary carbon migrating in preference to tertiary. With 2-butyl (2-oxocyclohexane)acetate (1b), however, products of both secondary carbon and tertiary carbon migration were observed: in this case, the intramolecular route appears to be impossible, so that formation of the latter product—*via* an intermolecular pathway and involving migratory aptitude control—is to be expected; however, the secondary carbon migration is surprising, and is probably due to intramolecular assistance of O–O cleavage by the ester carbonyl oxygen—*i.e.*, a cyclic transition state rather similar to that in the reaction of the ketoacid.

Application of these strategies to (2-oxocyclopentane)acetic acid and its 2-butyl ester resulted, in both the cases, in the formation of products of both secondary and tertiary carbon migration. This is explained as being due to additional strain—because of the smaller, five-membered, ring—in the cyclic transition state for secondary carbon migration, with the result that the intermolecular pathway becomes competitive with the intramolecular one.

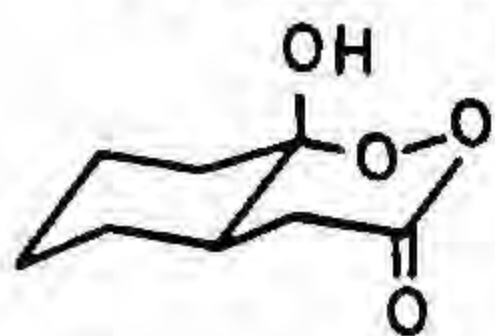
Studies were carried out to determine the origin of the unusual stability of the tricyclic orthoformate, 2,4,10-trioxatricyclo[3.3.1.1^{3,7}]decane (5a). A solvent isotope effect study of its hydrolysis showed that $k(\text{D}_2\text{O})/k(\text{H}_2\text{O}) = 0.76$, thus indicating that hydration of the intermediate dioxocarbenium ion, rather than C–O cleavage, is slow and rate determining. This is probably due to the close proximity of the hydroxyl group to the cationic centre in the intermediate ion. The origin of the above stability thus appears to be kinetic.

The unusual tricyclic orthocarbonate, 3-methoxy-2,4,10-trioxatricyclo[3.3.1.1^{3,7}]decane (5b), in which the exocyclic C–O bond lacks anomeric stabilization, was synthesized. Attempts to prepare 3-bromo-2,4,10-trioxatricyclo[3.3.1.1^{3,7}]decane (5c), expected to be a novel bromo orthoformate, were unsuccessful.

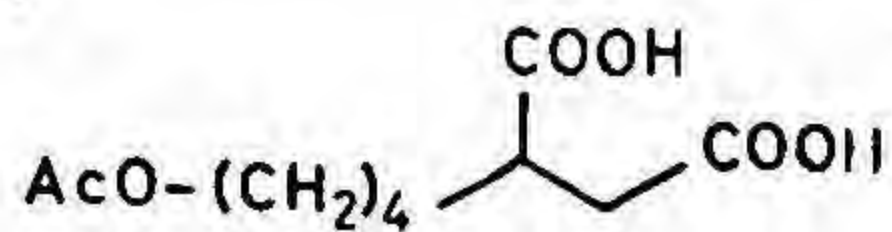
Studies were designed to take advantage of the above mechanistic lessons, *i.e.*, the stability of the 2,4,10-trioxatricyclo[3.3.1.1^{3,7}]decane system towards ring opening. It was thus expected that 2,4,10-trioxatricyclo[3.3.1.1^{3,7}]decyl-methylithium (5d) would be stable to ring opening. This was indeed found to be true, the methylithium being prepared by bromine–lithium exchange, and found to add to non-enolisable aldehydes in excellent yields. The resulting alcohols (6) could be oxidized to the corresponding ketones, which could be converted *via* the reduction of their oximes, and acid hydrolysis of the orthoformate, to β -amino acids and esters. Thus methylithium (5d) functions as a carboxyl-protected acetic acid carbanion, to provide carboxyl-protected β -ketoacids which, in turn, undergo further, unique, transformations, impossible to envisage in β -ketoacids.



(1)



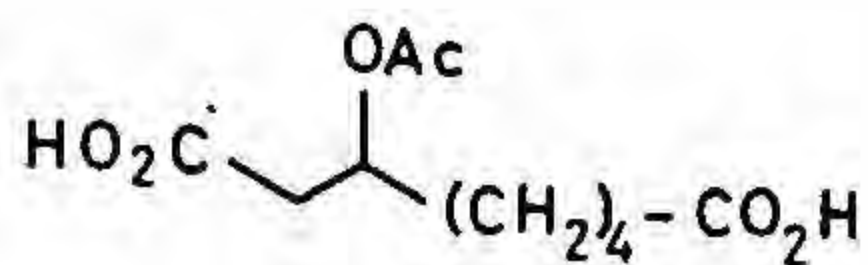
(2)



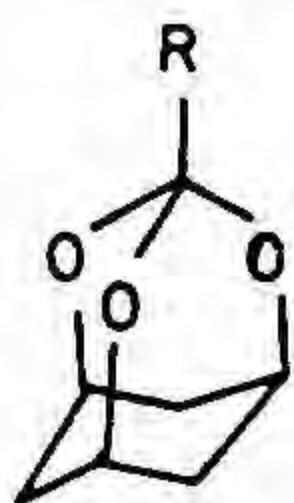
(3)

a : R
H

b : Me-CH(Me)-CH₂-Me



(4)



(5)

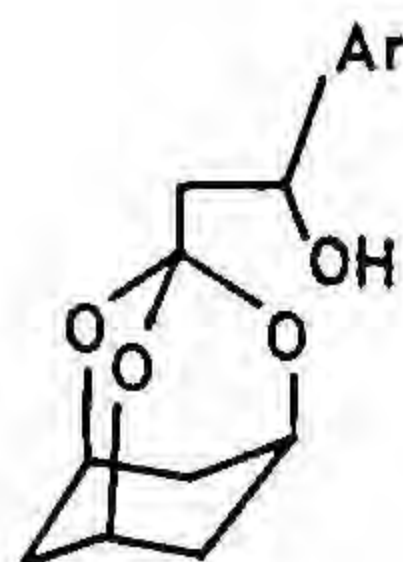
(5)

R

a : H

b : OMe

c : Br

d : CH₂Li

(6)



(a)



(e)

(7)

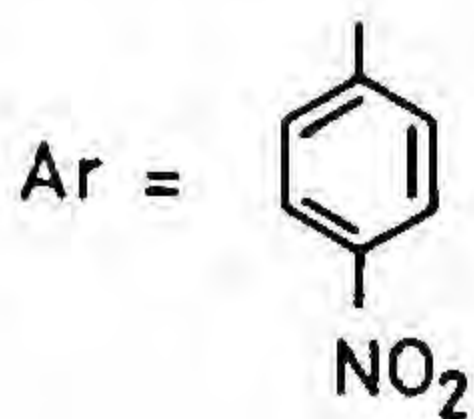


(a)



(e)

(8)



Studies were designed to cast light on the interaction between conformational changes and bond-breaking and bond-making processes in the reactions of conformationally mobile systems, *i.e.*, systems coming under the purview of the Curtin–Hammett principle. The hydrolytic reactivities of the conformationally mobile acetal anomers (7) were compared with those of the corresponding restricted analogues (8) with the help of the Winstein–Holness equation, in the expectation that the mobile equatorial anomer (7e) would be more reactive than the restricted equatorial anomer (8e): this is because (7e) should have direct access to the transition state for the cleavage of (7a) also, by ring inversion concomitant with reaction, such a process being impossible for (8e). However, experiment indicated the contrary result, which is explained as being due to relatively greater ground state entropy in (7e).

References

1. KIRBY, A. J. *The anomeric effect and related stereoelectronic effects at oxygen*, 1963, Springer-Verlag.
2. DESLONGCHAMPS, P. *Stereoelectronic effects in organic chemistry*, 1983, Pergamon.
3. CHANDRASEKHAR, S. AND ROY, C. D. Evidence for a stereoelectronic effect in the Baeyer–Villiger reaction: Introducing the intramolecular reaction, *Tetrahedron Lett.*, 1987, 28, 6371–6372.

Thesis Abstract (Ph. D.)

Radical cyclisation and annulation strategies to chiral bi- and tricyclic bridged systems by P. Hemamalini

Research supervisor: A. Srikrishna

Department: Organic Chemistry

1. Introduction

Free radical additions on to olefins, in particular the intramolecular version (*i.e.*, radical cyclizations) have been increasingly employed for the synthesis of various functional moieties as well as natural products^{1,2}. A combination of inter and intramolecular radical additions in a single sequence is appealing from synthetic standpoint (eqn 1). In particular, an intermolecular addition of a radical on to a radicophile followed by radical cyclization can provide ring systems from acyclic precursors, and the overall sequence results in an annulation. The generation of various bridged chiral synthons from readily available monoterpene, carvone using radical cyclization and annulation reactions is the objective of present investigation.

2. Synthesis of bicyclo [3.2.1] and [2.2.2]octanes

Regiospecific bromoetherification reaction of S-carvone (1) with N-bromosuccinimide (NBS) in the presence of methanol furnished the bromoenone 2 as a 1:1 diastereomeric mixture. Reaction of the bromoenone 2 with ^tBu₃SnH and AIBN (catalytic) in refluxing benzene (0.02M) afforded the bicyclo[3.2.1]octanones 7 and 12 via 5-*exo* trig radical cyclization^{3,4}. The generality of the sequence was established by the formation of various bicyclo[3.2.1]octanones 8–11 and 13–16 via the radical cyclization of the bromoenones 3–6.

The formation of bicyclo[3.2.1]octanes from carvone via 5-*exo* trig radical cyclization is clearly facilitated by the nature of the receptor olefin, an α , β -unsaturated enone. To test this point, cyclizations were attempted with corresponding allylic alcohols. Radical cyclization of the bromoalcohols 17 and 18 at more dilute conditions (0.01M) gave the bicyclo[3.2.1]octanols 19 and 20. PCC oxidation of the bicyclic alcohols gave the corresponding bicyclic ketones 7 and 12.

This methodology has also been extended for the synthesis of bridgehead-substituted bicyclo [3.2.1]octanones utilizing β -methylcarvone (21) as the starting material⁵. The bromoenones, 22–23 obtained from S-6-

methylcarvone (21) underwent radical cyclization to form the corresponding bicyclo[3.2.1]octanones 24–27 with a methyl group at the bridgehead position.

It was anticipated that the presence of a radical stabilizing group, *e.g.*, aryl group, at the β -position of carvone, which also makes the olefin fully substituted, might change the course of the radical cyclization reaction. Because now due to styrenic nature of the olefin, the 6-*exo* trig mode will compete with the 5-*exo* trig mode, leading to the formation of bicyclo[2.2.2]octanes along with bicyclo[3.2.1]octanes.

The requisite R-6-phenylcarvone (28) was obtained from (S)-carvone *via* the 1,3-alkylative enone transposition methodology⁶, *i.e.*, 1,2 addition of phenyl magnesium bromide followed by the oxidation of the resulting tertiary alcohol 29. Regiospecific bromoetherification of R-6-phenylcarvone (28) afforded the bromoenones 30 and 31. Radical cyclization of the bromoenones 30 and 31 resulted in the formation of a 1:1 mixture of bicyclo[3.2.1]octanones 32 and 35 and bicyclo[2.2.2]octanones 33 and 34 and 36 and 37 *via* competitive 5-*exo* trig and 6-*exo* trig radical cyclization reactions.

On the other hand, radical cyclization reaction of the alcohol 36 furnished the bicyclo[3.2.1]octanol 40 as the major product. The epimeric alcohol 39 furnished the epimeric mixture (2.5:1) of bicyclo[2.2.2]octanols 44 as the major product. An explanation based on conformational rigidity due to the intramolecular hydrogen bonding between the hydroxy and methoxy groups was proposed, and proved by the formation of bicyclo[2.2.2]octanes as major cyclized products with the corresponding acetates.

3. Synthesis of bicyclo[3.3.1]nonanes

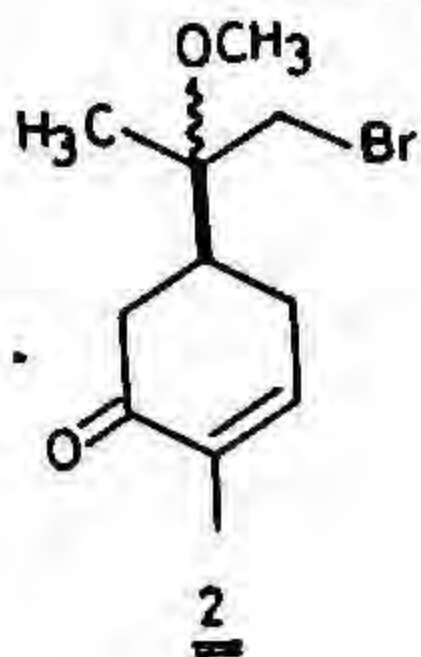
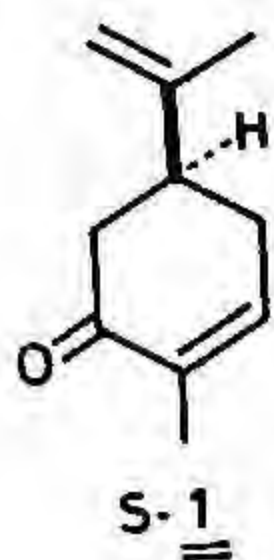
A radical annulation strategy was adopted for the construction of functionalized bicyclo[3.3.1]nonane derivatives starting from carvone. The tertiary halides 45 and 46 were opted as the radical precursors. The regiospecific addition of freshly generated gaseous HBr to the electron-rich double bond of (S)-carvone (1) furnished the known carvone hydrobromide 45. Whereas, reaction of (S)-carvone (1) with an *in-situ*-generated HI (TMSCl–NaI–H₂O) in acetonitrile afforded the iodide 46. A sequential inter and intramolecular Michael addition of the radical generated from the bromide 45, in the presence of an excess of acrylonitrile furnished the bicyclic ketonitriles 53 and 54 in a regiospecific manner⁷. To test the generality of this sequence radical annulations were carried out with various other radicophiles. Thus, radical annulation of the bromide with radicophiles 48–52 furnished the corresponding annulated products 55–59.

Radical annulation of the bromide 60 obtained from methylcarvone 23 with ⁿBu₃SnH (1.1 equiv) and AIBN (catalytic) in the presence of acrylonitrile (5 equiv.) furnished the bicyclic ketones 61 and 62 with a methyl group at the bridgehead position.

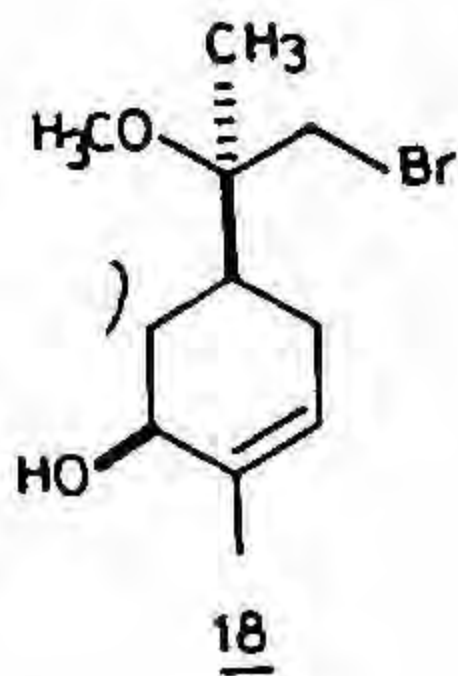
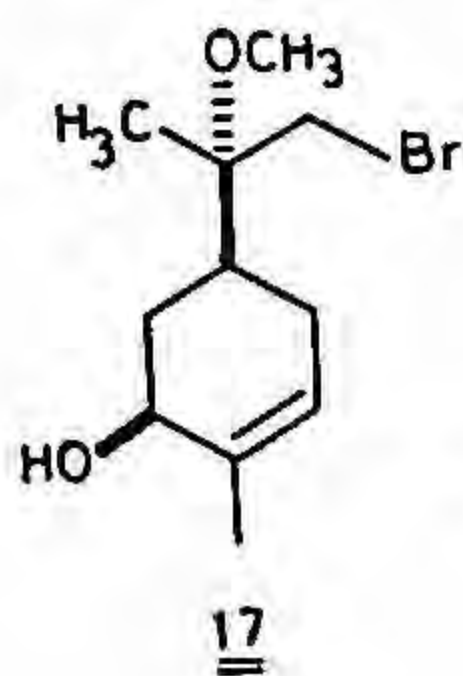
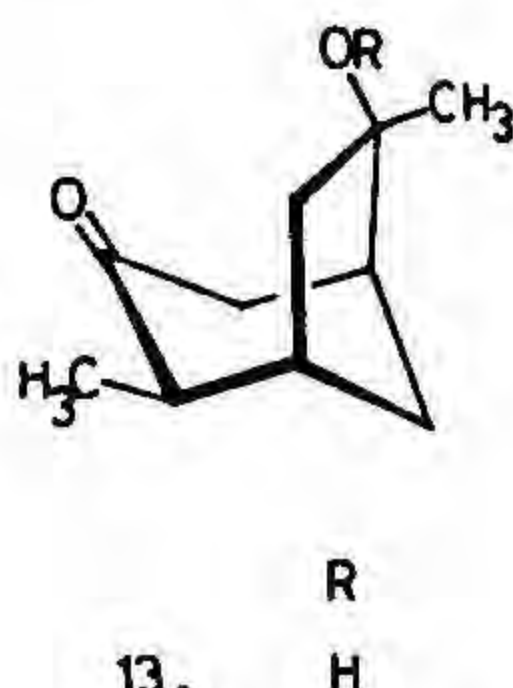
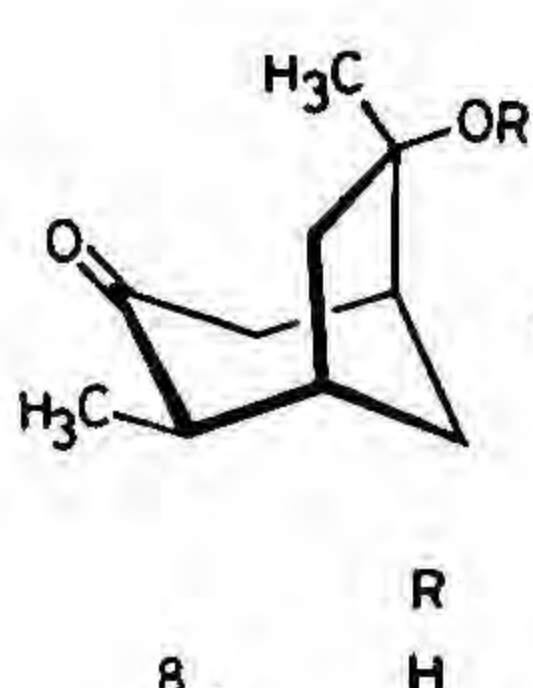
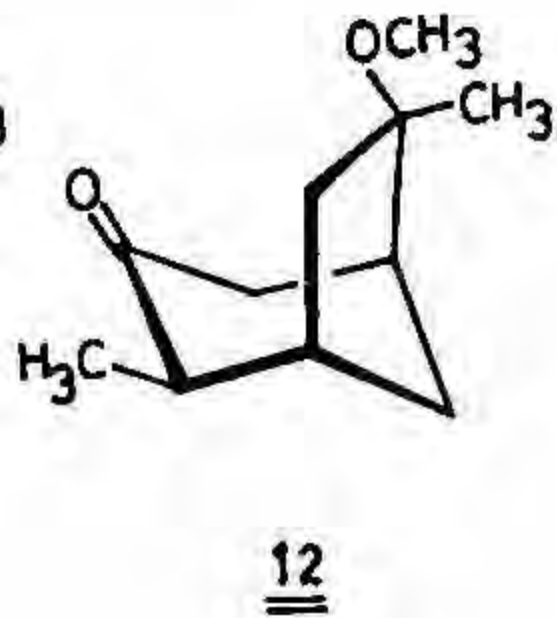
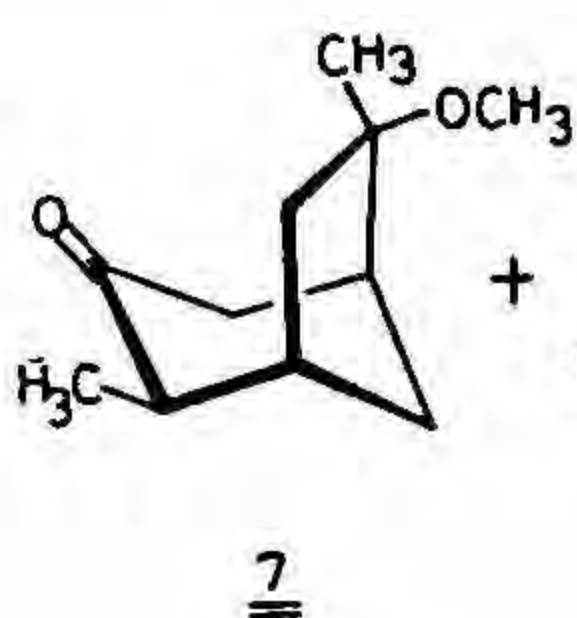
4. Synthetic approaches towards pupukeanone

An intramolecular alkylation reaction using (R)-carvone as the starting material has been employed for the construction of bicyclo [2.2.2] oct-5-en-2-ones, comprising a β,γ -unsaturated enone moiety. Treatment of the allyl bromide 63 with K⁺O⁻Bu in ^tBuOH–THF regiospecifically furnished the bicyclic enone 64. To establish the generality of this sequence, reactions were attempted with the other bromoenones. Thus, intramolecular alkylation of the epimeric mixture of bromoenone 2 furnished the bicyclic enones 65 and 66 in 1:1 ratio⁸. Intramolecular alkylation of the epimeric mixture of bromoenone 30 and 31 furnished the bicyclic enones 67 and 68.

After achieving the construction of chiral bicyclo[2.2.2]octenones from (R)-carvone, attention was focussed on the construction of chiral isotwistanes *via* radical annulation. The treatment of the mixture of 65 and 66 with boron tribromide afforded the bromoenone 69. Radical annulation of the bicyclic bromide 69 afforded a mixture of mono 70 and bis 71 adducts. It was anticipated that the presence of an electron-withdrawing group at C-6 would result in an electrophilic-cyclized radical, and thereby eliminate the possibility of second addition⁹ and hence the sequence was attempted with the phenylated compound. The treatment of the mixture of enones 67 and 68 with boron tribromide generated an inseparable mixture of the bicyclic bromides 72 and 73 in 3:1 ratio. Reaction of the mixture of the (5 equiv.) and AIBN (catalytic) in benzene (0.02M) furnished the cyclopropane 74, without incorporating the radicophile, *via* a 3-*exo* trig radical cyclization on to the styrenic double bond¹⁰.

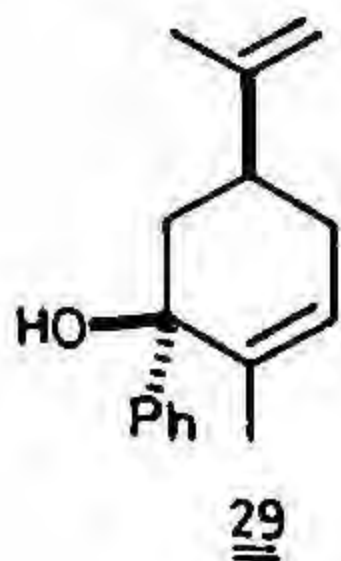
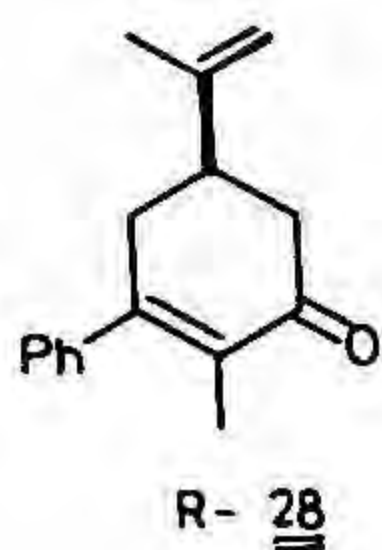
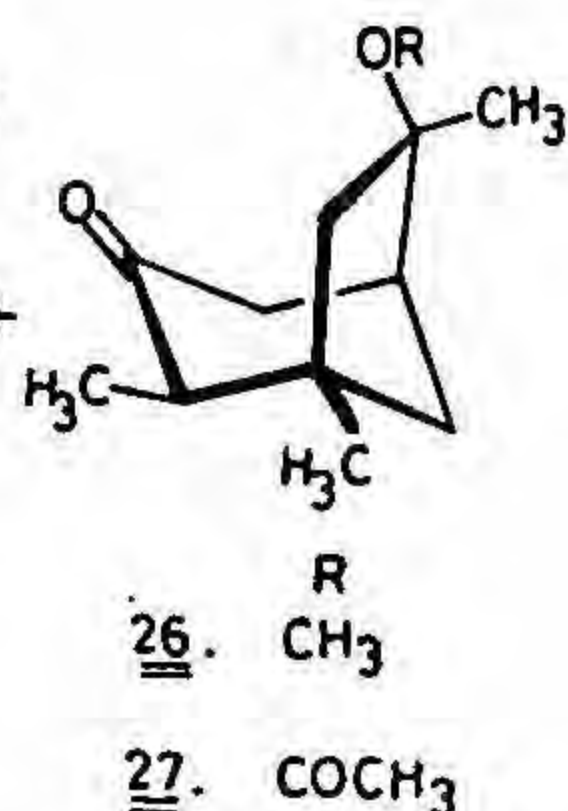
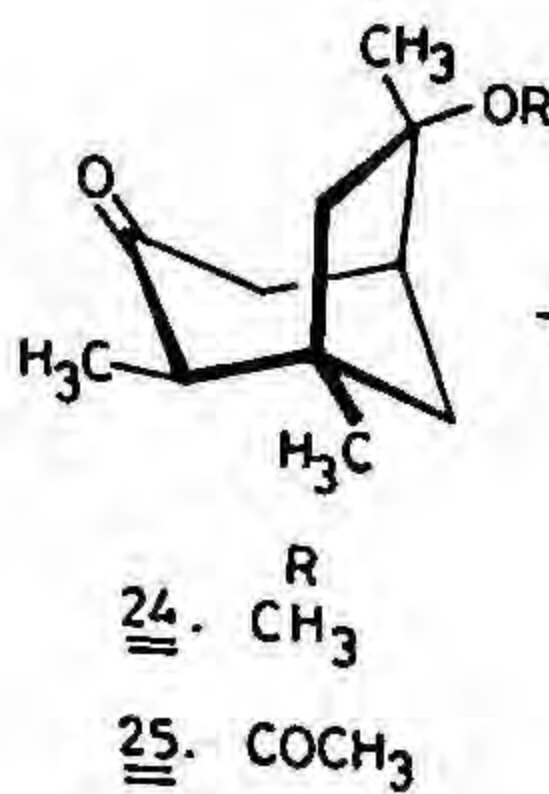
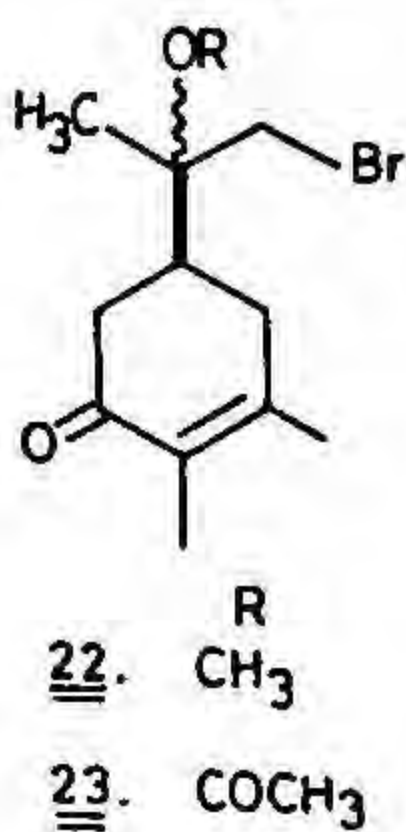
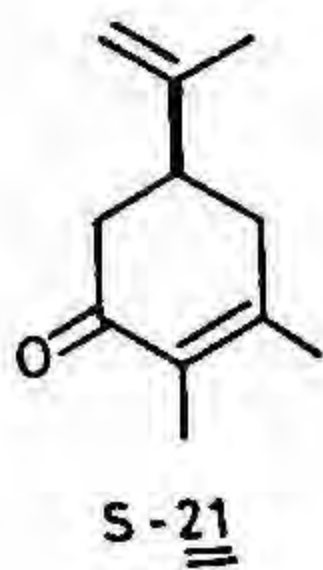
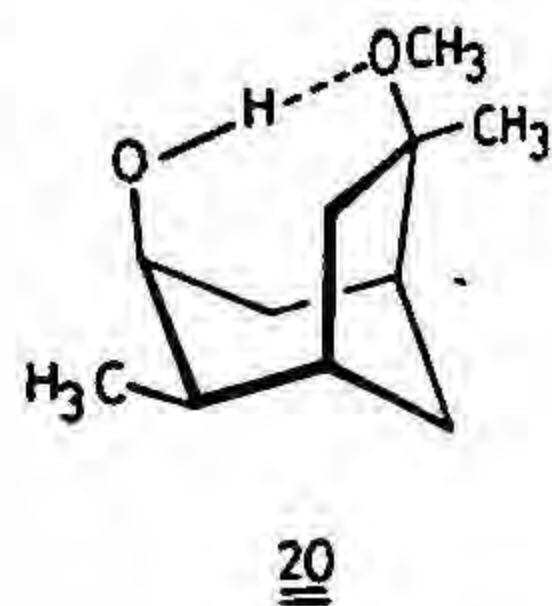
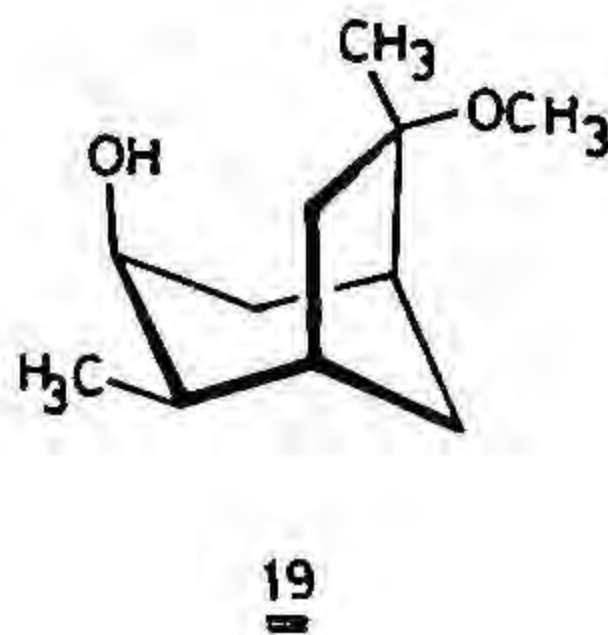


- | | |
|----|---------------------------------|
| 3. | R |
| 4. | H |
| 5. | CH ₂ CH ₃ |
| 6. | CH ₂ Ph |
| 6. | COCH ₃ |



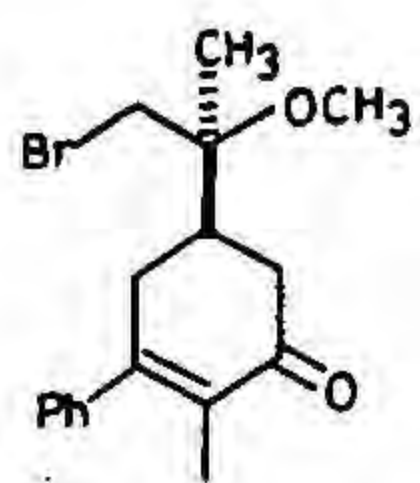
- | | |
|-----|---------------------------------|
| 8. | R |
| 9. | H |
| 9. | CH ₂ CH ₃ |
| 10. | CH ₂ Ph |
| 11. | COCH ₃ |

- | | |
|-----|---------------------------------|
| 13. | R |
| 13. | H |
| 14. | CH ₂ CH ₃ |
| 15. | CH ₂ Ph |
| 16. | COCH ₃ |

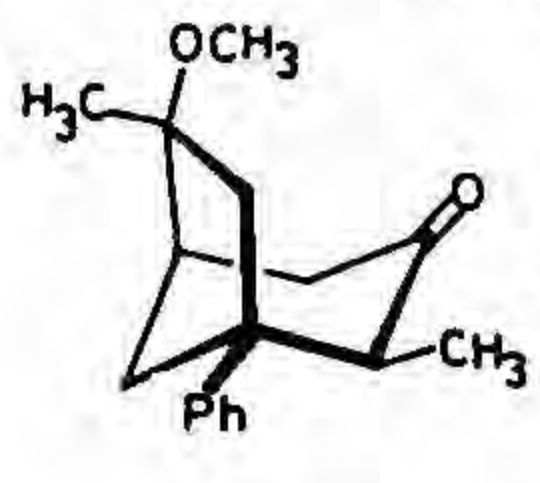


- | | |
|-----|-------------------|
| 24. | R |
| 25. | CH ₃ |
| 25. | COCH ₃ |

- | | |
|-----|-------------------|
| 26. | R |
| 27. | CH ₃ |
| 27. | COCH ₃ |

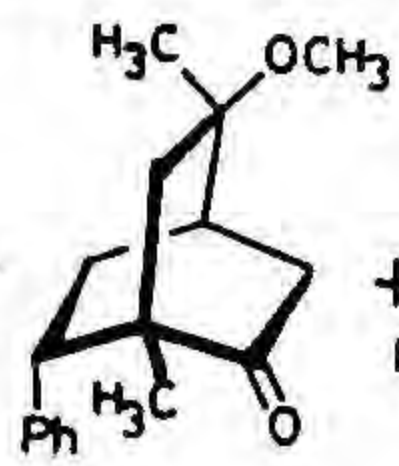


30



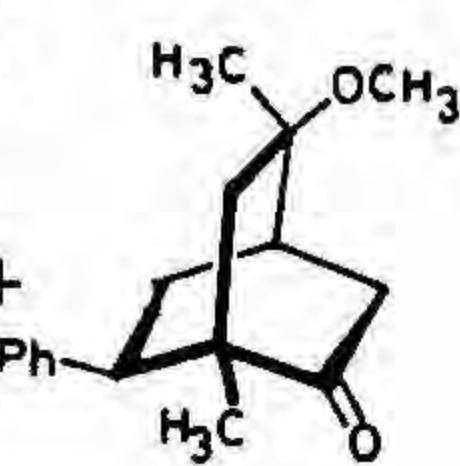
32

+

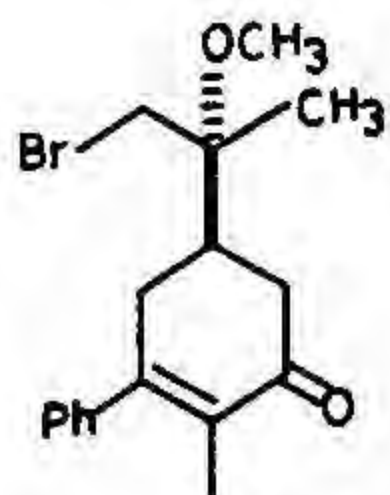


33

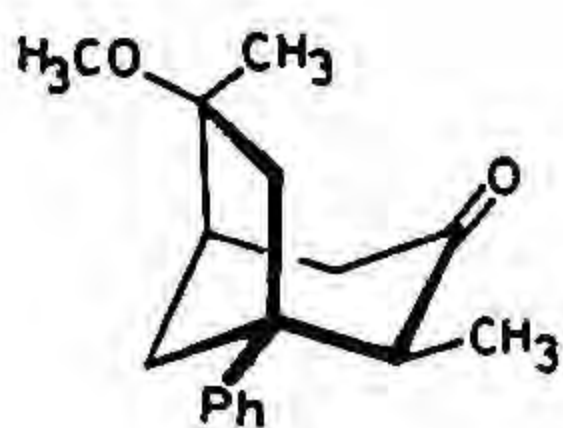
+



34

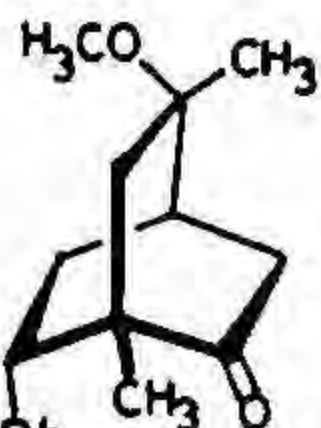


31



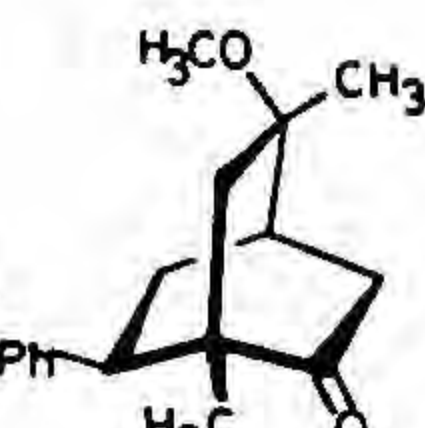
35

+

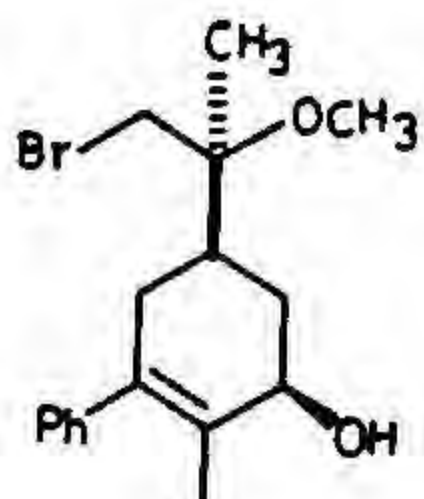


36

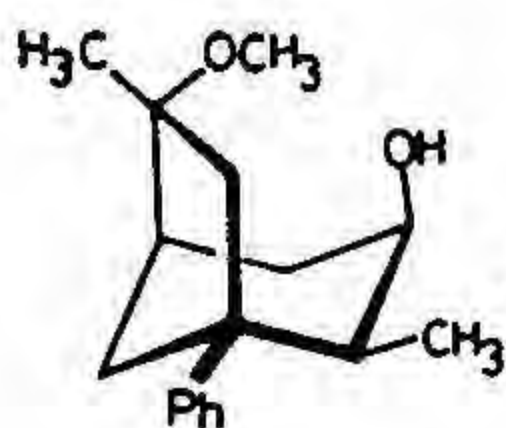
+



37

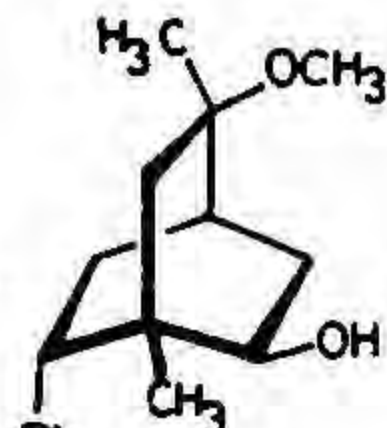


38



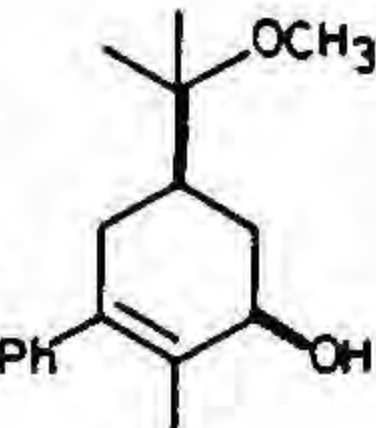
40 (47%)

+

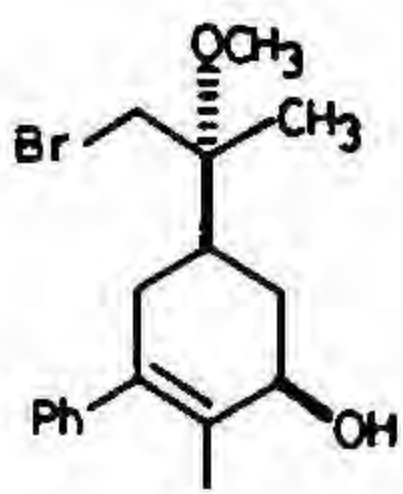


41 (25%)

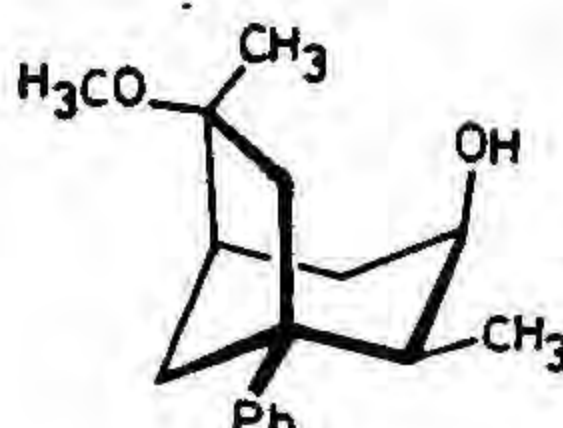
+



42 (12%)

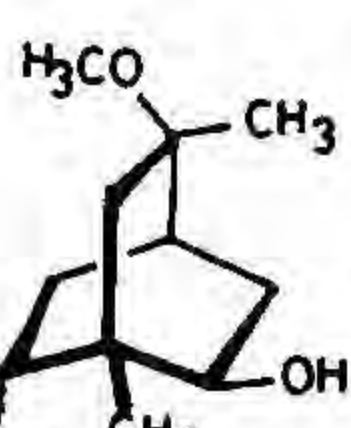


39



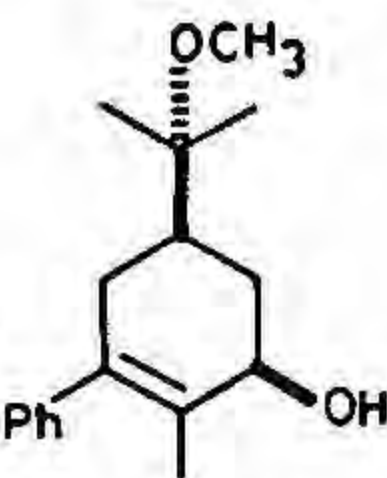
43 (15%)

+

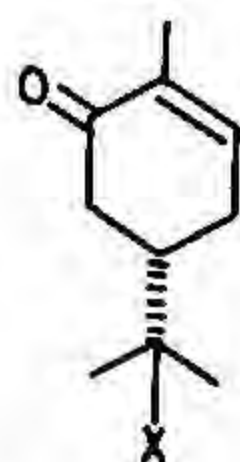


44 (45%)

+

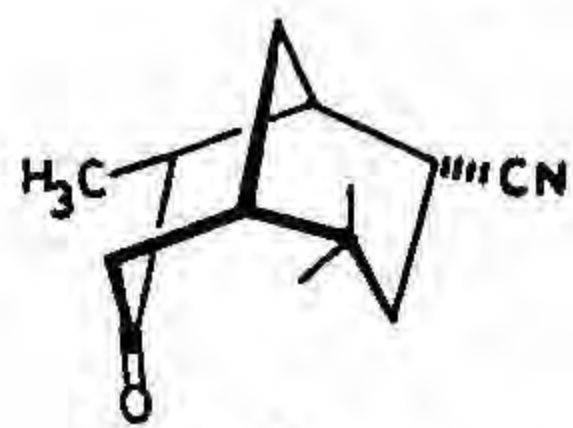


42 (30%)



45 X = Br

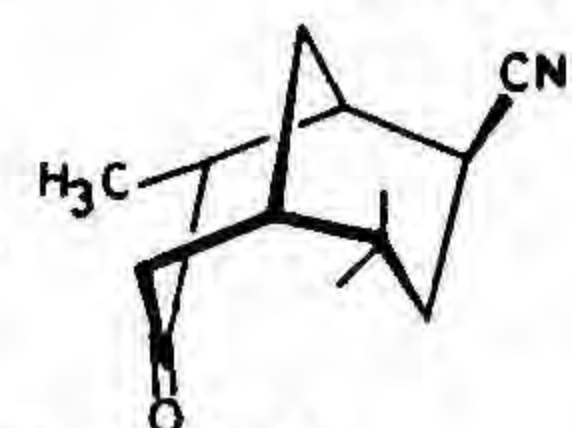
46 X = I



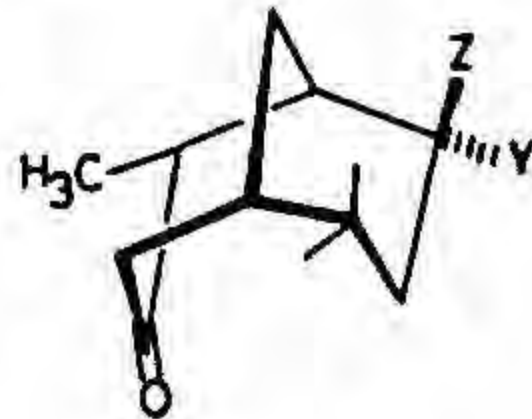
53

(2 : 1)

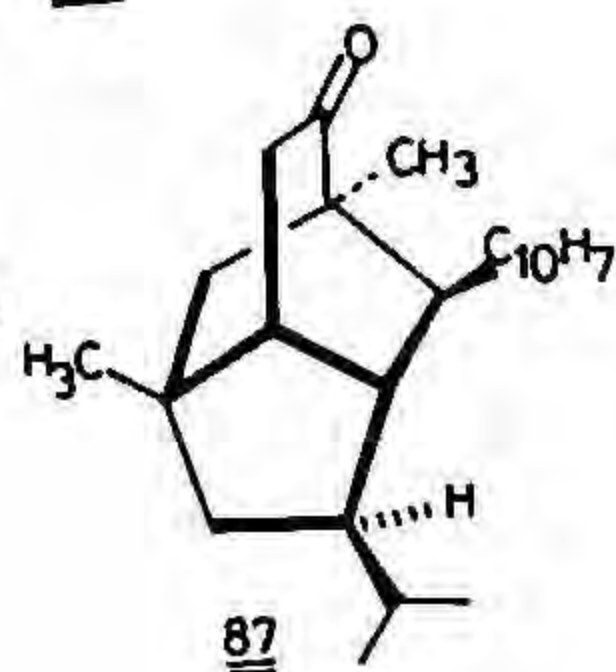
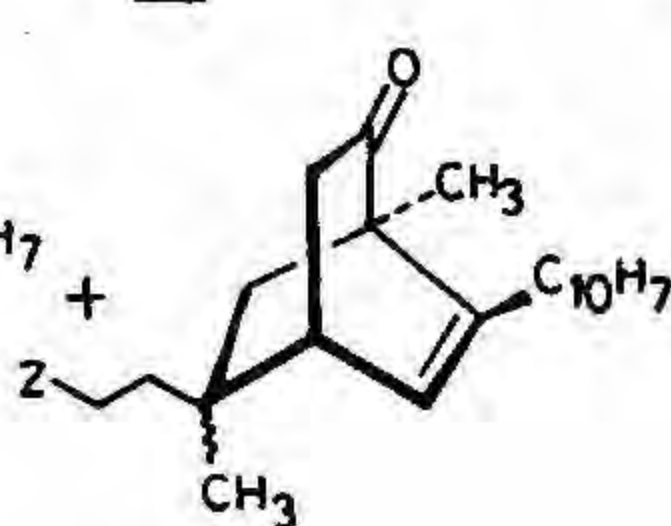
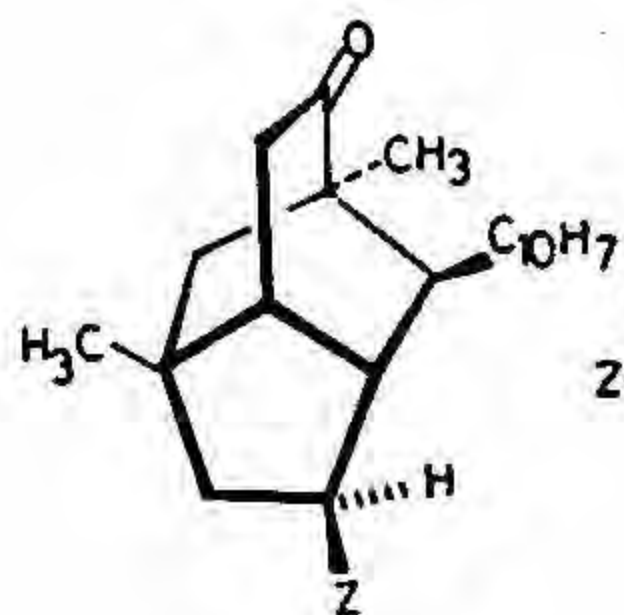
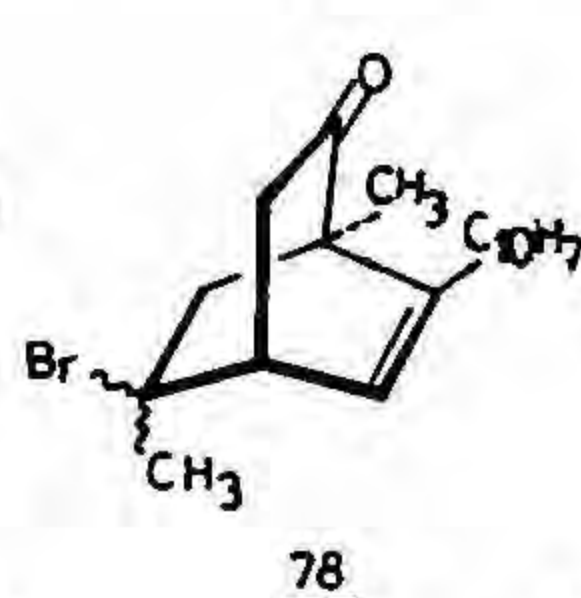
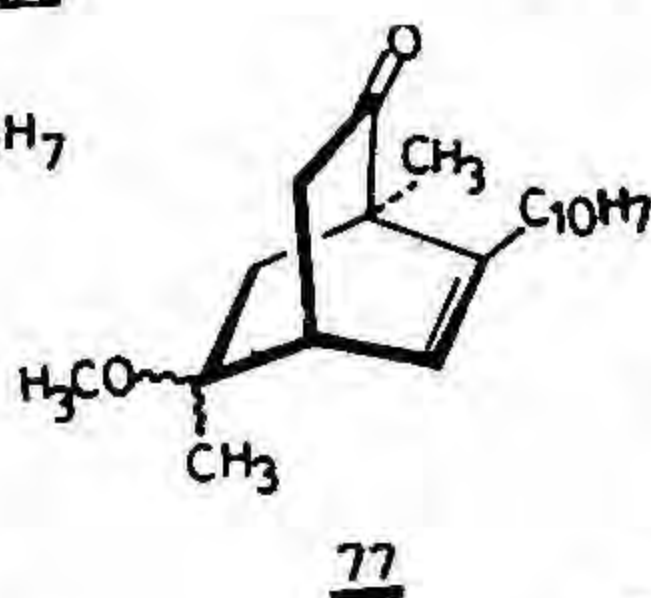
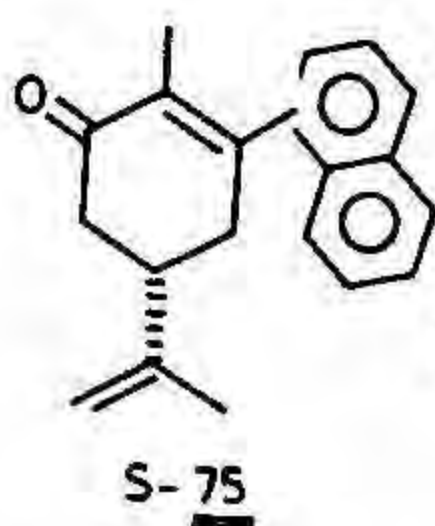
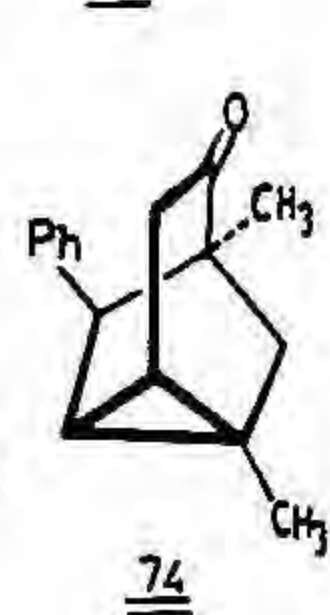
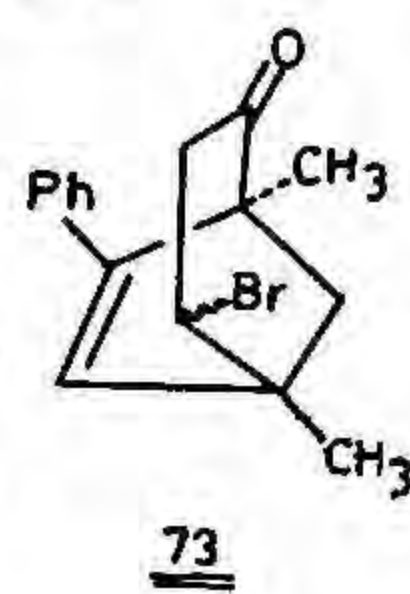
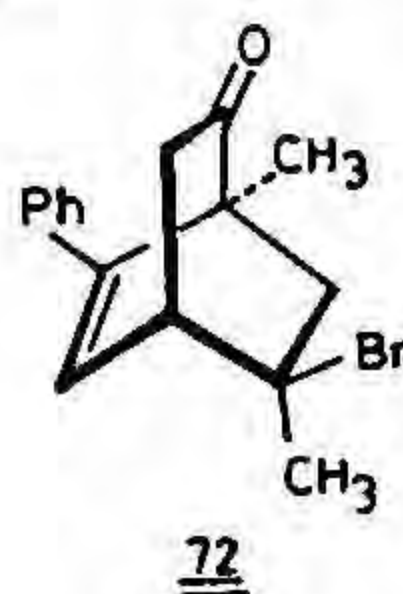
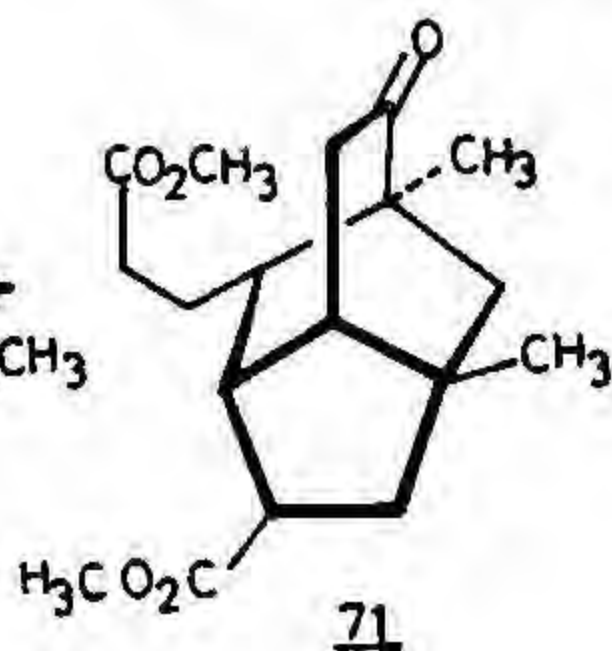
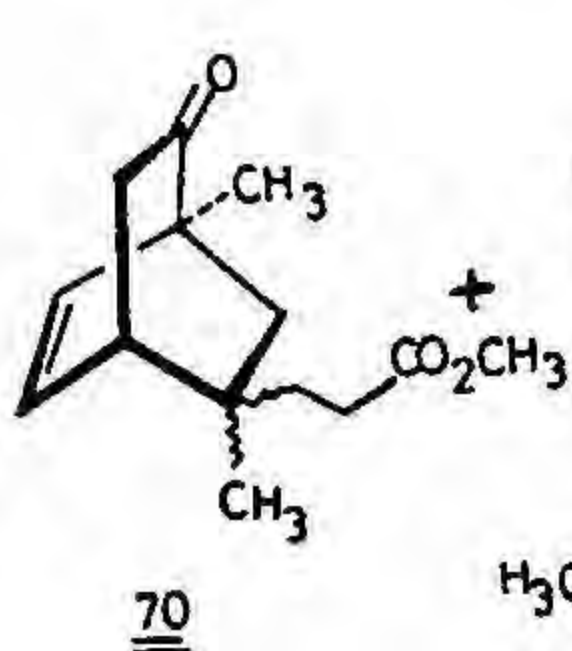
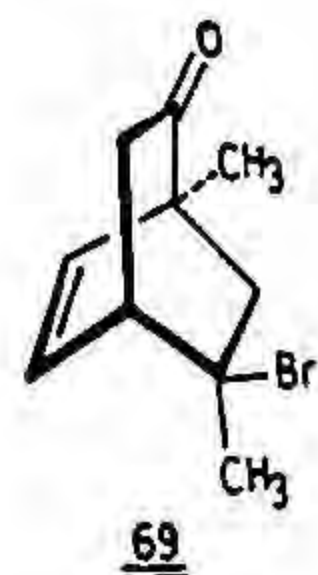
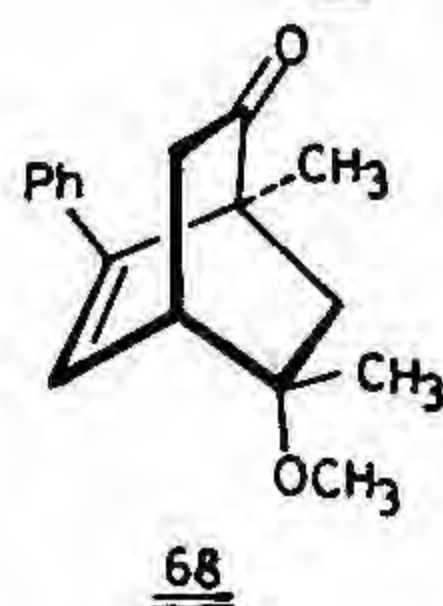
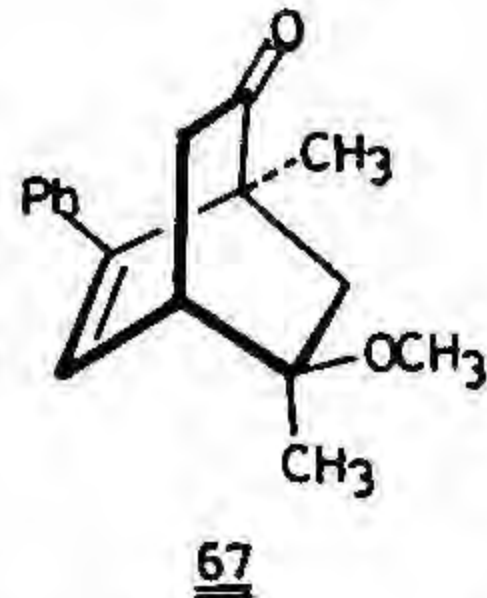
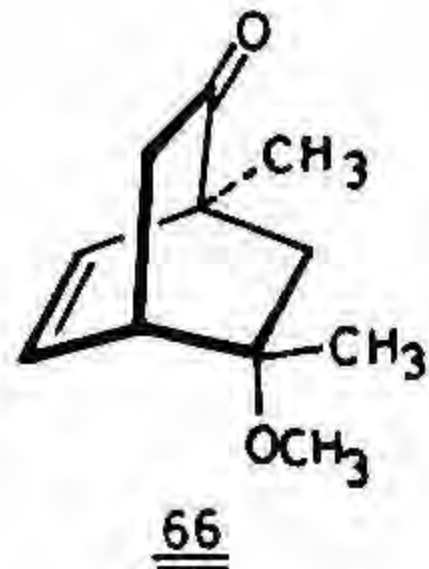
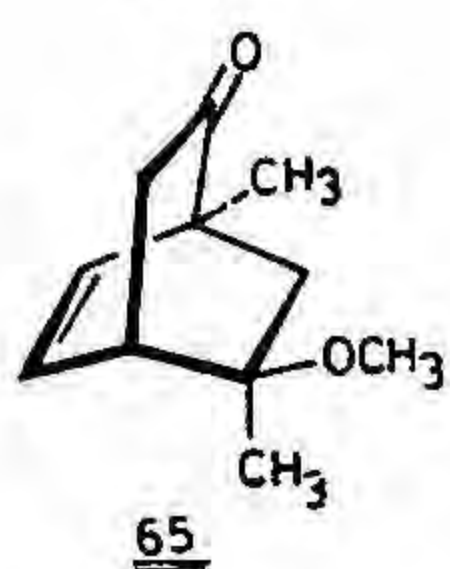
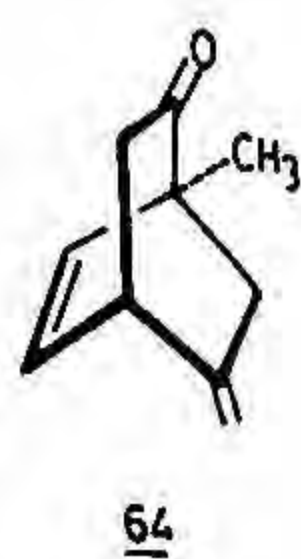
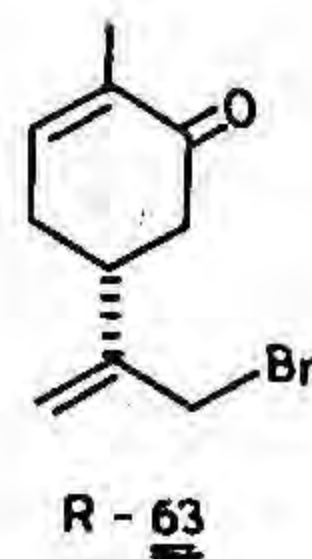
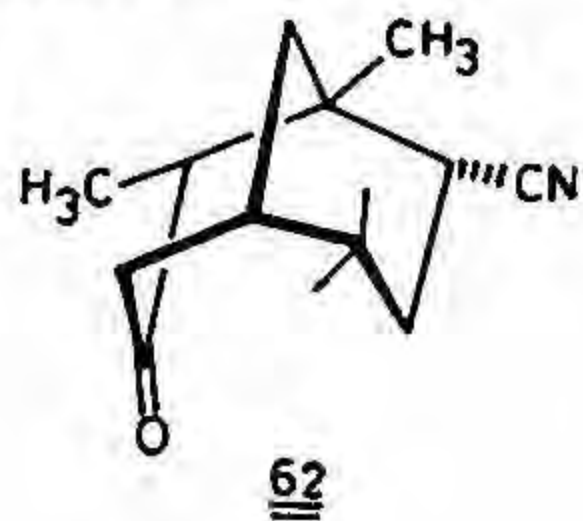
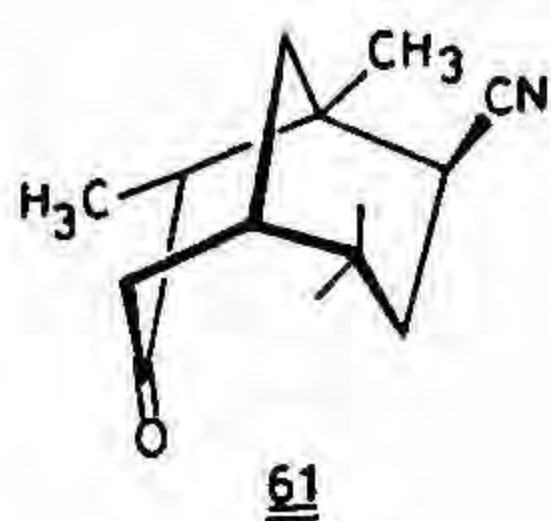
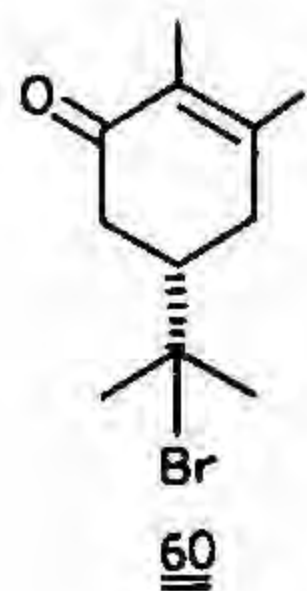
+



54



	Y	Z		Y	Z
<u>48.</u>	CO ₂ CH ₃	H	<u>55.</u>	CO ₂ CH ₃	H
<u>49.</u>	COCH ₃	H	<u>56.</u>	COCH ₃	H
<u>50.</u>	C ₆ H ₅	H	<u>57.</u>	C ₆ H ₅	H
<u>51.</u>	CH ₃	CN	<u>58.</u>	CH ₃	CN
<u>52.</u>	Cl	CN	<u>59.</u>	Cl	CN



79 : Z = CO₂CH₃

80 : Z = CN

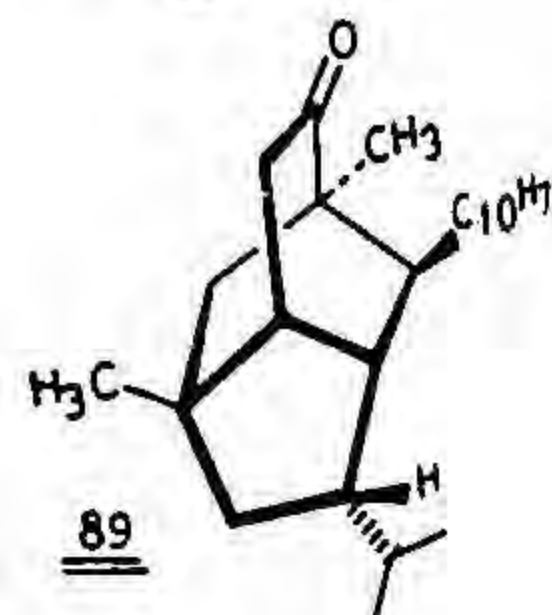
81 : Z = COCH₃

82 : Z = C₆H₅

83 : Z = CO₂CH₃

84 : Z = CN

85 : Z = COCH₃



88

89

To overcome the cyclopropane formation, the phenyl group was replaced by the bulky 1-naphthyl group, in anticipation that the electrophilic nature of the olefin will be decreased due to steric reasons. To this end, reactions were carried out with 6-(1-naphthyl)carvone (75). Regiospecific bromomethoxylation of the enone 75 with NBS in the presence of methanol followed by intramolecular alkylation of the resultant epimeric enone 76 furnished the bicyclic enone 77. Treatment of the enone 77 with boron tribromide yielded the bromoenone 78 as 2:1 mixture of epimers. Radical annulation of the bromoenone 78 with $^n\text{Bu}_3\text{SnH}$, AIBN and radicophiles 47–50 afforded the annulated products 79–82, along with the monoadducts 83–85¹¹.

Finally, the tricyclic compounds 79 and 81 were transformed to the analogues of pupukeanones 87 and 89. Selective Wittig reaction of the diketone 81 furnished the olefin 86. Hydrogenation of the olefin 86 afforded the epipupukeanone 87. On the other hand stereoselective hydrogenation¹² of the enone 88, prepared from the ketoester 79 via a Grignard reaction and dehydration, generated the naphthylpupukeanone 89.

References

1. RAMAIAH, M. *Tetrahedron*, 1987, 43, 3541-3676.
2. JASPERSE, C. P., CURRAN, D. P. AND FEVIG, T. L. *Chem. Rev.*, 1991, 91, 1237-1286.
3. SRIKRISHNA, A. AND HEMAMALINI, P. *J. Org. Chem.*, 1990, 55, 4883-4887.
4. BALDWIN, J. E. *J. Chem. Soc., Chem. Commun.*, 1976, 734-736.
5. SRIKRISHNA, A. AND HEMAMALINI, P. *Indian J. Chem. B*, 1990, 29, 152-153.
6. BUCHI, G. AND EGGER, B. *J. Org. Chem.*, 1971, 36, 2021-2023.
7. SRIKRISHNA, A. AND HEMAMALINI, P. *J. Chem. Soc., Perkin Trans. 1*, 1989, 2511-2513.
8. SRIKRISHNA, A. AND HEMAMALINI, P. *Indian J. Chem. B*, 1990, 29, 201-202.
9. CEKOVIC, Z. AND SAICIC, R. *Tetrahedron Lett.*, 1986, 27, 5893-5896.
10. SRIKRISHNA, A., SHARMA, G. V. R. AND HEMAMALINI, P. *J. Chem. Soc., Chem. Commun.*, 1990, 1681-1683.
11. SRIKRISHNA, A., HEMAMALINI, P. AND SHARMA, G. V. R. *Tetrahedron Lett.*, 1991, 32, 6609-6610.
12. FRATER, G. AND WENGER, J. *Helv. Chim. Acta*, 1984, 67, 1702-1706.

Thesis Abstract (Ph.D.)

Synthesis of bridged and spiro systems employing 3-*exo* and 5-*exo* radical cyclisation reactions by G. Veera Raghava Sharma

Research supervisor: A. Srikrishna

Department: Organic Chemistry

1. Introduction

The last decade had witnessed a dramatic growth in the use of free radicals for the construction of carbon-carbon bond in organic chemistry¹. By far, the most frequent applications of radical reactions have involved the formation of five-membered rings via 5-*exo* dig and trig cyclizations. However, for the construction of small rings using

radicals is highly unfavoured because the equilibrium lies too heavily in favour of the open chain radicals. Herein we describe the use of 3-*exo* trig, 5-*exo* trig and 5-*exo* dig radical cyclizations in the construction of chiral bi- and tricyclic- bridged compounds, and spiro systems present in natural products. In addition, a methodology to the chiral analogues of Cerapicanes and a novel benzannulation procedure have been described.

2. Results and discussion

Synthesis of chiral tricyclo[3.2.1.0^{2,7}]octanes **1** starting from carvone **2** via an efficient and exclusive 3-*exo*-trig radical cyclization of either a bicyclo[3.2.1]oct-6-en-2-yl radical or a bicyclo[2.2.2]oct-5-en-2-yl radical has been achieved. The radical precursors **3** and **4** were prepared from *S*-carvone via the β -aryl carvone **5a**, bromoenone **6a** and methoxy enone **7a**. Reaction of the methoxy enone **7** with boron tribromide furnished a mixture of bicyclo[2.2.2]octenyl **3** and bicyclo[3.2.1]octenyl **4** compounds. Treatment of the bromoketones **3** and **4** with tri-*n*-butyltin hydride in the presence of a catalytic amount of AIBN generated exclusively, the tricyclic ketone **1** via a 3 *exo* trig radical cyclization without the formation of any detectable amounts of either reduced or homoallyl-homoallyl radical rearrangement products².

Analogously, the radical precursors, *p*-anisyl, *o*-anisyl, phenyl ethynyl compounds **3b-d** and **4b-c** prepared from *S*-carvone in the same manner furnished the tricyclic ketones **1b-d**. However, α -naphthyl derivative **3f** failed to cyclize, due to the orthogonal arrangement of the naphthyl group with the olefin moiety because of steric reasons. This was proved by the 3-*exo* trig radical cyclization of the β -naphthyl compounds to the tricyclic ketone **1e**. In addition, a radical annulation methodology, via an intermolecular addition followed by 5-*exo*-trig radical cyclization of the resultant radical starting from the bromide **3f** and methyl acrylate, to the isotwistane **8** containing the molecular framework (12 out of 15 carbons in their place) identical to that present in the sesquiterpenes, pukeananes, has also been achieved³.

2.1. Synthesis of cerapicane analogues

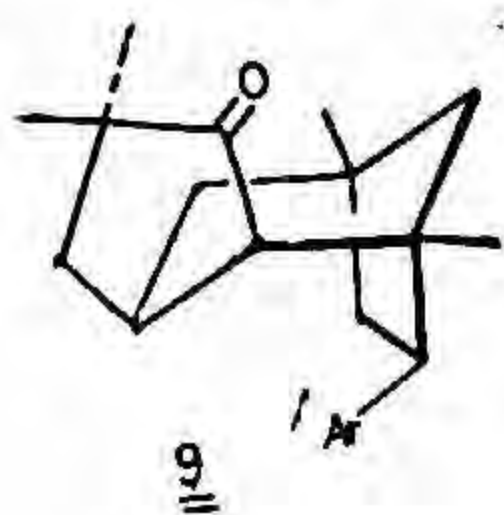
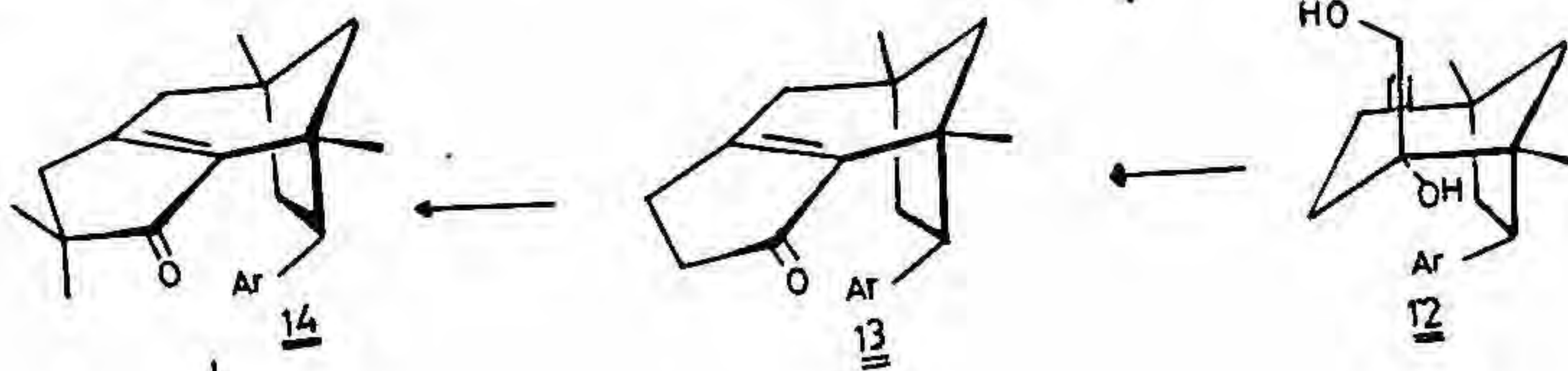
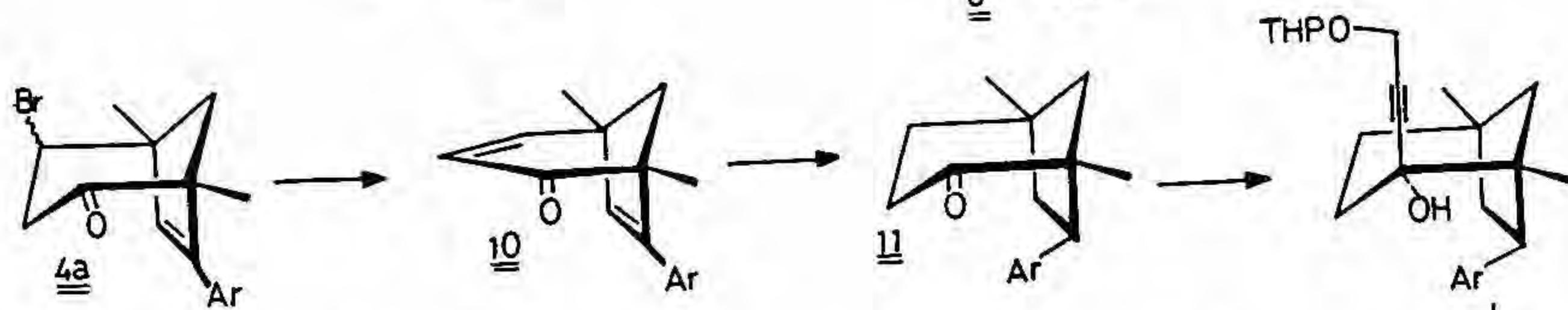
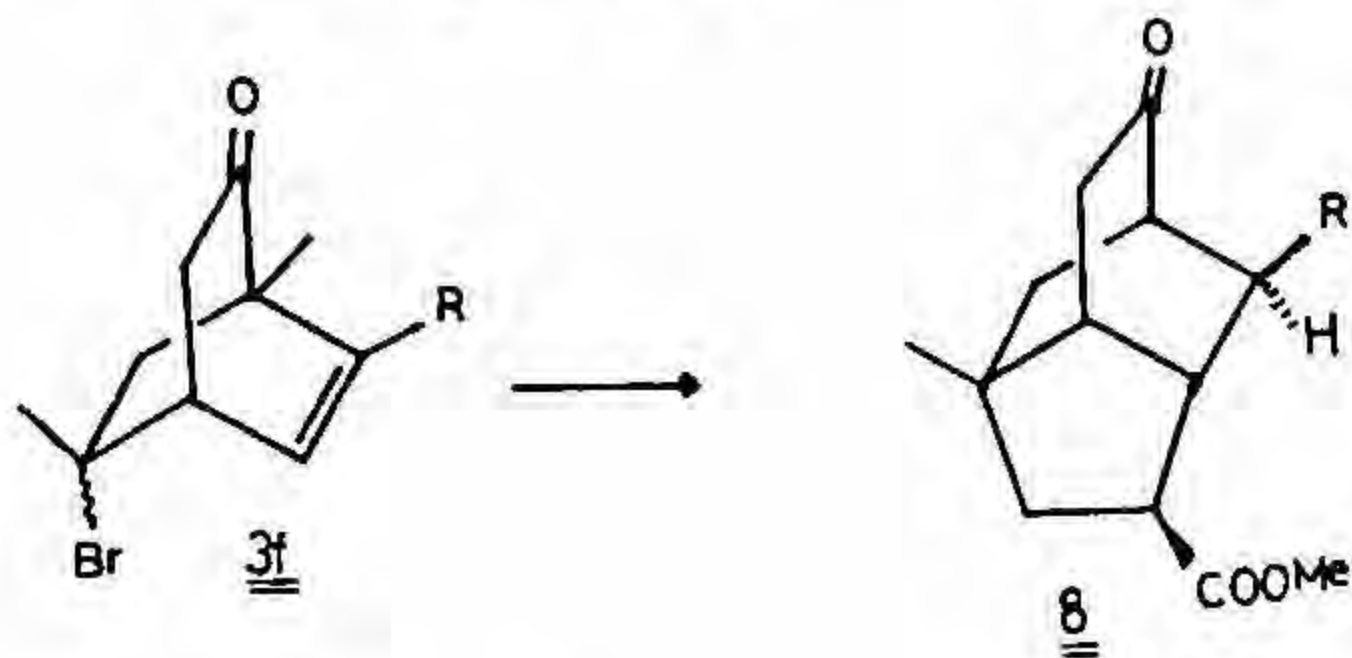
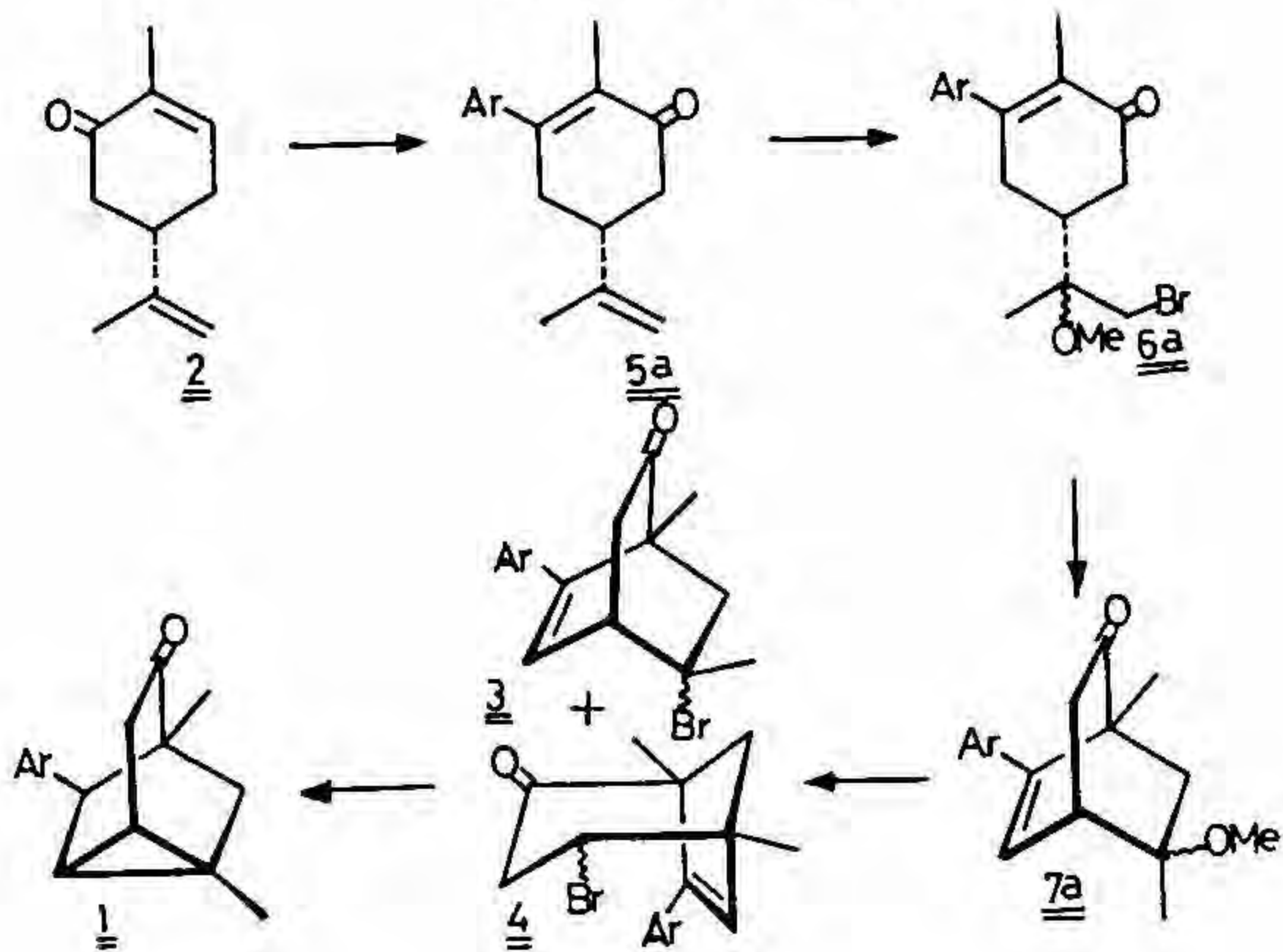
An enantiospecific total synthesis of (-)-(1*R*,1*S*,6*R*,8*R*,10*R*)-10-(*p*-tolyl)-1,4,4,8-tetramethyl tricyclo[6.2.1.0^{2,6}]undecan-3-one **9** containing the carbon framework of the sesquiterpene, cerapicol⁴ starting from (*R*)-carvone was achieved. (*R*)-Carvone was converted into the bromoketone **4a**. Dehydrobromination with 1,8-diazabicyclo[5.4.0]undec-7-ene followed by catalytic hydrogenation of the resultant dienone **10** transformed the bromoketone **4a** into bicyclic ketone **11**. Addition of the lithium salt of propargyl THP ether to the ketone **11** and deprotection of the THP ether gave the diol **12**. Nazarov-type cyclization of the butyn-1, 4-diol **12** with P₂O₅ in methanesulfonic acid yielded the cyclopentannulated product **13**. Methylation of the enone **13** furnished the cerapica-2(6)-en-3-one **14**. Reduction of the enone **14** using lithium in liquid ammonia reduction conditions generated the thermodynamic product **9a** a Cerapican-3-one chiral analogue.

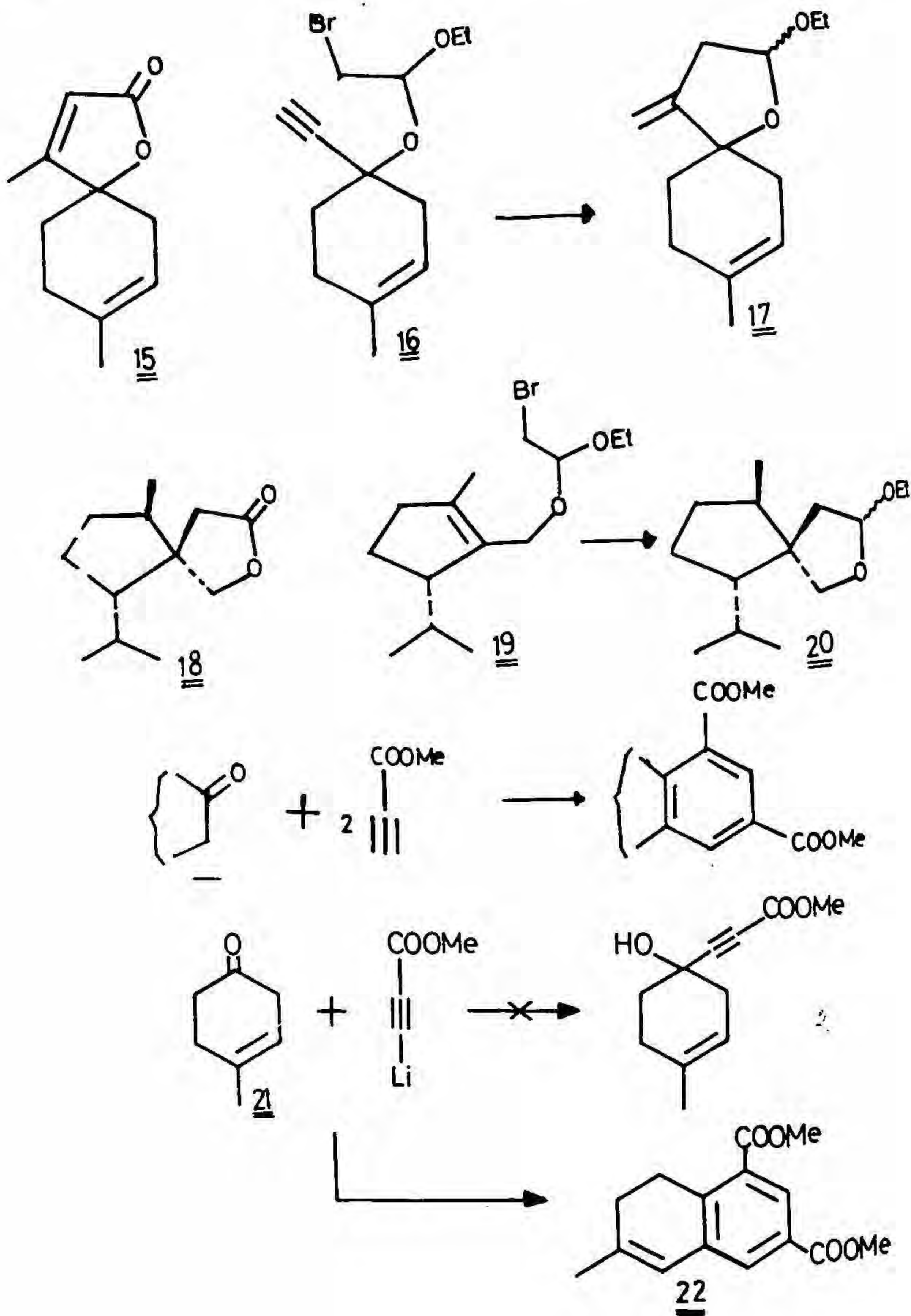
2.2. Synthesis of spiro lactones

First total synthesis of (\pm)-andirolactone **15**, a desisobutenyl sesquiterpene⁵ containing a γ , γ -spiro- β -methyl- γ -butenolide moiety isolated from *Cedrus libanotica*, was achieved starting from 4-methylcyclohex-3-enone using a 5-*exo* dig radical cyclization reaction (**16-17**) as the key step⁶. Synthesis of a new C-12 chiral synthon **18** containing a β , β -spiro- γ -butyrolactone moiety starting from limonene using a 5-*exo*-trig radical cyclization reaction **19-20** as the key step was accomplished⁷.

2.3. New benzannulation

A novel, one-pot, regioselective, *meta*-dimethoxycarbonyl benzannulation of Michael donors containing a COCH₂- moiety was discovered. Reaction of the 3-lithio derivative of methyl propynoate with 4-methylcyclohex-2-en-1-one **21** or alternatively, lithium dienolate of the enone **21** with methyl propynoate, contrary to the expected addition product, generated the dihydronaphthalene derivative **22** via a sequential Michael-Michael-intramolecular aldol-dehydration reactions. Oxidation of the dihydronaphthalene derivative **22** with DDQ furnished a naphthalene derivative conforming the structure of **22**. Generality of this new, one-pot, three-component *meta*-dimethoxycarbonyl benzannulation was established by the annulation of various Michael donors resulting in the aromatic products⁸.





References

1. RAMAIAH, M. *Tetrahedron*, 1987, 43, 3541-3675.
2. SRIKRISHNA, A., SHARMA, G. V. R. AND HEMAMALINI, P. *J. Org. Chem., Chem. Commun.*, 1990, 1681-1683.
3. SRIKRISHNA, A., HEMAMALINI, P. AND SHARMA, G. V. R. *J. Org. Chem.*, 1993, 58, 2509-2516.
4. HANESSEN, H. P. AND ABRAHAM, W.-R. *Tetrahedron*, 1988, 44, 2175-2180.
5. AVCIBASI, H., ANIL., H. AND TOPRAK, M. *Phytochemistry*, 1987, 26, 2852-2853.
6. SRIKRISHNA, A. AND SHARMA, G. V. R. *Tetrahedron Lett.*, 1988, 29, 6487-6488.
7. SRIKRISHNA, A., SHARMA G. V. R. AND NAGARAJU, S. *Synth. Commun.*, 1992, 22, 1221-1230.
8. SRIKRISHNA, A. AND SHARMA, G. V. R. *Tetrahedron Lett.*, 1989, 30, 3579-3580.

Thesis Abstract (Ph.D.)

Labelled clustering and its applications by V.Sridhar

Research supervisor: M.Narasimha Murty

Department: Computer Science and Automation

1. Introduction

Clustering is a process of grouping a collection of objects. Clustering approaches can be broadly categorized into conventional and knowledge-based approaches. In a conventional approach, objects are typically represented as points in an n -dimensional space and the essential ingredients of clustering algorithm such as similarity measure and/or objective function to be optimized are implicitly represented. On the other hand, in knowledge-based approaches, the objects are typically described using linguistic concepts such as round, shape, color, red, etc., and the background knowledge contains goals of clustering, cluster validating criterion, etc. A well-known example of knowledge-based clustering is conceptual clustering¹. Here, the object descriptions are logical expressions of the form: $[color=red] [shape=round][size=medium]$. It is to be observed that the above logical expression is a conjunction of three primitive concepts: $[color=red] [shape=round]$ and $[size=medium]$. The conceptual clustering algorithm operates on these descriptions, using the background knowledge, to generate clusters and their descriptions that optimize a lexical evaluation function. Second example of knowledge-based clustering is functional clustering². Even in this case, objects are described using linguistic concepts. However, the background knowledge now contains information regarding functionalities of various objects. More specifically, the knowledge contains information regarding various sub-concepts that are essential to realize a super-concept. For example, the concepts *cutting*, *lathering*, and *mirroring* are essential concepts to realize the concept of *shaving*. Given a collection of objects described using the concepts such as *cutting*, the functional clustering algorithm generates clusters with the highest level concepts (based on the knowledge) that can be realized as cluster descriptions. Clustering algorithms (both conventional and knowledge based) described in the literature operate on unlabelled objects. More specifically, objects are described using the properties of the objects rather than the concepts that label them. For example, a cricket ball might be described as $[color=red] [size=medium] [shape=round]$. In this thesis, we describe clustering approaches that operate on labelled objects. The clustering algorithms proposed in this thesis operate on the labels of the objects such as *cricket ball*.

2. Labelled clustering

The labelled clustering approach is based on the following fundamental observation: Humans tend to use the most appropriate general description to describe a collection of objects. For example, when we take a walk within a campus, we talk about *cycles* and *scooters*. On the other hand, while we stride along a main road, we worry about sound and air pollution caused by *vehicles*. Observe, how the description has been generalized from *cycles* and *scooters* to *vehicles*. Similarly, if we watch from a balcony or our house, we see *crows* and *sparrows* whereas we go for *bird* watching to a bird sanctuary. In the following, we describe two approaches to achieve labelled clustering: deductive clustering approach and model-theoretic approach to clustering.

3. Deductive clustering approach

The proposed deductive clustering approach^{3,4} (DCA), a knowledge-based clustering approach, operates on labelled objects to generate clusters and their descriptions. The approach utilizes the knowledge represented in the form of a hierarchy (more specifically, a rooted directed acyclic graph). Cluster descriptions generated by DCA are the most plausible generalizations given the knowledge and a collection of input objects. Typically, the object labels correspond to the leaf nodes of the hierarchy. We have used logic as a framework for representing knowledge as well as to describe the clustering approach. We have proposed a modified first-order logic that characterizes the clustering approach. The proposed logic is a nonmonotonic logic and has both proof theory and model theory. A formula denoting a cluster description along with the associated objects is a logical consequence of the proposed theory and hence the name deductive clustering. We have also described an algorithm to realize the DCA and implemented the same in the context of reviews drawn from *ACM Computing Reviews*. The source of domain knowledge is the Full Computing Reviews Classification Scheme. The DCA, here, can be viewed as a proof-theoretic approach to clustering.

4. Model-theoretic approach to clustering

We have also investigated a model-theoretic approach⁵ to clustering. Here again, we use first-order logic as a framework to characterize clustering. We defined the notion of maximal models to describe clusters. More specifically, we partition a collection of well-formed formulas, Δ_K , describing the proper axioms (that include domain knowledge as well as input objects) into three blocks: $\Delta_R \subseteq \Delta_K$ are relationships with exceptions, $\Delta_C \subseteq \Delta_K$ are constraining relationships, and $\Delta_H \subseteq \Delta_K$ are hierarchical relationships. The maximal model defines with respect to the set $\Delta_R \cup \Delta_C$ and each such maximal model defines a cluster. We remark that Δ_C constrains the number and nature of the generated clusters. We have proposed an algorithm to achieve this sort of clustering and investigated the same in the context of library books. The source of domain knowledge is the Dewey Decimal Classification Scheme. In the following two sections, we describe the applications of the labelled clustering approach.

5. Application: Semantic modeling of database

We have pointed out that labelled clustering tends to identify the most plausible general label of a collection of objects. Thus labelled clustering can be viewed as an act of data abstraction. As a consequence, it finds applications in modeling databases^{6,7}. Such an extended semantic data model can facilitate not only answering structure-dependent queries such as "How good a library is with respect to artificial intelligence area?" but also the comparison of databases using a labelled clustering approach such as DCA with respect to this common hierarchy. We achieve the (qualitative) comparison of databases by comparing the respective cluster structures. We have implemented the proposed scheme in the context of library book databases.

6. Application: Belief revision

Another interesting application of the labelled clustering is in the context of belief revision⁸⁻¹⁰. The problem of belief revision is to keep a database of beliefs consistent (in other words, there should not be any contradiction in the collection of beliefs) and is an active field of research within artificial intelligence. We have proposed the object-centered belief revision in which the belief revision can be restricted to a small number of related clusters of beliefs. Specifically, we have proposed an axiomatic approach to model belief revision. In order to represent

knowledge that includes default knowledge syntactically as well as semantically using logic, we have used two implication operators: \rightarrow (conventional material implication operator of first-order logic for ISA relationships) and $>$ (a logical operator introduced to deal with default relationships). The problem of multiple inheritance with exceptions is handled by defining nonmonotonic transitive closures and using the same in defining the nonmonotonic inference rule (in lieu of modus ponens of first-order logic). The proposed logical system is a 3-tier system that deals with contexts and reasons consistently with the most recent beliefs. In order to achieve reasoning with the most recent beliefs, we represent input beliefs in a reified form that accounts for contextual as well as temporal information. The proposed belief revision model has been employed to model the beliefs, about patients, of a physician in allopathy and ayurveda contexts.

7. Future work

In this thesis, we have proposed a clustering approach called labelled clustering approach. We have discussed two possible ways of realizing labelled clustering and two applications of the labelled clustering approach. Further work can be carried out along the following lines:

1. Extending the DCA to handle default knowledge. This is very useful in achieving inductive question-answering.
2. Providing a framework for learning default knowledge¹¹.
3. Providing a formalization of maximal model¹².
4. Extending the 3-tier logical system to model human decision-making¹³.

References

1. MICHALSKI, R. S. AND STEPP, R. E. Learning from observation: *Conceptual clustering*. In *Machine learning: An AI based approach*, (Michalski, R.S., Carbonell, J. G. and Mitchel, T. M., eds) Vol. I, 1983, Morgan Kaufmann, California.
2. SHEKAR, B., MARASIMHA MURTY, M. AND KRISHNA, G. A knowledge-based clustering scheme, *Pattern Recognition Lett.*, 1987, 5, 253-259.
3. SRIDHAR, V. AND NARASIMHA MURTY, M. A knowledge based clustering algorithm, *Pattern Recognition Lett.*, 1991, 12, 511-517.
4. SRIDHAR, V. AND NARASIMHA MURTY, M. Deductive clustering approach, *Theor. Appl. Artif. Intell.*, 1994, 6, 195-237.
5. SRIDHAR, V. AND NARASIMHA MURTY, M. A model-theoretic approach to clustering, *Knowledge-Based Systems*, 1991, 4, 87-94.
6. SRIDHAR, V. AND NARASIMHA MURTY, M. Clustering algorithms for library comparison, *Pattern Recognition*, 1991, 24, 815-823.
7. SRIDHAR, V. AND NARASIMHA MURTY, M. A knowledge based clustering algorithm for data abstraction. *Knowledge-Based Systems*, 1994, 7, 103-113.
8. SRIDHAR, V. AND NARASIMHA MURTY, M. Reasoning with perceived information: A case for non-monotonic reasoning, *J. Indian Inst. Sci.*, 1990, 70, 101-120.
9. SRIDHAR, V. AND NARASIMHA MURTY, M. Nonmonotonic logics for belief revision, *Comput. Artif. Intell.*, 1993, 11, 23-46.
10. SRIDHAR, V. AND NARASIMHA MURTY, M. Belief revision: An axiomatic approach, *J. Intell. Robotic Systems. Tech. Applic.*, 1993, 8, 127-153.
11. SRIDHAR, V. AND NARASIMHA MURTY, M. Learning defaults: Recognizing patterns in beliefs, *J. Instn. Electronics Telecommun. Engrs.*, 1991, 37, 512-520.

12. SRIDHAR, V., NARASIMHA MURTY, M. AND KRISHNA, G. Minimal models and real-world models. In *Proc. Applications of Artificial Intelligence VIII*, 1991, Orlando, Florida.
13. SRIDHAR V. NARASIMHA MURTHY, M. AND KRISHNA, G. A logical model for decision making. In *Proc. 1989 IEEE Int. Conf. on SMC*, 1989, Cambridge, Mass.

Thesis Abstract (Ph. D.)

Notch fatigue under aircraft spectrum loading by V. Raghu Prakash

Research supervisor: M. N. Srinivasan

Department: Mechanical Engineering

1. Introduction

Fatigue often restricts the endurance of built-up metallic structures. Fatigue damage occurs due to the initiation and growth of one or more cracks at stress raisers under the action of random load history, typical of service environment. Enhanced performance requirements of aircraft structures often involve high-design stress levels that increase the probability of local yield resulting in accelerated crack initiation and growth at stress concentrators. While long crack growth under spectrum loading has been studied for many years, extension of fracture mechanics concepts to model short crack growth behavior under spectrum loading is currently of practical interest.

The following aspects of fatigue damage accumulation were considered in this work:

- Significance of spectrum representation to cumulative damage analysis,
- Notch root crack opening behavior under inelastic loading,
- Notch root small crack growth rates under specially programmed load sequences, and
- Estimation of notch root crack growth under spectrum loading.

The goal was to develop an empirical model to predict the growth of small cracks at a notch under spectrum loading. The modelling effort was based on the observation¹, that in a random load sequence, the major cycle

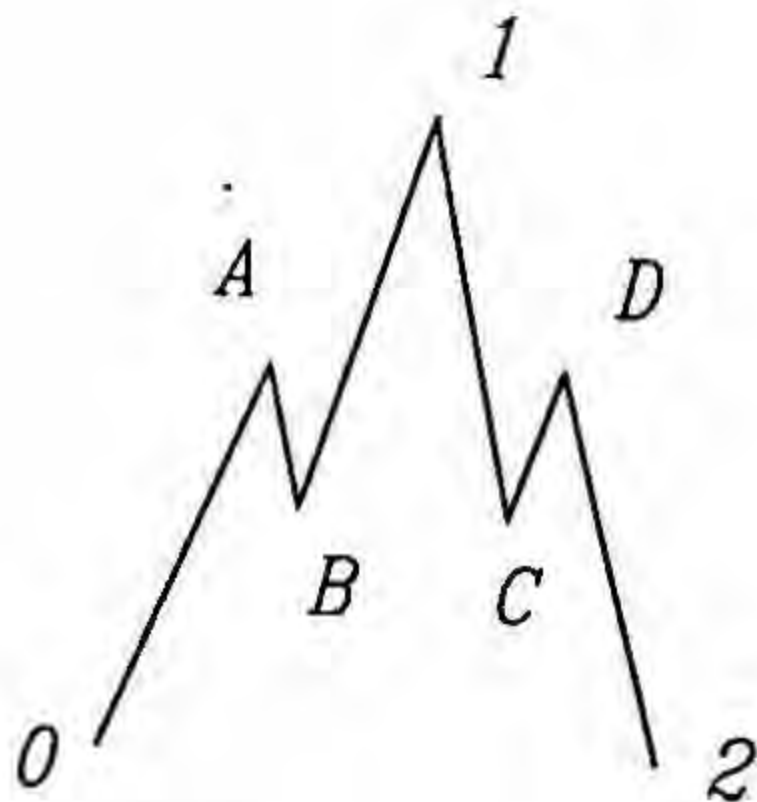


FIG 1a. Source load sequence containing two minor cycles A-B and C-D embedded in major cycle 0-1-2. Notch root stress-strain response is shown in (e).

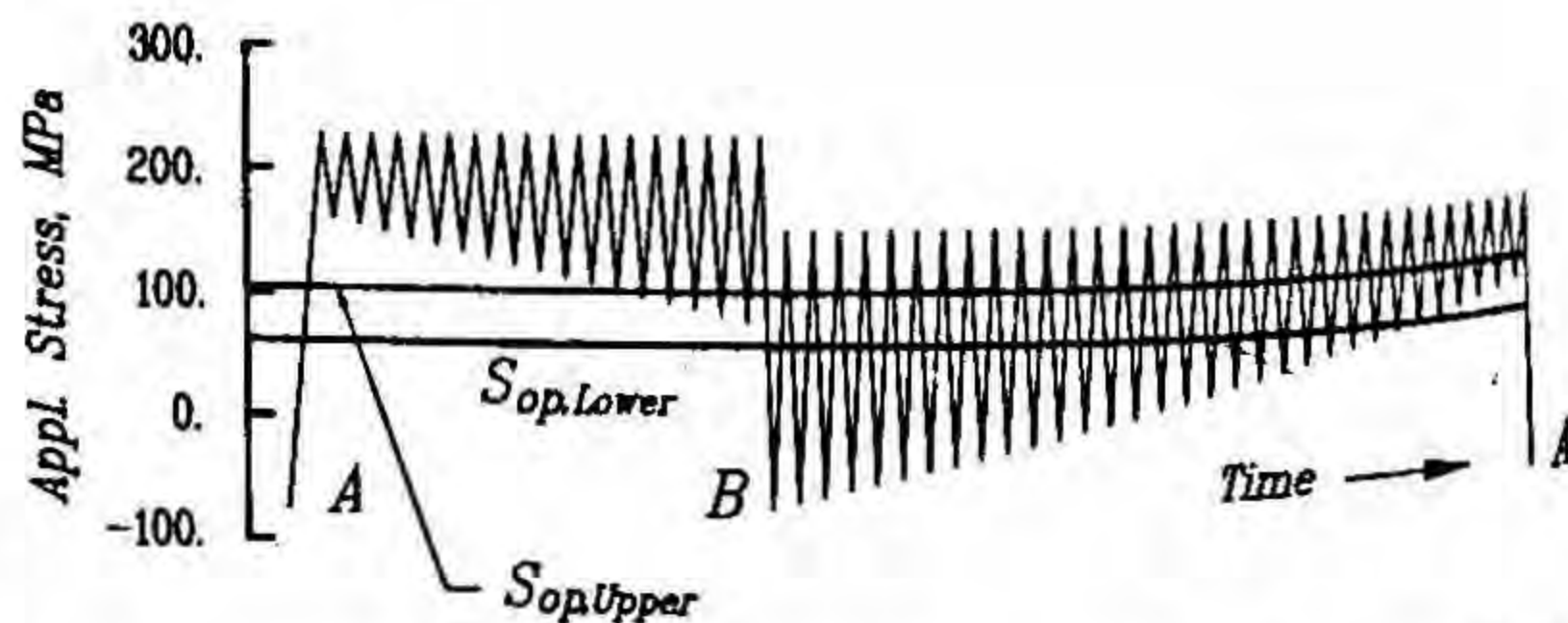


FIG 1b. Programmed load sequence used to determine the upper and lower bound of crack-opening stress for notch cracks under conditions of cyclic inelasticity. Crack-opening stress for minor cycles of (a) are sequence sensitive and their bound values are determined by major cycle 0-1-2.

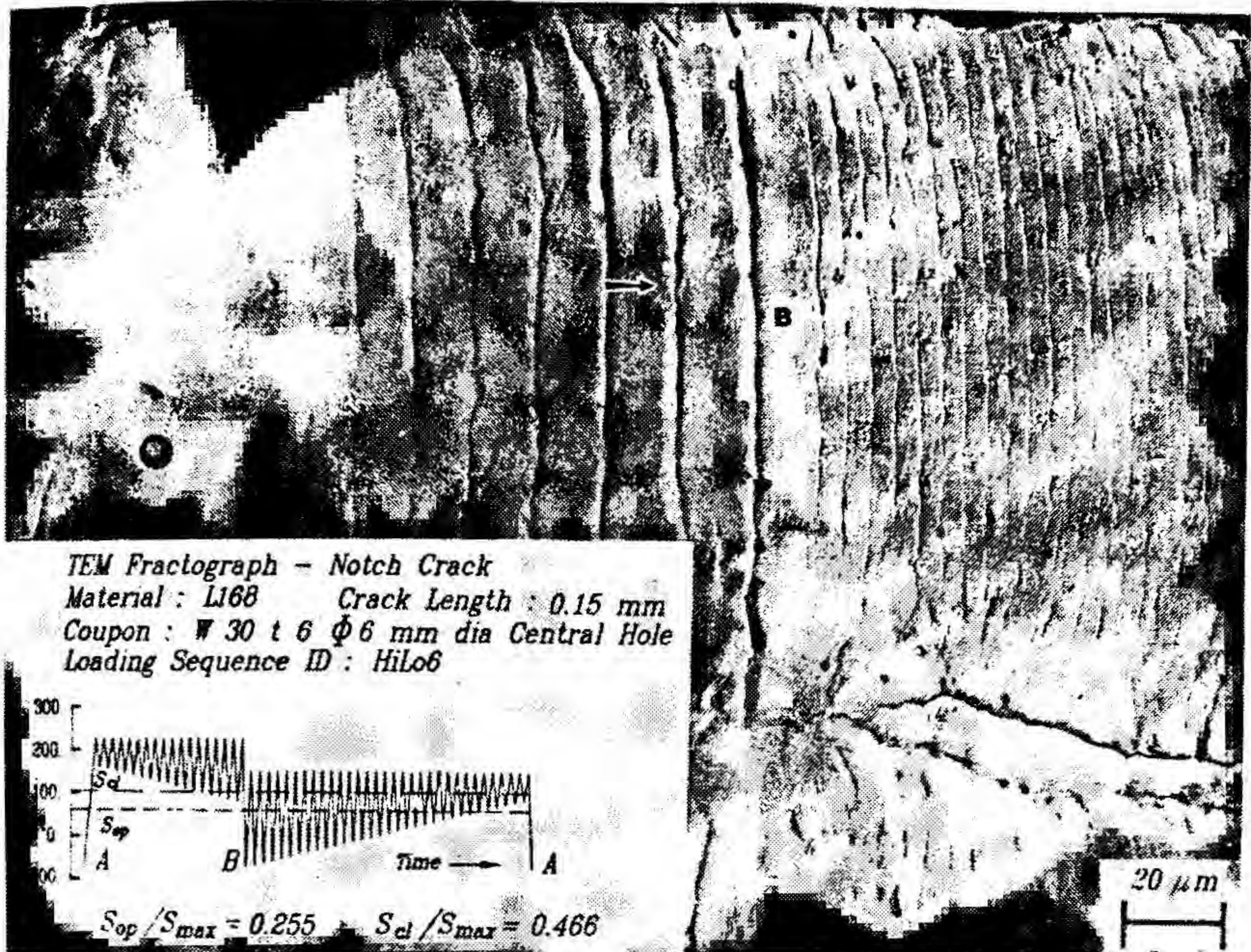


FIG 1c. Fractograph from the load sequence in (b). Bounds on opening stress are determined from equally spaced striations from the two blocks in (b). Crack length 0.15 mm from notch root under inelastic loading.

in the spectrum controls the extent of variation of crack opening stress in individual cycles. It was also assumed that crack extension over cycles between major cycles is negligible when compared to plastic zone size. Thereby, crack extension-related transients in crack opening stress were neglected and load interaction effects are related to cycle-by-cycle material hysteresis. Earlier work had demonstrated a similar pattern for fatigue damage in crack initiation². Figure 1 schematically explains the concept.

2. Experimental

An experimental investigation using specially designed programmed load sequences was undertaken to study crack closure at notches on an Al-Cu alloy (2014-T6511). Notch coupons were tested to failure under load sequences similar to that shown in Fig. 1b and then studied using transmission electron fractography. The number of equally spaced striations in a single block of loads determines the crack-opening stress, S_{op} . By counting equally spaced striations for cycles on falling and rising half of the major cycle in the programme, upper and lower limits of crack-opening stress variation was estimated (Fig. 1c). Figure 1d summarizes the interval of variation in crack-opening stress for a long, short and notch crack. The highest variation in crack-opening stress level was observed for notch inelastic conditions. Crack-opening stress for individual small cycles embedded in a large cycle is described by a linear hysteretic model (Figs 1e-f). Strain intensity corrections after El Haddad *et al.*³ were incorporated in the notch crack growth model to account for inelasticity at the notch.

The model estimates were validated against experimental growth rate data for short, notch cracks under a standardized fighter aircraft load spectrum (FALSTAFF). Precise estimation of crack length and growth rate is

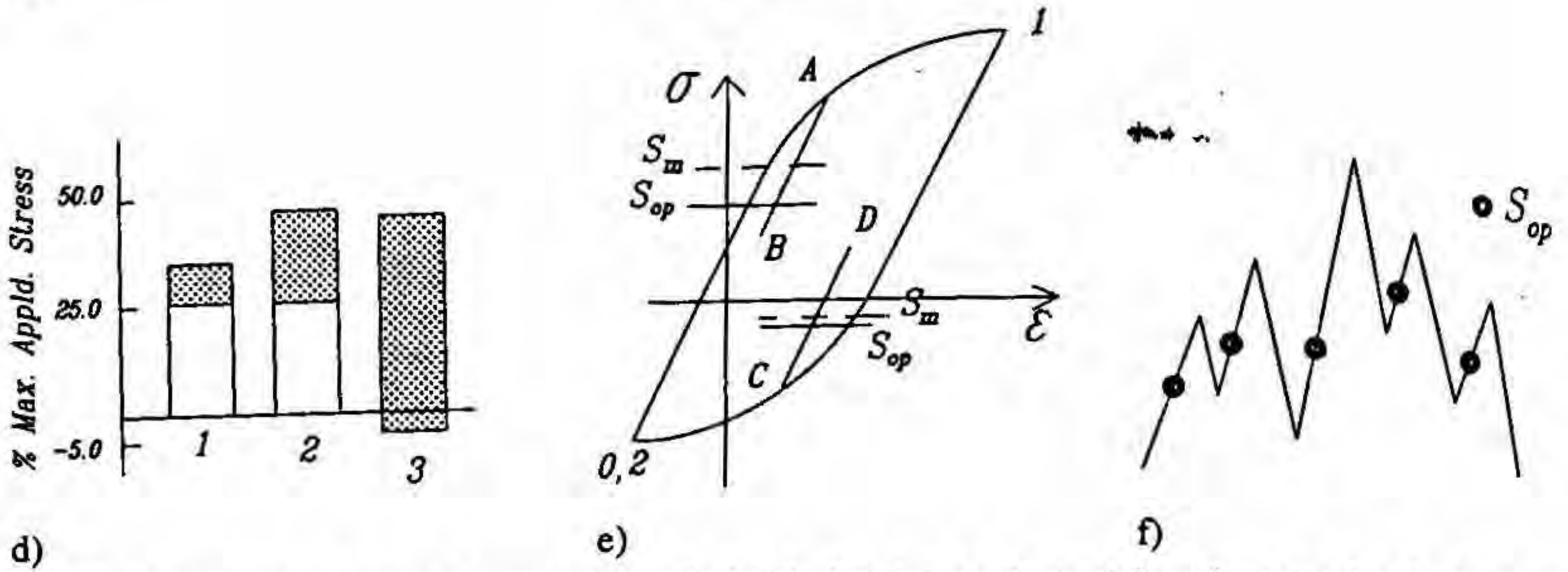


FIG 1d. Bounds on crack opening stress shown by hatched region as obtained from fractography. Applied maximum stress: 1. Long crack: Mpa, 2. Short crack, smooth specimen: 275 Mpa, 3. Notch cyclic inelastic crack: 275 Mpa. Highest variation in opening stress is observed under cyclic notch inelasticity.

FIG 1e. Notch root (local) stress-strain response to applied loads shown in (a). Local mean stress and crack-opening stress response are qualitatively similar.

FIG 1f. Hysteretic crack opening stress response as determined from bounds on opening stress for a random load sequence.

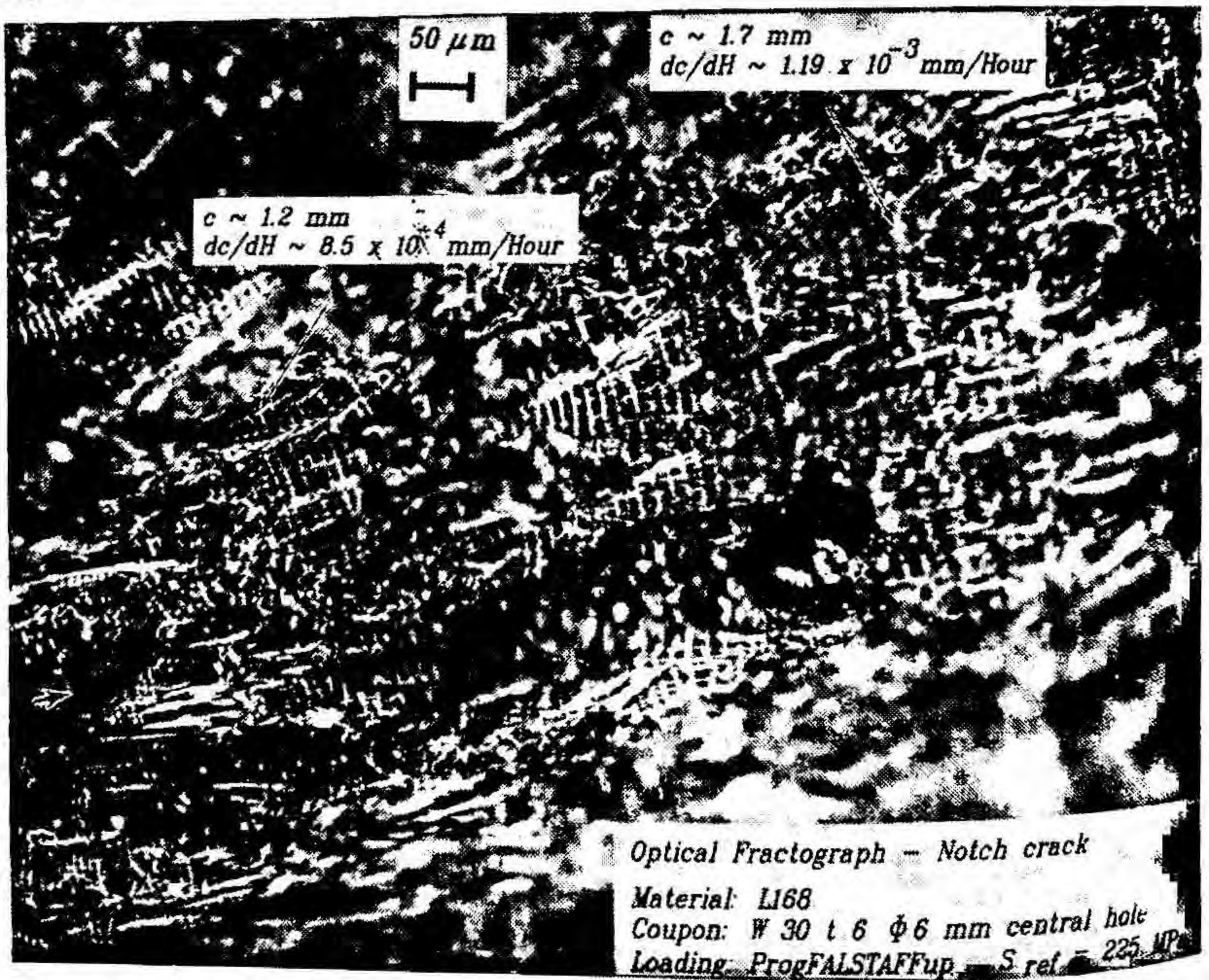


FIG 2a. Fatigue crack growth from a circular hole under programmed FALSTAFF load sequence. Applied maximum reference stress: 275 Mpa. Eighteen consecutive striations observed under an optical microscope determine crack growth in 200 flights.

important for such validation. Replica and *in-situ* optical microscopic techniques have shown considerable scatter in short crack growth rates⁴. In this work, optical fractography was used for notch root crack growth rate characterization. FALSTAFF was modified into a programmed load sequence designed to leave behind discernible marker bands on the fracture surface. Figure 2a shows typical optical fractograph for a notch crack. The 18 major loads of FALSTAFF are seen as ten and eight striations on the fracture surface. Damage equivalence of the programmed and randomized versions of the FALSTAFF was supported by results of tests on SE(T) specimens with long cracks, which also demonstrated good correlation between optical fractography and compliance-based crack growth rate estimates (Fig. 2b).

Multiple fatigue crack initiators were observed at the notch root. The crack that initiated first influenced the growth of other cracks, and is therefore referred to as the dominant crack. Shown in Fig. 2c is the crack growth rate *versus* crack length plot for different crack origins. The growth rate of the dominant crack is typically the lowest and is shown by a line.

3. Model predictions

Figure 3 summarizes crack growth rate prediction results. Conservative crack growth rate estimates were obtained using a (lower bound) constant crack-opening stress level of -4.0% of S_{max} . Unconservative estimates used $S_{op} = 35.0\% S_{max}$ (long crack closure level) as opening stress. The experimental data for dominant crack are shown by symbols, and the model predictions are shown by a solid line in Figs 3a–b.

Modelling hysteretic closure behaviour and accounting for strain inelasticity permits more accurate crack growth rate estimates as shown by the thick line in Figs 3a–b. Figure 3c summarizes prediction quality of the proposed model under spectrum loading over a wide range of applications: long cracks under elastic loading, short notch cracks under low and high stress levels.

4. Conclusion

The results of this study indicate that hysteresis in crack closure behaviour can explain load sequence sensitivity of notch fatigue damage. An empirical model based on constant amplitude long crack growth data,

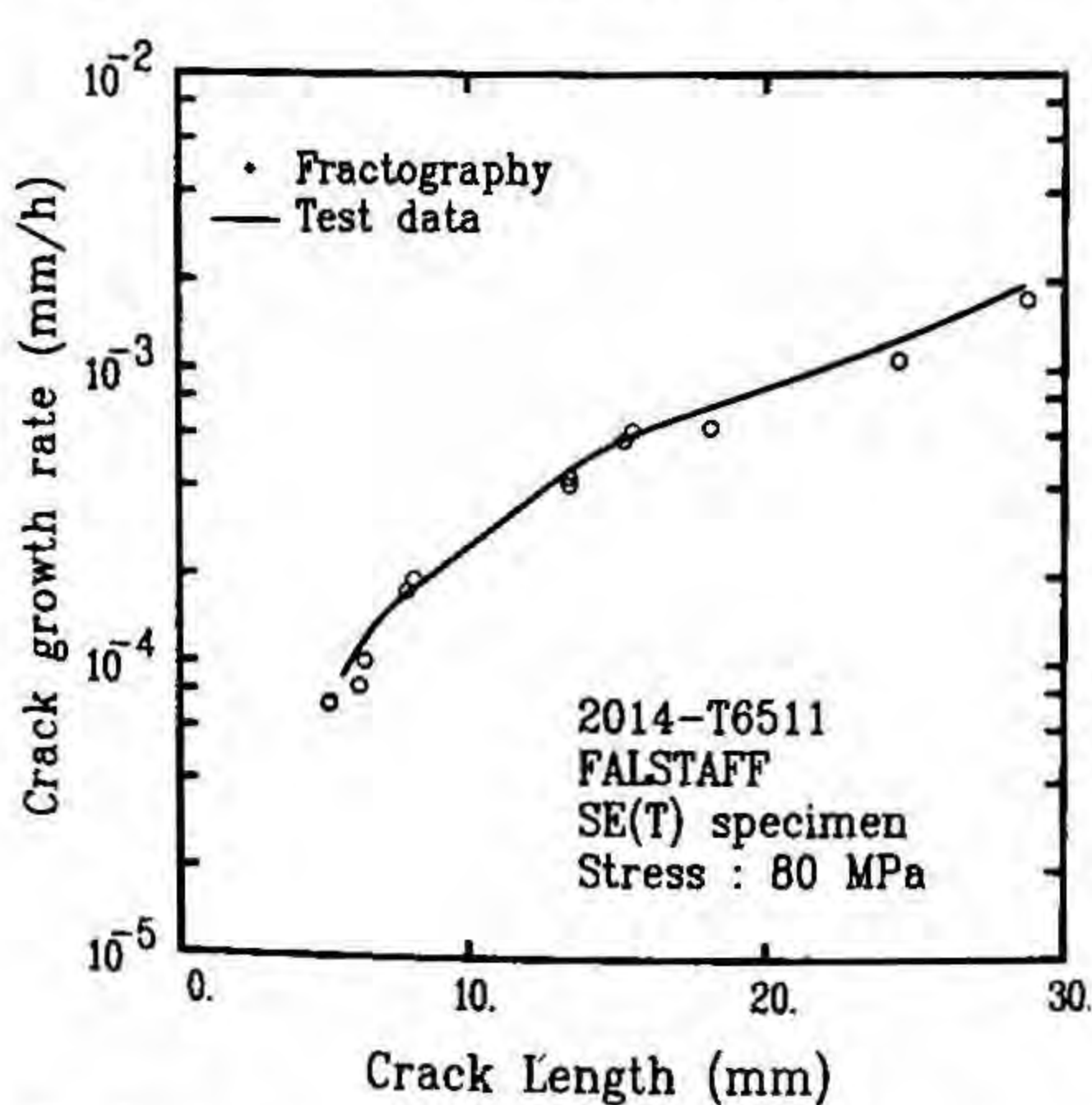


FIG 2b. Crack growth rate estimates from optical fractography compare well with compliance-based computations. Specimen: SE (T) long crack 80 Mpa: Load sequence: Programmed FALSTAFF.

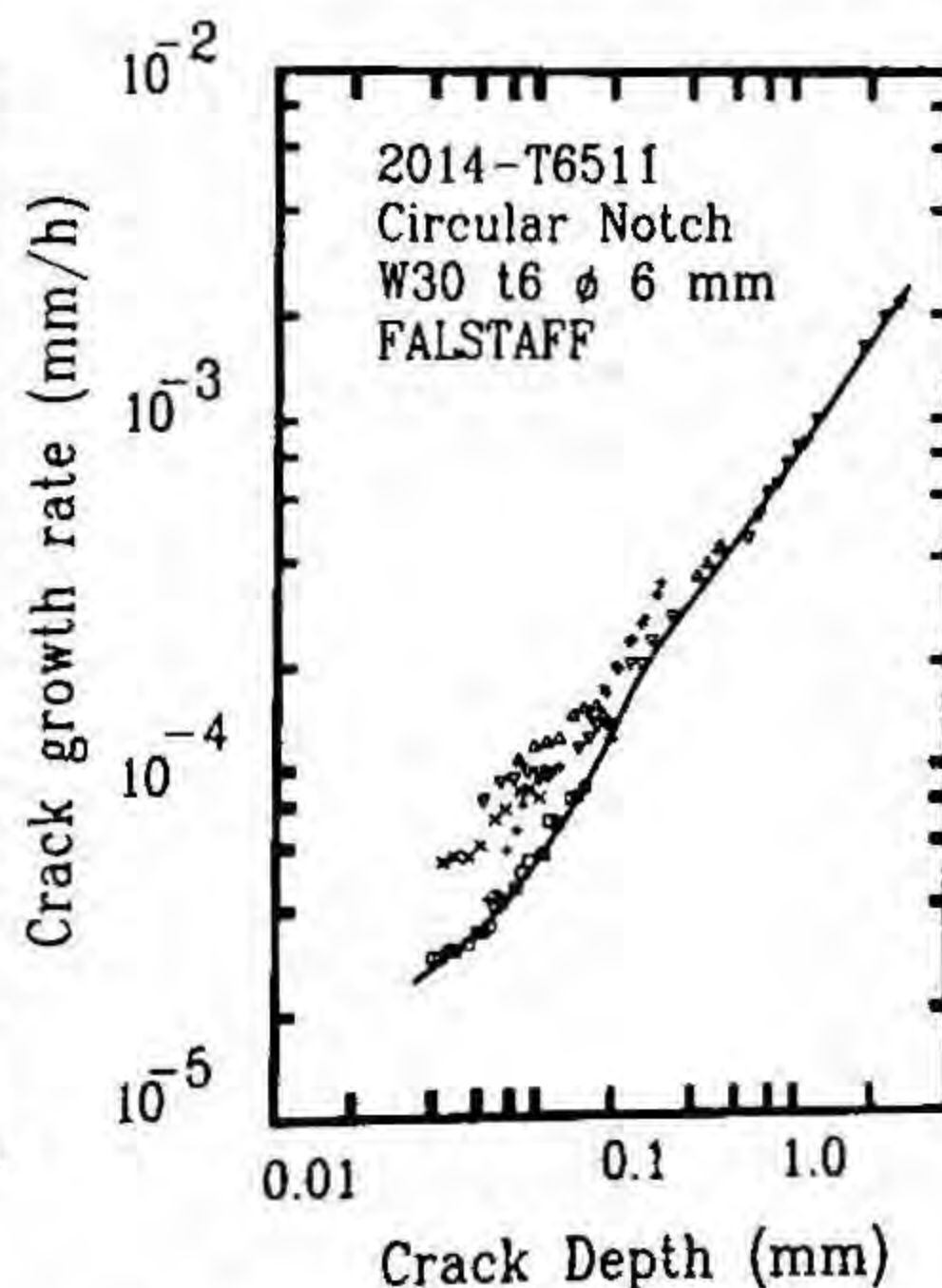
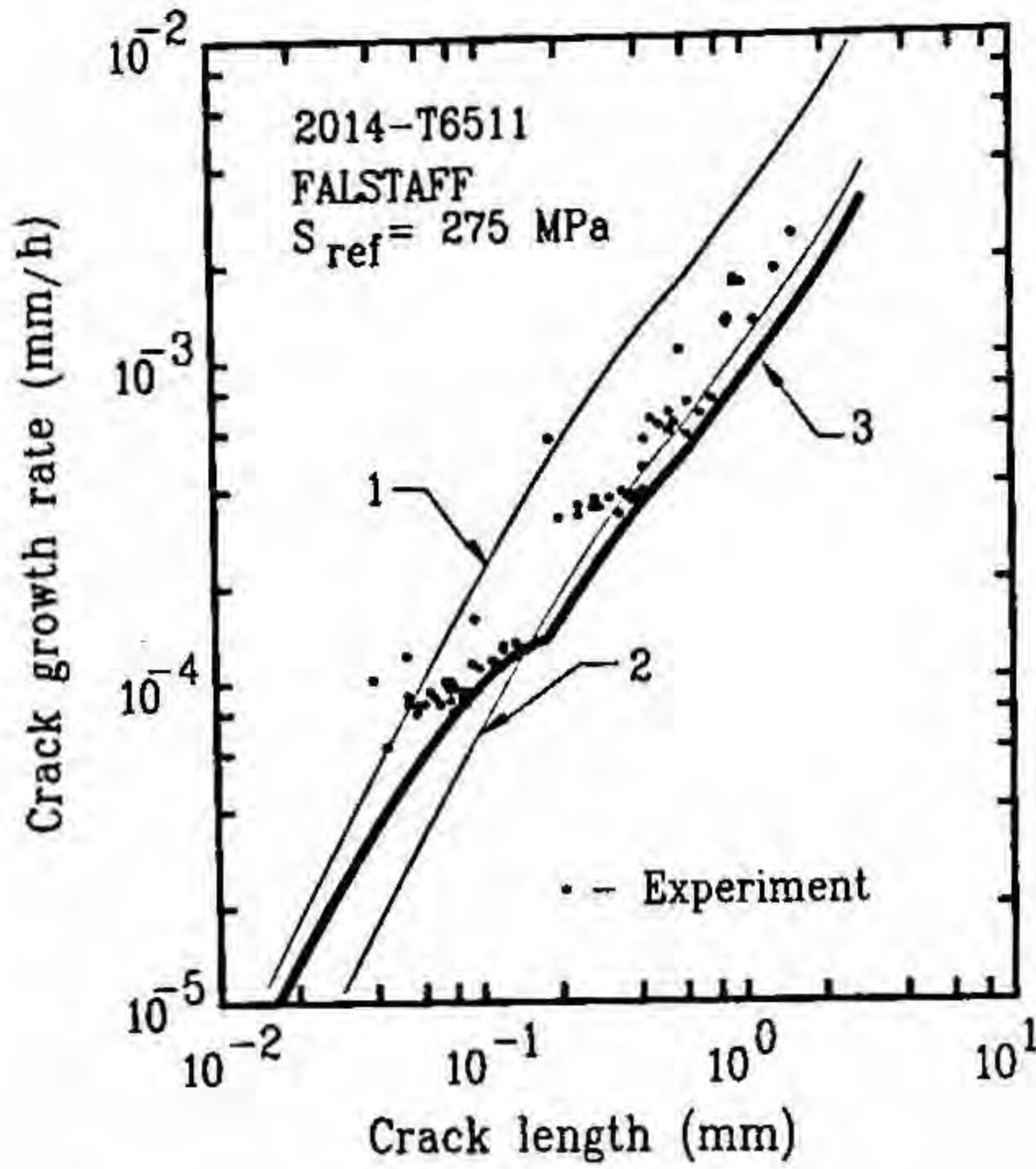
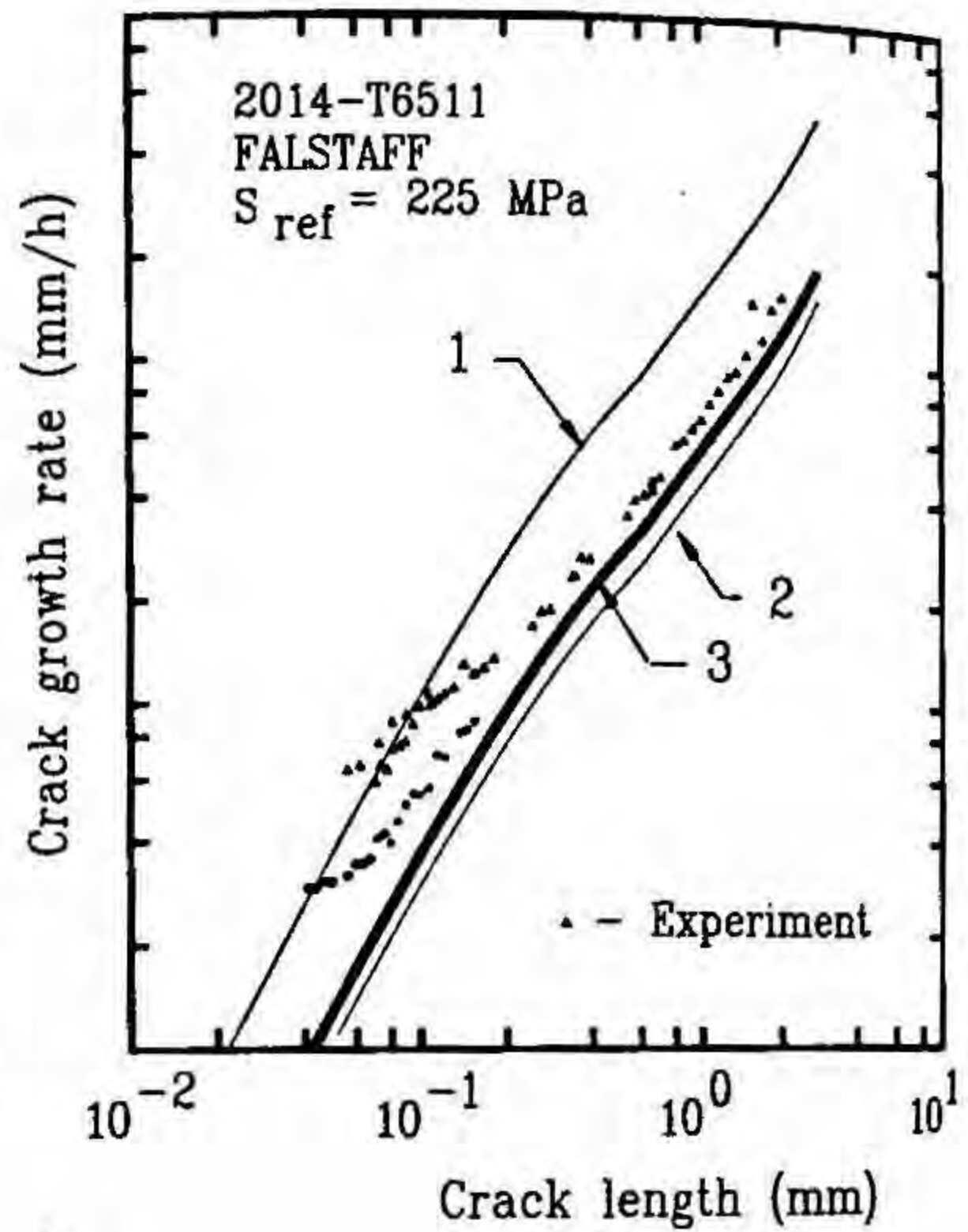


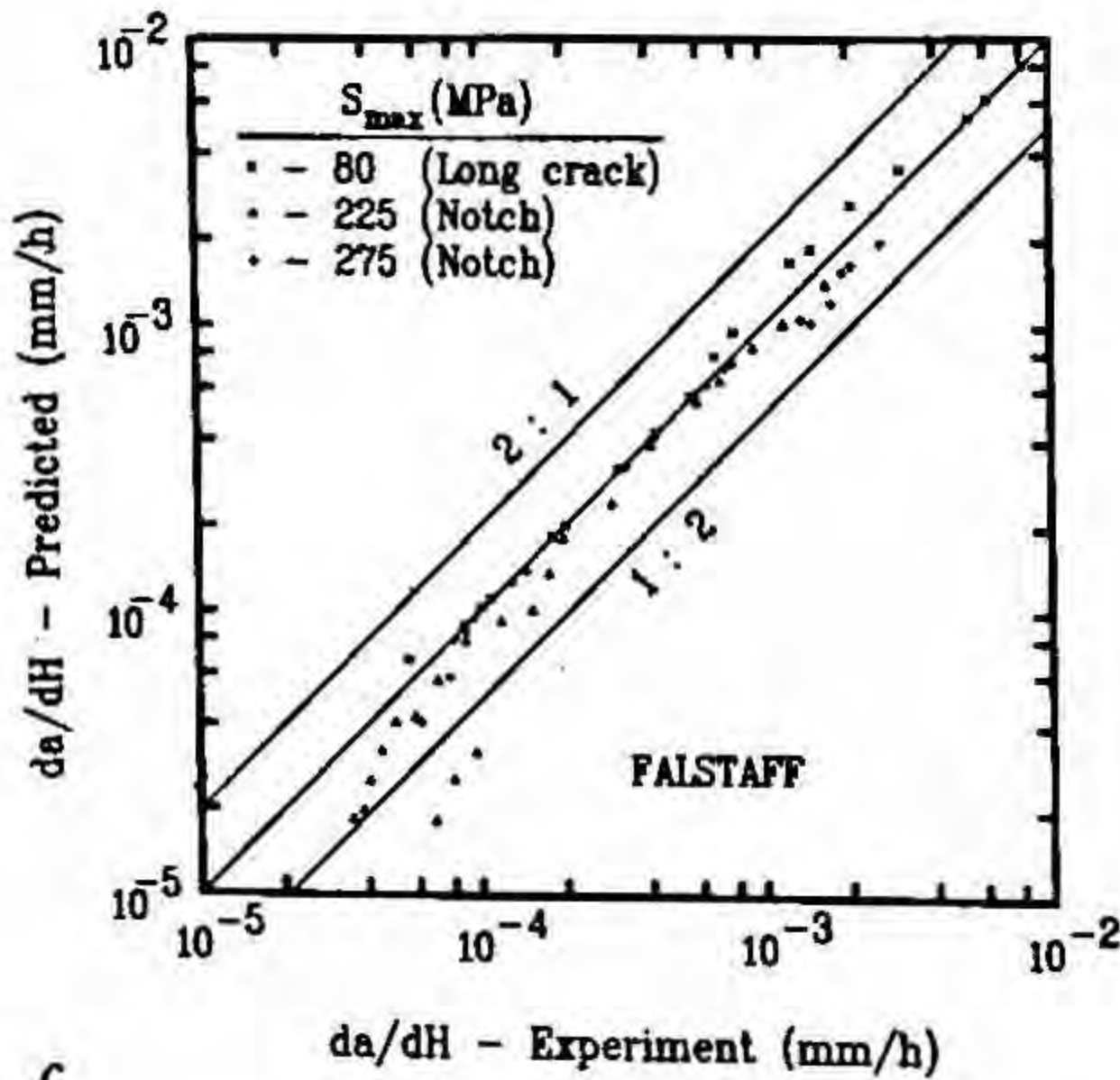
FIG 2c. Growth rate of multiple crack initiators can vary up to a factor of three. Dominant crack initiates first (solid line), but accelerates others.



a



b



c

FIG 3a-c. Notch crack growth rate predictions from hysteretic crack-opening model compare well with experimental data. Conservative estimates used constant crack-opening stress level of -4.0% of S_{max} . The difference between experimental and predicted crack growth rates is within a factor of 2.0 for dominant crack (c).

crack-opening stress data for notch cracks, and material stress-strain properties is capable of predicting crack growth rates for both long and short cracks at notches down to a depth of under $100\ \mu$ for elastic as well as inelastic spectrum loading.

References

1. SUNDER, R. *Notch root crack closure under cyclic inelasticity*, NAL Project Document PD ST 9132, NAL, Bangalore, India,
2. DOWLING, N. E. AND KHOSROVANEH, A. K. *A simplified analysis of helicopter fatigue loading spectra*, ASTM STP 1006, ASTM, Pa, 1989, pp. 150-171.
3. EL HADDED, M. H., SMITH, K. N. AND TOPPER, T. H. *A strain based intensity factor solution for short fatigue cracks initiating from notches*, ASTM STP 677, ASTM, Pa., 1979, pp. 274-289.
4. MILLER, K. J. AND DE LOS RIOS. (EDS) *The behaviour of short fatigue cracks*, EGF Publication 1, 1986, Mechanical Engineering Publications, London.

Thesis Abstract (Ph. D.)

Some investigations on the development of electronic components based on superconducting films by M. V. S. Lakshmi

Research supervisor: M. Satyam

Department: Electrical Communication Engineering

1. Introduction

Electronics industry has been actively engaged in the development of several components based on vacuum, gas, liquid and semiconductors. All these components dissipate a certain amount of power during the active period. Thus there has been considerable effort on the part of the scientists to develop electronic components with minimum energy losses in active state. For this purpose semiconductors based on CMOS circuits have been developed. Even these devices dissipate certain amount of power during the transition from one state to the other. Alternative seems to be the use of superconductivity for this purpose as the superconductors in the superconduction state do not dissipate any power.

In the early part of this century considerable effort has been put in to develop superconducting components like cryotrons, Josephson junctions, etc. All these devices are operated at very low operating temperatures

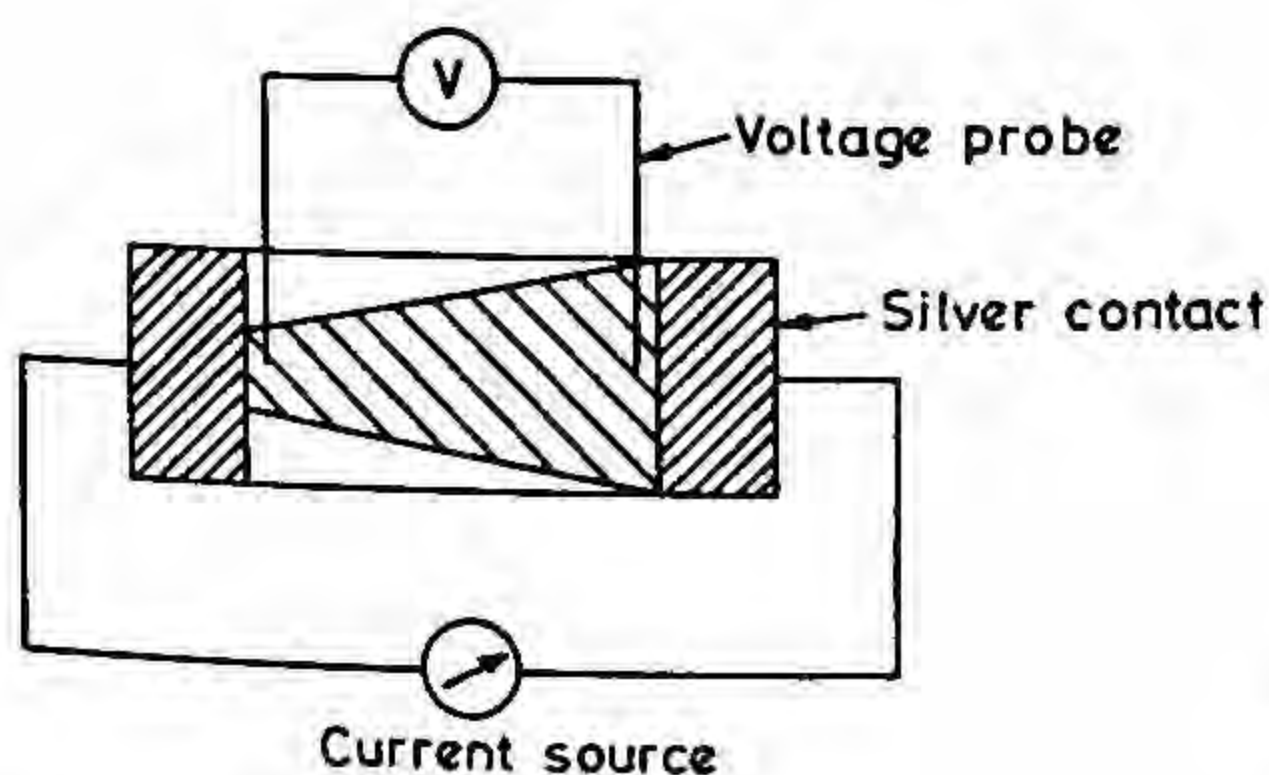


FIG. 1.

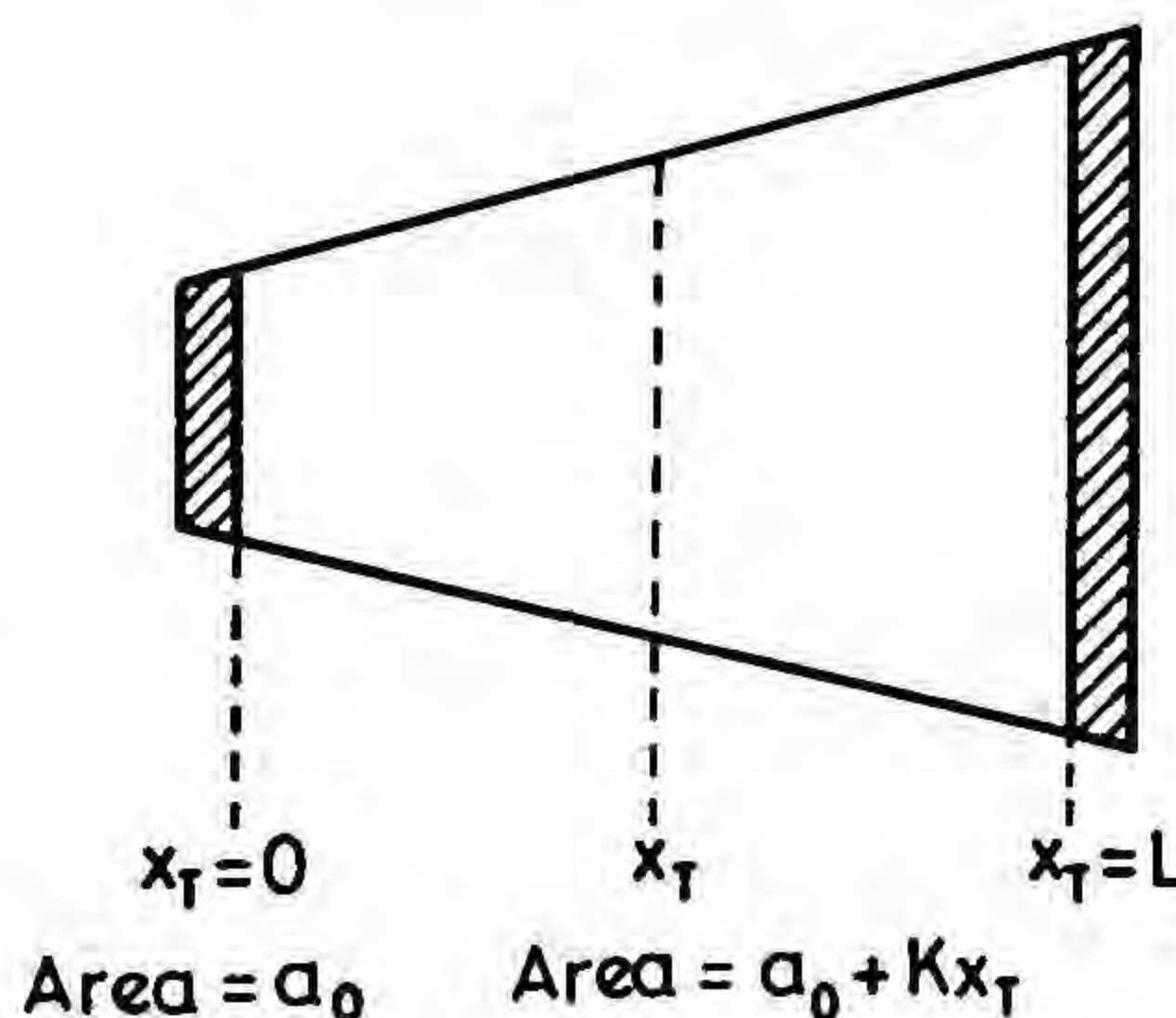


FIG. 2

(max. 23K) and hence the cost of maintenance is high. The recent invention of high T_c superconductors has kindled the hope of making economical superconductor devices. Considerable activity exists to make Josephson junction, cryotrons and allied systems with high T_c superconductors.

This thesis describes the investigations carried out to develop simple electronic components through the use of superconduction films. The problems encountered in realising these components using thick film superconducting films has been discussed in some detail.

2. Experimental work

In the first instance, high T_c superconducting films based on Y-Ba-Cu-O have been prepared on alumina substrates using thick film approach. It has been found that the processing is rather critical and the critical currents are rather low for these films. Through XRD analysis it has been found that the superconductivity is destroyed in these films because of the formation of yttrium aluminate compounds¹. So an attempt has been made to prevent the interaction of alumina with Y-Ba-Cu-O film by providing a silver buffer layer². This effort has helped in realising superconducting films with good critical currents.

On the same lines good superconducting films based on Bi-Sr-Ca-Cu-O have been prepared³. While processing these films it has been found that there exist two phases, one with T_c 80 K and another with T_c 110 K. It has been found that depending on the time of heat treatment either of the phases can be realised.

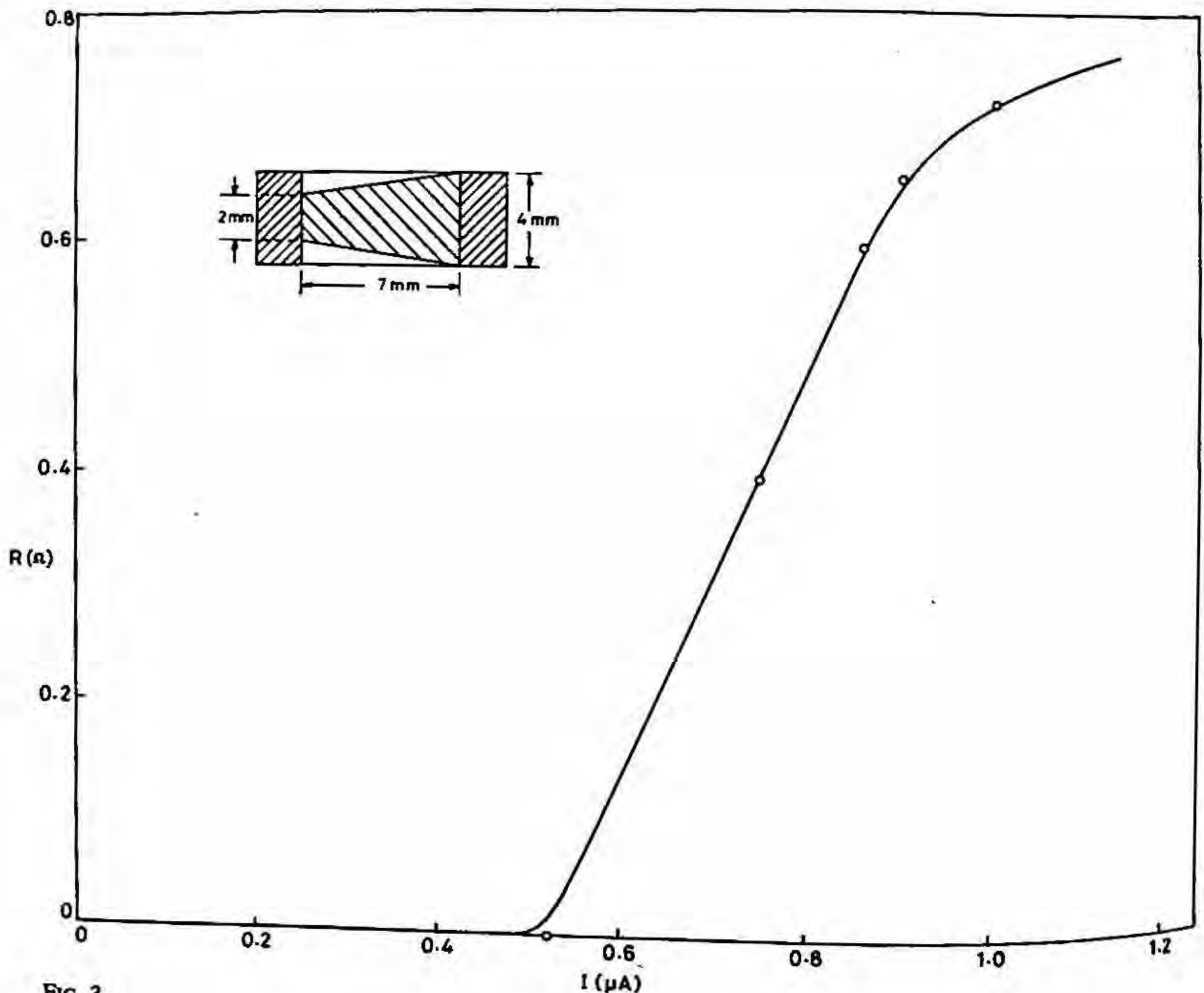


FIG. 3.

3. Principle of operation of electronic components

A broad look at the various existing electronic components reveals that all of them are either two- or three-terminal variable resistors. From the work presented in the thesis, it appears that most of the two-terminal components may be realised through the use of shaped superconductors. This calls for a detailed analysis of the existing components and intelligently choosing the right property of superconductors to get this function.

Using these it has been shown that one can realise components like current-controlled resistor⁴, and wide-range thermal sensor⁵. All these devices are essentially based on shaping the superconducting film to give rise to required characteristics (Figs 1 and 2). In the case of current-controlled resistor depending on the current resistance relation that is needed, the film cross-section is varied. As the current through the film varies depending on the magnitude of the current a certain portion of superconductor becomes resistor and thus the required variation of resistance with current can be achieved (Fig. 3). On the same lines it has been shown that when the temperature varies a certain portion of the film becomes resistive and therefore a thermal sensor with required variation can be realised.

An analysis of the process of clipping has clearly revealed that a change in resistance value of the device is needed at a defined threshold current or voltage. One of the basic properties of a superconductor being, that it becomes a normal conductor beyond a critical threshold current, it had been possible to show that a film of uniform cross-section can be used to perform bidirectional clipping. It has been pointed out that this clipper has two states of conduction corresponding to zero resistance and finite resistance whereas in a normal clipper the two states correspond to finite and infinite resistances.

4. Contacts to high T_c superconducting films

Investigations were carried out on the contacts to high T_c superconducting films from the point of choosing the right material for the contact pads. The various conductors that have been used as contact materials are gold, silver, aluminum and indium. I-V measurements were made on the superconducting films with these contact materials by both two- as well as four-probe measurement method. It has been found that either silver or indium contacts are suitable and for our samples silver has been used.

Thus this work has clearly established the possibility of making electronic components by shaping superconducting films.

References

1. LAKSHMI, M. V. S., RAMKUMAR, K. AND SATYAM, M. On superconducting Y-Ba-Cu-O films prepared by printing on alumina substrates, *J. Phys. D. Appl. Phys.*, 1989, 22, 373-375.
2. LAKSHMI, M. V. S., RAMKUMAR, K. AND SATYAM, M. Role of a silver buffer layer on the superconducting Y-Ba-Cu-O films deposited by screen printing on alumina substrates, *J. Mat. Sci.*, 1991, 26, 4092-4094.
3. LAKSHMI, M. V. S., RAMKUMAR, K. AND SATYAM, M. Superconducting Bi-Si-Ca-Cu-O films prepared by the screen printing technique, *Phys. Stat. Sol. (a)*, 1992, 129, K33-K37.
4. LAKSHMI, M. V. S., RAMKUMAR, K. AND SATYAM, M. A wide range superconductor thermal sensor for low temperature measurement, *Rev. Sci. Instrum.*, 1991, 62, 2792-2794.
6. LAKSHMI, M. V. S. AND SATYAM, M. A bidirectional clipper using superconductors, *Cryogenics*, 1992, 22, 300-302.

Thesis Abstract (Ph. D.)

Performance analysis of scheduling strategies in switching and multiplexing of multiclass VBR traffic in an ATM network by Lillykutty Jacob

Research supervisor: Anurag Kumar

Department: Electrical Communication Engineering

1. Introduction

We study certain novel issues arising in the switching and multiplexing of traffic in ATM (asynchronous transfer mode) networks. In particular, the work is concerned with the performance analysis of various strategies for scheduling cell service in an input queueing, non-blocking, space-division ATM switch and in an ATM multiplexer.

Hui and Arthurs¹, and Karol *et al.*² studied the performance of such an ATM switch with a Bernoulli model for the cell arrival process and each arriving cell independently requesting each output with equal probability. Li³ studied the performance with Bernoulli cell arrivals but nonuniform cell routing. Performance analysis of the switch with a certain correlated input traffic was also investigated by him⁴.

2. Contribution of the thesis

We begin our study on the performance of an $N \times N$ switch by using a simple two-parameter (p and q) Markovian model for the output request process of the arriving cells on each input link of the ATM switch. With this model, geometrically distributed bursts of consecutive cells destined for the same output can arrive at an input; $(1-p)^{-1}$ is the mean burst length. A burst of cells for an output is followed either by a geometrically distributed number of idle slots (mean idle period being $(1-q)^{-1}$) or by a burst of cells for another output. The output for this new burst is chosen uniformly from among the other $(N-1)$ outputs. Motivated by the fact that some input links may receive traffic from metropolitan area networks, and others from broadband-ISDN terminals⁵, we study the situation where there are two classes of inputs with different values of p .

We address an important technical question in the theory, namely, the relation between saturation throughput and stability of the input queues. We show that for each N , the saturation throughput yields a sufficient condition for stability. The saturation throughput of the switch is shown to be equivalent to the throughput of customers in a certain closed queueing network model with N single server stations and N customers. The service times are equal to one slot time on the input links and the servers are synchronous in that their services begin and end at the same epochs. The N customers in the queueing network correspond to the N HOL cells at the N inputs, and the customers queued up at station m , $1 \leq m \leq N$ represent the number of HOL cells that are waiting at their input queues to be switched on to the output m . The class of each customer corresponds to the burstlength parameter p_i of the corresponding input link.

We give an exact analysis of this queueing network *via* the regenerative method, for a 2×2 switch with two traffic classes, and obtain an optimal contention resolution policy which maximizes the saturation throughput. This optimal policy is the shorter-expected-burstlength-first (SEBF) policy, *i.e.*, give priority to the input with the smaller bursts (on the average) when there is an HOL contention, the intuition being that this is more likely to break the contention. An exact analysis of the closed queueing network for finite N except for very small values of N seems to be intractable. Hence we restrict ourselves to the asymptotic analysis ($N \rightarrow \infty$). In the previous studies¹⁻⁴ also, only the asymptotic performance of the switch was analysed. We consider a situation where there are two classes of traffic. A fraction α of the switch inputs carry type 1 traffic with burst length parameter p_1 and the remaining inputs carry type 2 traffic with parameter p_2 . Based on a Poisson assumption for flows in the closed queueing network, as $N \rightarrow \infty$, we obtain explicit expressions for the asymptotic saturation throughput of each class, with priority given to one class over the other when HOL contention occurs. Simulations of finite size switches show that for increasing N the saturation throughput does approach the limit computed by us.

Results from these simulations and asymptotic analyses show that there can be significant throughput advantage if, when several HOL cells contend for the same output, the input with the smaller bursts is given priority. A remarkable finding that we make is that, when there are two traffic classes, giving priority to less bursty traffic gives better throughput than if all the inputs were occupied by this less bursty traffic.

Next we study the impact of the HOL contention resolution policy on traffic delay. We develop cell and burst delay analyses, for the asymptotic case ($N \rightarrow \infty$), with the same traffic model. In particular, we consider the 2 class traffic situation with priority given to one class over the other, and obtain mean burst delays for each class. We compute the burst delay in two steps. In the first step we obtain the probability generating function (pgf) of the HOL contention delay of the burst, *i.e.*, the time from when the leading cell of the burst reaches the head of the

input queue, until the last cell of the burst is transmitted on the output link. In the second step we compute the mean waiting time of a burst at the input queue, *i.e.*, the time from when the leading cell of the burst arrives at the input buffer, until this cell reaches the head of the queue.

For the high-priority traffic, we model the HOL contention delay as the time to absorption in a certain Markov chain. A low-priority HOL cell is selected for transmission only if there are no high-priority HOL cells contending for the same output. We model the HOL contention delay of a low-priority burst as the time to absorption in an appropriate Markov renewal process. Numerical computations are facilitated by truncating the state spaces of these processes; by choosing sufficiently large truncation parameters we make the numerical error due to truncation small.

To obtain the mean burst waiting time at the input queue we model each input queue as a Geom/GI/1 queue. Here each customer corresponds to a burst, and its service time is the HOL contention delay. With the geometric approximation for the burst arrival process at an input queue, we obtain an upper bound for the mean burst waiting time.

We study the delay performance for a finite size switch through simulation. From the asymptotic analyses and simulation results, we make the following important observations. There are combinations of cell arrival rates for the two bursty classes such that while both type 1 (short burst length traffic) and type 2 (longer burst length traffic) input queues are stable with SEBF policy; type 1 queues are unstable with reversed priority. Further, SEBF policy can yield significantly lower mean delay for the short burst length traffic without much effect on the longer burst length traffic. As pointed out earlier, a motivating scenario for our two class traffic model is that the less bursty traffic can be from metropolitan or campus area networks. Such traffic will carry interactive data services, which will have short burst lengths but will be delay sensitive.

Next, in our study, we turn to the analyses of cell service disciplines in an ATM access multiplexer. We model the cell arrival process from each VBR source as an on/off process with exponentially distributed on and off periods. We consider the scenario where there are M statistically identical variable bit rate (on/off) sources multiplexed through low-speed access lines on to a high-speed link. We study two strategies for statistical multiplexing: burst-level multiplexing and round-robin cell level multiplexing. Kumar and Cole⁶ have studied these two strategies for an LAPD terminal adapter for multiplexing SDLC protocol frames arriving over low-speed lines. However, the number of fixed-size LAPD packets yielded by each SDLC frame was assumed to be fixed.

We resort to a fluid flow approximation for analysing the burst-level multiplexer. We assume that the superposition of the arrival epochs of the first bit of the bursts forms a Poisson stream. The bursts, however, do not arrive instantaneously. The server (*i.e.*, the trunk) is allocated to the customers (*i.e.*, the bursts) in an FCFS fashion; once allocated to a burst, the server is deallocated only after the burst has fully arrived and has been fully served¹. We obtain the distribution of waiting time of the first bit of the burst after its arrival at the multiplexer, *via* level-crossing analysis⁷. We perform a simulation of the actual discrete time model to test the validity of the fluid flow approximation and the Poisson assumption.

Since direct stochastic analysis of the round-robin cell-level multiplexing scheme is intractable, and reasonable approximations are as yet unavailable, we resort to a discrete time simulation. We compare this discrete time model with the fluid flow model of Anick *et al.*⁸ Since both the models have work-conserving servers, the two models should have the same total buffer content. As a check on the simulation, and also to study the accuracy of the fluid approximation, we compare the mean total buffer content from both the models. We show that for a low value (≤ 3) of speed ratio between the switch input link and the customer access lines, burst-level multiplexing yields a lower end-to-end mean burst delay. For higher speed ratios round-robin multiplexing yields smaller delays.

Finally, in order to study if the results for the ATM switch obtained from the simple Markovian traffic model hold with more realistic traffic, we simulate an ATM network with an input queueing cell switching hub, and customer access lines being multiplexed into the input links of this hub. Each access multiplexer is fed by on/off sources. Some multiplexers are fed by sources with long bursts, and others by sources with short bursts. At the access multiplexer we use either burst-level multiplexing or round-robin cell-level multiplexing. At the cell

switching hub we use one of the three schemes to resolve the HOL contention: Shorter-Expected-Burstlength-First, Random Selection, or Longer-Expected-Burstlength-First scheme. We find that, for an ATM link to customer access lines speed ratio ≤ 3 , most desirable end-to-end mean burst delay performance occurs when we have burst-level multiplexing at the access multiplexer and SEBF contention resolution policy at the switching hub.

References

1. HUI, J. Y. AND ARTHURS, E. A broadband packet switch for integrated transport, *IEEE J. Select Areas Commun.*, 1987, 5, 1264-1273.
2. KAROL, M. J., HLUCHYJ, M. G. AND MORGAN, S. P. Input versus queueing on a space-division packet switch, *IEEE Trans.*, 1987, Com-35, 1347-1356.
3. LI, S. Q. Nonuniform traffic analysis on a nonblocking space-division packet switch, *IEEE Trans.*, 1990, Com-38, 1085-1096.
4. LI, S. Q. Performance of a non-blocking space-division packet switch with correlated input traffic, *Proc., 1989 GLOBECOM Conf.*, pp. 1754-1763.
5. BYRNE, W. R. *et al.* Evolution of metropolitan area networks to broadband ISDN, *IEEE Commun. Mag.* 1991, 29, 69-82.
6. KUMAR, A. AND COLE, R. G. Comparative performance of interleaved and non-interleaved pipelining in LARD terminal adaptors, *Proc. INFOCOM 1990*, pp. 694-701.
7. BRILL, P. H. AND POSNER, M. J. M. Level crossings in point processes applied to queues: single-server case, *Op. Res.*, 1977, 25, 662-674.
8. ANICK, D., MITRA, D. AND SONDHI, M. M. Stochastic theory of a data-handling system with multiple sources, *Bell Syst. Tech. J.*, 1982, 61, 1871-1894.

Thesis Abstract (M. Sc. (Engng))

Ocean acoustic tomography using the normal mode approach by P. V. Nagesha

Research supervisor: G. V. Anand

Department: Electrical Communication Engineering

1. Introduction

Ocean acoustic tomography (OAT) is a potentially powerful tool for monitoring the ocean on a large scale¹. More specifically, OAT is a method of reconstructing the three-dimensional sound speed field $c(x, y, z)$ in a volume of ocean using the transmission of sound between a set of sources and a set of receivers deployed within or around the area of interest. Several parameters of the received signal fluctuate in response to sound-speed fluctuations in the region through which the signal has travelled. The fluctuations in one of these parameters may be measured at all the receivers, and from these data the fluctuations in the sound-speed field may be estimated.

In this thesis, a technique of low-frequency OAT, based on normal mode approach, is presented for a horizontally stratified ocean. The technique exploits the dependence of modal wavenumbers on the sound-speed profile. A system of linear equations relating sound-speed profile perturbation with the modal wavenumber perturbations can be obtained using first-order perturbation theory. The problem of solving these equations is mathematically ill-posed since the solution is generally neither unique nor stable. Some methods of obtaining acceptable solutions are discussed and numerical results are presented.

2. Problem formulation

Consider a monochromatic source of frequency, $\omega/2\pi$, located in a horizontally stratified ocean with sound-speed profile $c(z)$ and depth h . The acoustic pressure in the far-field region is given by the normal mode solution

$$p(r, z, t) = \sum_{m=1}^M a_m r^{-1/2} \psi_m(z) \exp[i(\xi_m r - \omega t)], \quad (1)$$

where $r = (x^2 + y^2)^{1/2}$ is the range, $\psi_m(z)$ are the mode functions with amplitudes a_m , and ξ_m , the modal wavenumbers. The mode functions are the eigenfunctions of the eigenvalue problem represented by the equation

$$(d^2\psi/dz^2) + k^2(z)\psi = \alpha\psi, \quad k(z) = \omega/c(z) \quad (2)$$

with appropriate boundary conditions at the top and bottom surfaces of the ocean. The wavenumbers ξ_m are related to the eigenvalues α_m of eqn (2) through the relation

$$\xi_m^2 = \alpha_m. \quad (3)$$

A good approximation to the actual sound-speed profile $c(z)$ is provided by the average sound-speed profile $c_o(z)$ for the region, which may be obtained from historical data. The eigenvalues and eigenfunctions corresponding to the profile $c_o(z)$, denoted by α_{om} and ψ_{om} , respectively, can be determined with a high degree of accuracy using numerical methods^{2,3}. The eigenvalues of the actual profile $c(z)$ can be estimated from experimental measurements⁴. The following relation between the sound-speed perturbation $\Delta c(z) = c(z) - c_o(z)$, eigenvalue perturbations $\Delta\alpha_m = \alpha_m - \alpha_{om}$, and unperturbed eigenfunctions ψ_{om} can be obtained using first-order perturbation theory under the assumption that $\Delta c/c \ll 1$ for all z :

$$\Delta\alpha_m = -2\omega^2 \int_0^h (\psi_{om}^2(z) / c_o^3(z)) \Delta c(z) dz, \quad m = 1, 2, \dots, M. \quad (4)$$

3. Solution techniques

3.1. Least-squares minimum-norm solution

We have to estimate $\Delta c(z)$, which is a function of the continuous variable z , using finite data. Equations (4) can be approximated by a system of linear algebraic equations if each integral is evaluated by an N -point Gaussian quadrature formula, where the value of N depends on the degree of smoothness of the integrand, and the degree of accuracy required. The value of $N = 80$ should be adequate to provide a very good approximation in most situations of practical interest, and this value of N is used in all numerical computations presented in this paper. The algebraic equations can be written in matrix form as

$$G X = Y, \quad (5)$$

where G is an $M \times N$ matrix with $M < N$, X , the perturbation vector, and Y , the data vector. If the equations are consistent, there exists infinitely many solutions. Hence, some constraints must be imposed to get a unique solution. In the absence of any meaningful physical constraints, the least-squares minimum-norm (LSMN) solution of eqn (5) should yield a good estimate of $\Delta c(z)$ if $\Delta c(z)$ is small for all z and if data errors are either zero or small. The LSMN solution of eqn (5) is given by

$$X_{\text{LSMN}} = G^\dagger Y, \quad (6)$$

where G^\dagger is the generalized inverse of G . The generalized inverse can be obtained using singular value decomposition (SVD) technique.

If the singular values of G^\dagger are small, the solution given by eqn (6) is unstable since even small errors in the model and/or data get magnified. The problems of instability and sensitivity to data errors can be overcome by using Tikhonov's method of regularization⁵.

3.2. Tikhonov's regularization method.

Let Y be the given data vector, Y_o , the true data vector, and let

$$\|Y - Y_0\|^2 = (Y - Y_0)^T (Y - Y_0) = \delta^2. \quad (7)$$

If the error δ^2 is known, Tikhonov's regularization consists of minimizing the functional

$$F(X, \alpha) = \|G X - Y\|^2 + \alpha \Omega(X), \quad (8)$$

where $\Omega(X)$ is the stabilizing functional and α is the regularizing parameter. The stabilizing functional $\Omega(X)$ is nonnegative and has the property that $X : \Omega(X) \leq d$ (a positive number) is a compact set. The parameter α is chosen such that

$$\|G X - Y\|^2 = \delta^2. \quad (9)$$

The functional $\Omega(X)$ may be chosen to be of the form

$$\Omega(X) = \int \sum_{r=0}^p q_r(z) \|(d^r X / dz^r)\|^2 dz \quad (10)$$

if information about the smoothness of $\Delta c(z)$ is available. In the absence of any a priori information, a good choice is

$$\Omega(X) = \|X\|^2. \quad (11)$$

If $\Omega(X)$ is given by eqn (12), the vector X_r that minimizes $F(X, \alpha)$ is given by

$$X_r(\alpha) = (G^T G + \alpha I)^{-1} G^T Y, \quad (12)$$

where I is the identity matrix. The parameter α is chosen so as to satisfy eqn (10).

4. Results and conclusions

We have considered a shallow ocean of depth 25 m, with a hard bottom. The reference profile $c_0(z)$ has a constant value of 1500 m/s. An 80-point Gaussian quadrature is used to reduce eqn (4) to a system of linear algebraic equations. Figures 1 and 2 show the LSMN reconstructions of two different perturbation

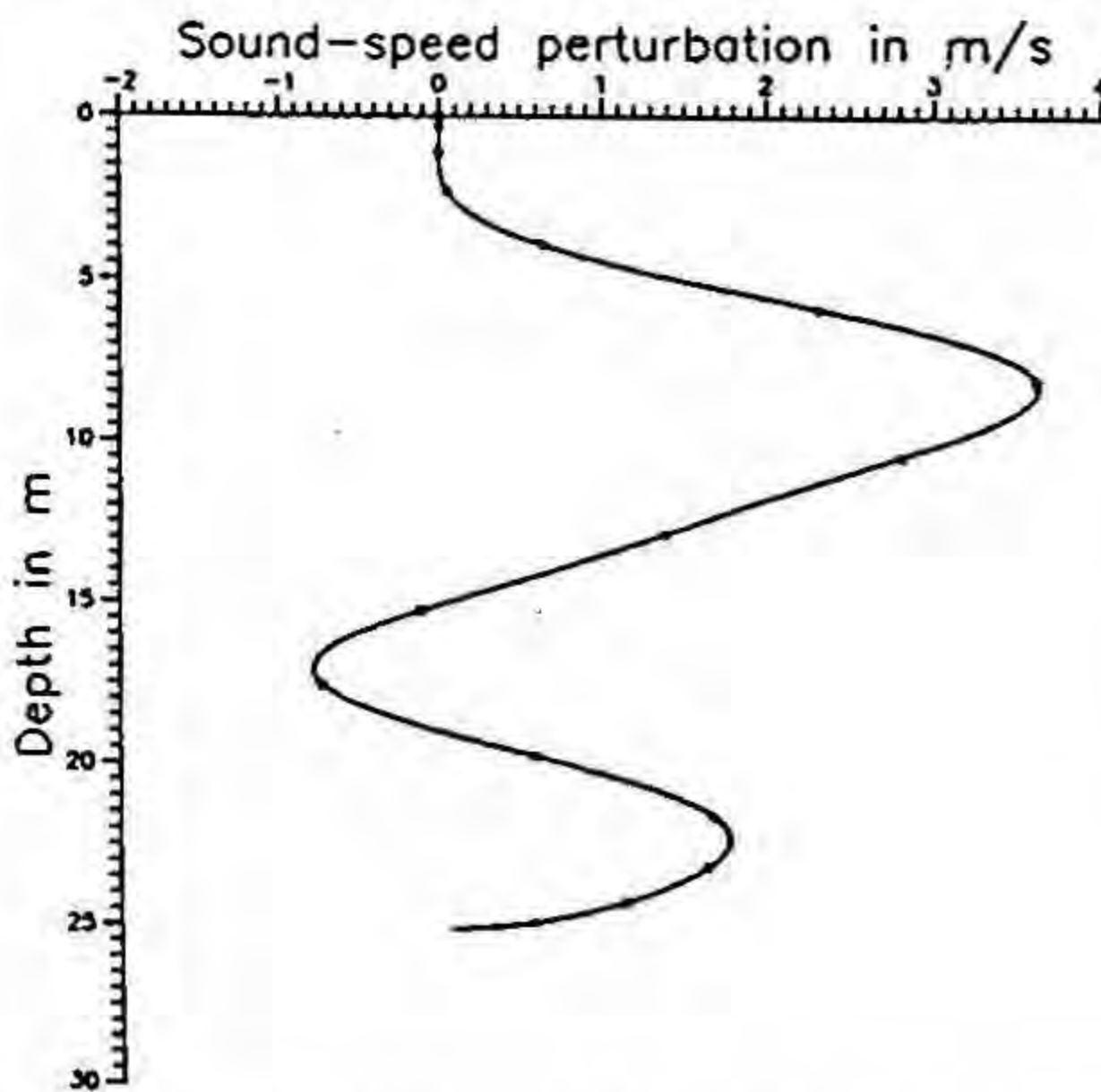


FIG. 1. Actual and estimated profiles of $\Delta c(z)$. —Actual profile, - - -Estimated profile.

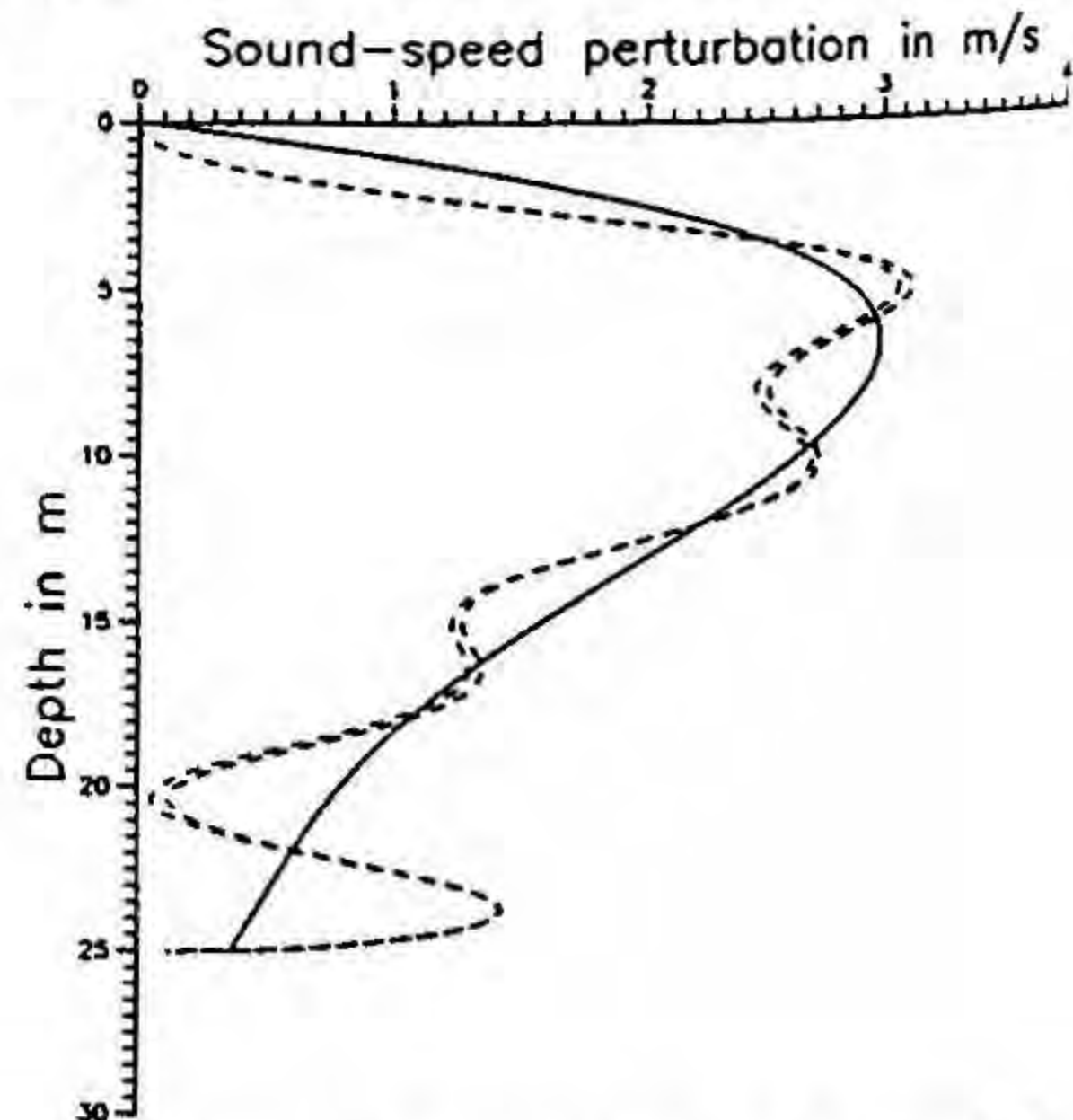


FIG. 2. Actual and estimated profiles of $\Delta c(z)$. —Actual Profile, - - - reconstruction using 4/8 modes.

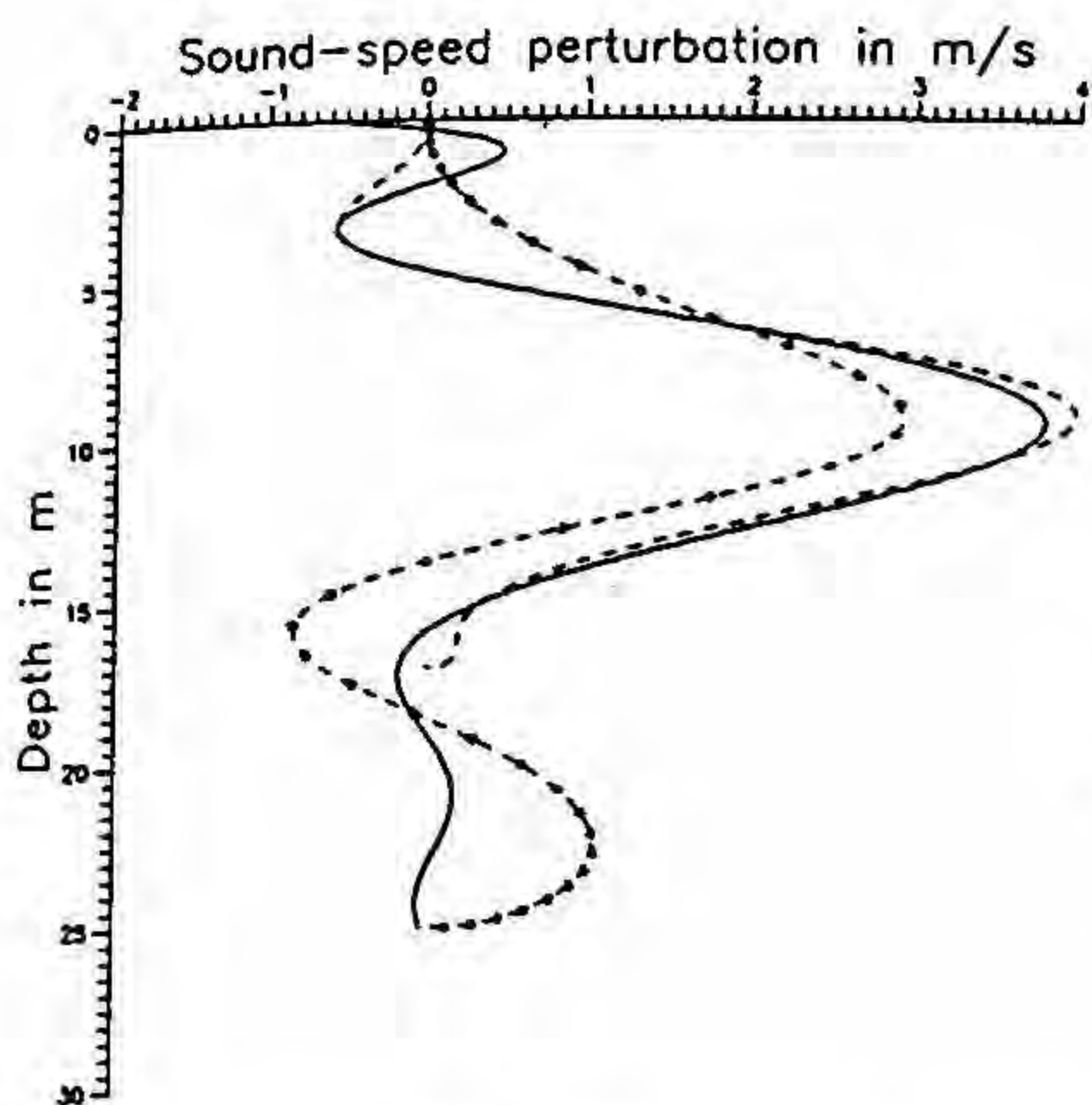


FIG. 3. The effect of a priori information. —Actual profile, -reconstruction without a priori information. - reconstruction with a priori information.

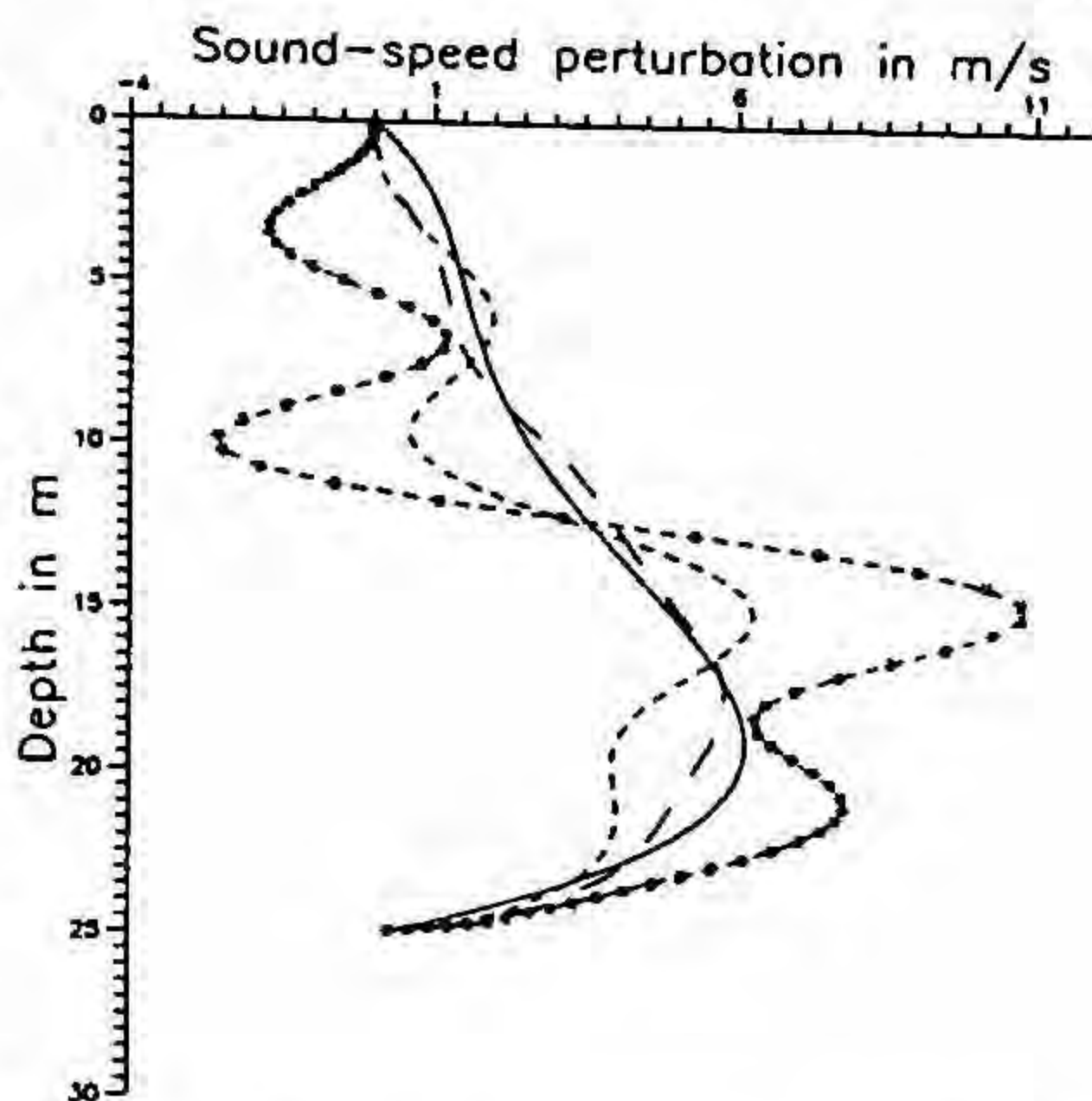


FIG. 4. The effect of regularization. —Actual profile, -Regularized reconstruction using data with 30% Error, -LSMN reconstruction using data with 30% error, - -LSMN reconstruction using error-free data.

profiles $\Delta c(z)$ obtained using the first four modes at frequency of 150 Hz. Though error-free data is used in both the cases, the quality of reconstruction is significantly different. This is so because the reconstruction is good only if the perturbation vector X is in or close to the range of G^T . Another reconstruction, obtained using the first eight modes at 300 Hz, is also shown in Fig.2. There is hardly any difference between the 4- and the 8-mode reconstructions, indicating that increasing the size of the data vector need not lead to a better reconstruction.

However, incorporation of a priori information can lead to a significant improvement in the reconstruction as illustrated in Fig.3. The broken curve with dots in Fig.3 shows the reconstruction of a perturbation profile without using any a priori information, while the broken curve without dots shows the reconstruction of the same profile using the a priori information that $\Delta c(z)$ is negligibly small for $z > 16$.

Figure 4 illustrates the performance of the regularization technique when the data contains large errors. The data error is +30% for modes 1 and 3 and -30% for modes 2 and 4, and it is assumed that the sum of squares of the data error is known. The broken curve with dots in Fig.4 shows the LSMN solution obtained using the erroneous data and the broken curve without dots shows the regularized solution is significantly better than the LSMN solution. The LSMN solution for error-free data is also shown in the figure for comparison.

Numerical results have been obtained for the case of deep ocean also, but these are not reported here due to constraints on space.

Summarizing it can be said that the quality of reconstruction depends on the nature of the perturbation profile, the accuracy of data, and the a priori information available.

References

1. MUNK, W. AND WUNSCH, C. Ocean acoustic tomography : A scheme for large scale monitoring, *Deep-Sea Res. A*, 1979, 26, 123-161.
2. PORTER, M. B. AND REISS, E. L. V. A numerical method for ocean-acoustic normal modes, *J. Acoust. Soc. Am.*, 1984, 76, 244-252.

3. BOYELS, C. A. *Acoustical waveguides: Application to oceanic science*, Ch.4, 1984, Wiley.
4. CHOUHAN, H. M. Normal mode decomposition and its application in ocean acoustics, Ph. D. Thesis, Ch. 5, Indian Institute of Science., Bangalore, 1989.
5. TIKHONOV, A. N. AND ARSEININ, V. Y. *Solutions of ill-posed problems*, English translation, Ch.2, 1977, Wiley.

Thesis Abstract (M. Sc. (Engng))

Supercombinator-based implementation of lazy functional programming languages

by Anurag D. Mendhekar.

Research supervisor: Priti Shankar

Department: Computer Science and Automation

1. Introduction

Graph reduction implementations¹ of functional languages use dynamically created linked structures (graphs) to represent programs. These programs are evaluated by modifying this graph structure according to the reduction rules of λ -calculus. The creation of the nodes of this graph is governed by a run-time storage allocator. Due to the manipulation of the graph structures, many storage cells become inaccessible, *i.e.*, there are no live pointers pointing to these cells. These cells are called garbage cells. It is the responsibility of the storage allocator to collect these garbage cells and make them available for re-use. This reclamation is called garbage collection. Garbage collection is performed at the expense of computation time. Functional programs can be expected to run faster if the overhead of garbage collection is reduced. Supercombinator-based compilation of functional languages is considered to be an efficient way of implementation. In this method, the source program is translated into a form which only uses restricted forms of functions which are called supercombinators². We propose a method to analyse the supercombinator program at compile time and incorporate a run-time mechanism to alleviate some of this overhead.

2. Scope of the work

The work carried out involved the implementation of a G-machine-based implementation of graph reduction, with a front-end for a subset of Miranda, following Peyton Jones³. The implementation was done in Miranda itself. A new technique for potential garbage detection at compile time was proposed and implemented. A brief description of the technique and the results follows.

3. Local and result nodes

Built-in functions invoke recursive calls to the evaluator to evaluate their arguments. The value of the evaluation is returned by updating the root of the graph which the evaluation started with. Typically, in a supercombinator-based implementation such as that based on the G-machine, an evaluation unwinds the spine of the graph, enters the supercombinator at the tip of the spine. The code for this supercombinator builds the graph of the supercombinator with its arguments, updates the root of this reducible expression (the node whose right child is the last argument used by the supercombinator) with the new graph and continues unwinding. The evaluation terminates when the graph being unwound is found to be in weak head normal form (WHNF). This weak head normal form is reached when the supercombinator in the graph is partially applied or the root of the graph is a data object. So an evaluation may be thought of as a sequence of fully applied supercombinators terminating in a partially applied supercombinator or a fully applied built-ins of zero arity.

The code for the supercombinators in this sequence produces some nodes which may be used in further computation. Most importantly, some of these nodes may appear in the result of the evaluation. Such nodes are called *result* nodes of the evaluation. Other nodes, which do not appear in the result, are called the *local* nodes of the evaluation. The locality of the nodes created in the evaluation is affected by the mode in which an evaluation terminates. If the evaluation terminates with a partially applied function, then all the nodes which might appear in this partial application will appear in the result. In case the evaluation terminates with a built-in function, then the semantics of this built-in function determine which of its arguments may appear in the result. For example, both arguments of the built-in function for addition, say '+', will not appear in the result of the evaluation which terminates with '+'. We then say that both arguments of '+' are *local*. On the other hand, the arguments of packing functions like 'CONS', which constructs a data object node with the graphs of its arguments as fields, all appear in the result of the evaluation which terminates with it. Thus, all the arguments of CONS are *result*.

Based on this, we can associate 'blocks' of storage each for the local and result nodes of an evaluation, respectively. When the evaluation terminates, the 'block' of local storage for that evaluation may be freed immediately. These blocks need not be contiguous regions of the store — they may simply be some tags with which the storage allocator can identify the nodes which belong together. A new block may be allocated as a local block for the evaluation when it begins. The result block is the block to which the root of the graph beginning the evaluation belongs. So, if it can be determined whether a node is local to an evaluation or not, we can allocate it in the appropriate block and leave it to the run-time mechanism to free it when the corresponding evaluation terminates.

The task of determining local and result nodes is carried out by the compiler. The compiler analyses the supercombinator program, determines the behaviour of the nodes, with worst case assumptions, and annotates the body with the corresponding locality information. The code generator then uses these annotations to make the portions of the compiled code which request nodes supply the allocator with information about their expected locality. The storage allocator then allocates the nodes appropriately.

In the context of a function, we say that the argument of a function is local to an evaluation if it is not going to appear in the result of the evaluation, and it is result, otherwise. The behaviour of the arguments is referred to as the locality of the arguments of the function.

4. Performing the analysis

The analysis of the supercombinator program is carried out using a least fixed point computation approach. Initially, all nodes are assumed to be local. We iterate over the list of supercombinators with the invariant that we know the annotations to the supercombinator arguments and bodies up to a certain approximation (for built-ins, we use the locality information determined from their semantics as 'pre-knowledge'). At every iteration over the list of supercombinators, we update the locality information of the body of a supercombinator (say S_1) on the basis of the locality of the arguments of the built-in function or supercombinator (say S_2) likely to be entered next in the evaluation in which S_1 participates. This supercombinator or built-in, S_2 , will be entered into only if it is fully applied. If not, the evaluation in which S_1 participates will terminate and the result will be the partial application of S_2 . In this case, we annotate all the nodes appearing in this graph as result. The annotation of any expression in the supercombinator body is always changed only from *local* to *result* and never the other way. Whenever a formal argument appears in an expression that is annotated as result, we update the corresponding locality information of that argument of S_1 . This is done for all the supercombinators in the list.

The next iteration is carried out on the basis of the annotations obtained in the previous iteration. This is repeated till there is no change in the annotations of any supercombinator. The algorithm is guaranteed to terminate because the annotations are always changed in one direction only (from local to result). In the case of higher order functions, it may happen that the supercombinator or built-in to be entered next will not be known at compile time. Then we make the worst case assumption that all the nodes in the arguments of this function will be result nodes. Similar assumptions are made when the body of the supercombinator is a single variable.

Fully applied *if* and *case* functions are assumed to provide alternate paths in the evaluation rather than being supercombinators participating in the evaluation, giving us more than one possibility for the supercombinator or

built-in to be entered next. In such cases, the annotations of the arguments of the supercombinator are fixed, on a worst-case basis, from the annotations obtained from all the possible branches.

5. Pragmatics of the method

This method does claim to guarantee that all the garbage has been collected at a given instant in the execution of the program. It needs to be supported with a conventional garbage collector. The overheads in the method are as follows. There is a one-time cost in allocating the node in the appropriate block. In our implementation, this is just the cost of adjusting three pointers, and initialising the block tag of the node. The cost of freeing a block of nodes is a constant (independent of the number of nodes in the block being freed) and is the cost of adjusting two pointers. However, in case a call to the ordinary garbage collector occurs, some overhead will be incurred to ensure the consistency of the blocks. This overhead is dependent on the implementation and the kind of garbage collector being used. Our implementation needs one more comparison and two more pointer adjustments for every cell reclaimed by ordinary garbage collection. The scanning of the space to look for garbage also needs one more operation. Space overhead per cell, apart from that required by the garbage collector is that of an integer holding the block number to which the node belongs. This can be minimized depending on the maximum expected nesting of evaluations in the implementation. Two pointers are also required for every evaluation which has not yet terminated.

Experimental results have shown that the method works well for largely numerical programs and behaves rather poorly in the case of programs which mostly manipulate data structures. For example, tests on Newton-Raphson's method showed that about 75% of the nodes were cleared automatically tests on a program using both lists and numeric processing (matrix multiplication using lists to represent matrices showed that about 40% of the nodes were cleared by this method. All the local nodes detected for the Quicksort program, however, were eliminated by G-machine optimizations and no advantage was obtained by using this method.

One other aspect of the method is that it can coexist with any of the optimizations used by the code generator to eliminate allocation of nodes. Local-node analysis may be also used to gauge the feasibility of requesting remote evaluations of expressions in parallel implementations of graph reduction on distributed multiprocessors.

References

1. WADSWORTH, C. P. *Semantics and pragmatics of the lambda calculus*, Ph. D. thesis. Oxford, 1971.
2. HUGHES, R. J. M. *The design and implementation of programming languages*, Ph. D thesis, PRG-40, Programming Research Group, Oxford, September 1984.
3. PEYTON JONES, S. L. *The implementation of functional programming languages*. 1987, Prentice-Hall International.

Thesis Abstract (M. Sc. (Engng))

Thermal, mechanical and nondestructive characterization of carbon-carbon composites by A. Ajay Kumar

Research supervisor: Kishore

Department: Metallurgy

1. Introduction

The present and future space-age technology requires high-performance materials which should maintain sufficient strength and stiffness at the ultra-high temperatures encountered especially during the reentry phase, in addition to having a high resistance to thermal shock. Carbon-fiber reinforced carbon (carbon-carbon or C/C) com-

posites offer a formidable combination of the above properties¹⁻³ and hence the characterization of such a material is of importance.

It is well known that the structure of carbon is variable and process-sensitive⁴, which brings into picture the effect of 'process' on the 'properties' of a carbon composite. Hence it is of equal importance to study the effect of fabrication on the composite material properties.

Nondestructive testing of carbon-carbon is of importance owing to their porous nature. For FRPS, the variations in the composition of the material density and porosity content and the presence of anomalies are reported to have a noticeable effect on the ultrasonic wave attenuation⁵. The present investigation, therefore, concerns with the thermal, mechanical and nondestructive characterization of a carbon-carbon composite material.

2. Experimental

Four different process routes were employed to fabricate the composite laminates. Coal tar pitch was used as a matrix precursor to densify the laminates. The effect of pressure during carbonization and of matrix precursor material on the bulk density and on the matrix morphologies formed was investigated.

During the repetitive cycles of impregnation-carbonization, the laminates were periodically checked for bulk density. Scanning microscopic examination was done to identify the morphologies of the matrix. The composite laminates were scanned using the through-transmission ultrasonic C-scan method to assess their integrity by mapping out regions of different attenuation levels on the planar dimensions of the composite laminates.

Mechanical tests were performed with an emphasis to study the effect of specimen orientation (with regards the loading axis). ILSS and in-plane compression tests were done on specimens taken from zones of different (ultrasonic) attenuation levels. The influence of laminate orientation was also investigated in this study both at room temperature and at 925°C. Charpy impact tests were also carried out as per the ASTM standard test procedure.

To study the effect of oxidation on the C/C composites, cubical samples were subjected to oxidation to different levels of burn-off and then tested in compression. Thermogravimetric studies were carried out on cubical and powdered samples at temperatures in the range of 650-850°C to ascertain the rates of oxidation.

3. Results and discussion

3.1. The effect of pressure during carbonization had a significant effect on the bulk density. In about three cycles of (HIP) pressure impregnation-carbonization, the bulk density reached a value equivalent to 10 cycles of atmospheric pressure-carbonization.

The matrix morphologies observed were predominantly lamellar-sheath and leaf-like flakes. It was also observed that pitch as a matrix precursor led to an improved density than the use of phenolic resin precursor which yields nongraphitizing (glassy) carbon.

3.2. The attenuation levels (measured in decibels, dB) plotted over the plane of the laminates gave interesting results. It was clearly established that flaws such as delamination and porosity can be 'healed' in subsequent cycles of densification. The plots also help identify the cut-off cycle of densification.

3.3. Mechanical tests on compression and ILSS samples from zones of different attenuation levels clearly showed the drop in the strength with an increase in the ultrasonic attenuation. This can be explained on the basis that higher attenuation implies significant defect concentration, which in turn leads to a drop in strength. Further, the mode of failure also varied with respect to attenuation levels. Thus a good correlation is seen to exist between nondestructive test data and mechanical properties of the composite.

3.4. Compression tests (both at room temp. and at 1100°K) showed that the strength depended more on the orientation of the composite than on the type of carbon-carbon. Further the ILSS computed from 45° compression tests matched closely with those obtained from the short-beam shear test method. The inplane impact tests gave a higher load and lower (absorbed) energy, while an opposite behaviour was noticed for the interlaminar impact tests.

3.5. Compression tests after burn-off due to oxidation showed a clear drop in strength values with a corresponding increase in the level of burn-off. Thermogravimetric studies showed that specimen geometry and temperature of oxidation had a significant effect on the rate of oxidation. Powdered samples exhibited a higher rate than the bulk ones due to a larger total surface area.

4. Reference

1. STUART M. LEE, (ED). Carbon-carbon composites, pp. 158-187, *International encyclopaedia of composites*, 1990 VCH Publishers.
2. BUCKLEY, J. D. AND EDIE, D. D. *Carbon-carbon materials and composites*, NASA reference publication, RP 1254. p 282, 1992.
3. FITZER, E. The future of carbon-carbon composites, *Carbon*, 25 163-190.
4. BOKROS, J. C. Deposition, structure and properties of pyrolytic carbon. In *Chemistry and physics of carbon*, Vol. 5, 1969. (ed Walker, P. L.), Marcel Dekker.
5. MARTIN, B. G. Ultrasonic attenuation due to voids in fiber reinforced plastics, *NDT Int.*, 1976. 9, 242-246.

Thesis Abstract (M.Sc.(Engng))

Modelling of maneuvering for wheeled mobile robots by R. Balakrishna

Research supervisor: Ashitava Ghosal

Department: Mechanical Engineering

1. Introduction

Wheeled mobile robots (WMRs) are generally modelled as nonholonomic dynamical systems. This arises because the condition for wheel rolling without slip has to be satisfied. The formulation incorporating rolling without slip gives kinematical mappings between wheel rotation and the Cartesian space variables. However, rolling conditions are sometimes violated in tractive maneuvering of WMRs, predominantly due to slipping and scrubbing. To obtain realistic models for maneuvering, the rigid body dynamics of the WMR needs to be used in conjunction with tractive forces that are developed at the wheel-surface contact patch. In this thesis, we present a model for the tractive force in terms of the adhesion coefficient, the linear and angular velocity of the wheel. The dynamic equations of motion are then derived including the effect of the tractive forces. In the work presented here, we include the effects of wheel slip, bearing friction and drive train backlash in the WMR dynamic model. The mechanical configuration of WMRs falls into one of two categories—steered-wheeled and different-drive vehicles. This thesis deals with the latter category¹.

2. Models of the nonlinear effects

2.1. Traction model

The wheel slip, λ , is defined as

$$\lambda = (\theta - v^*) / y \quad (1)$$

where v^* is the wheel linear speed normalised in rad/s¹ and θ , the wheel angular velocity in rad/s. The value of y is when $v^* < \theta$ and is θ when $v^* > \theta$. The relation between the adhesion coefficient, μ_a and wheel slip, λ depends on the nature of the surface and the wheel material. A typical relationship is shown in Fig.1. The curve represents the change in adhesion coefficient, μ_a for acceleration and braking conditions². The tractive force developed, F_t can be written as

¹ $v^* = V/r$, where V is the wheel linear velocity and r , the wheel radius.

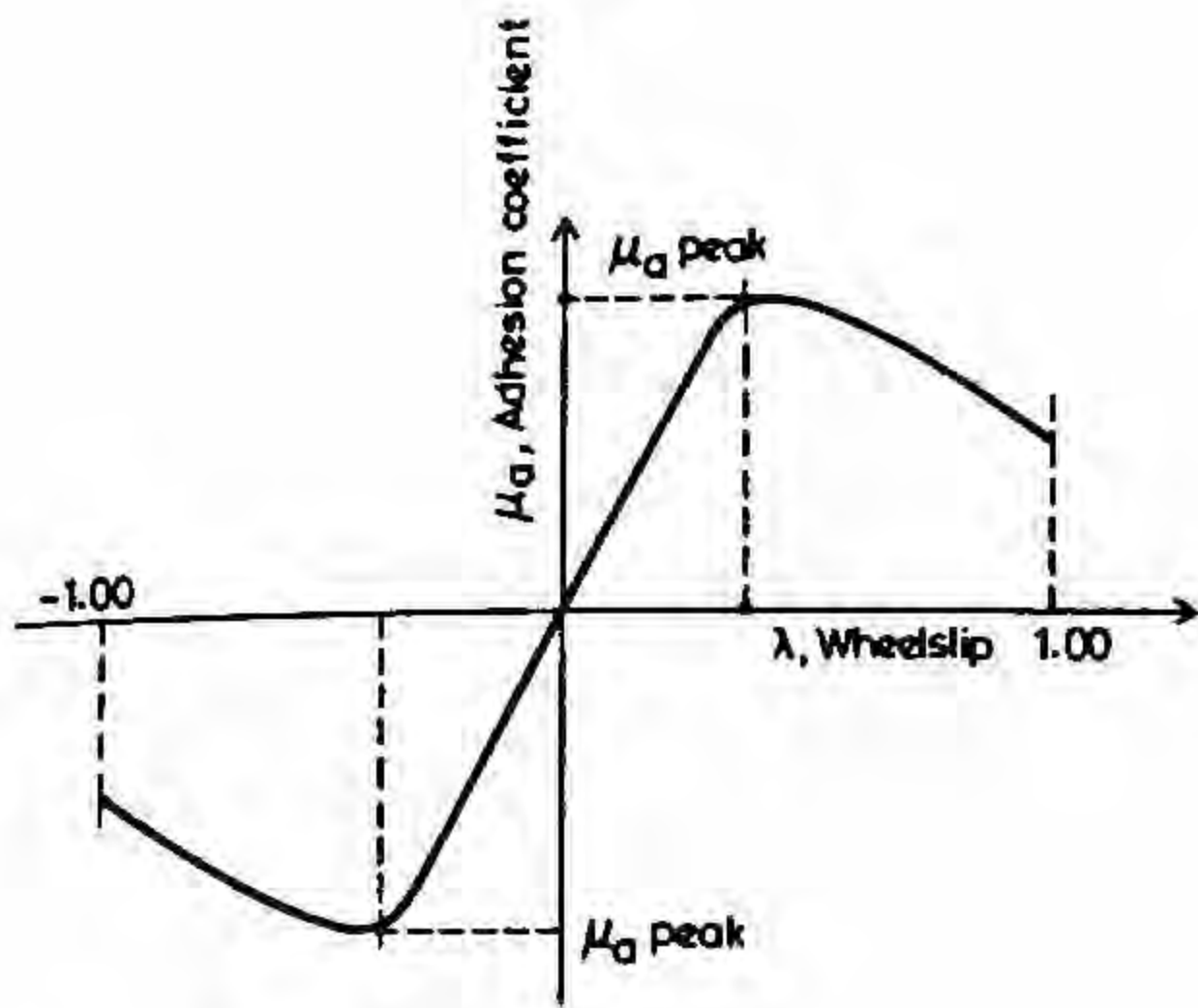


FIG. 1. Traction model.

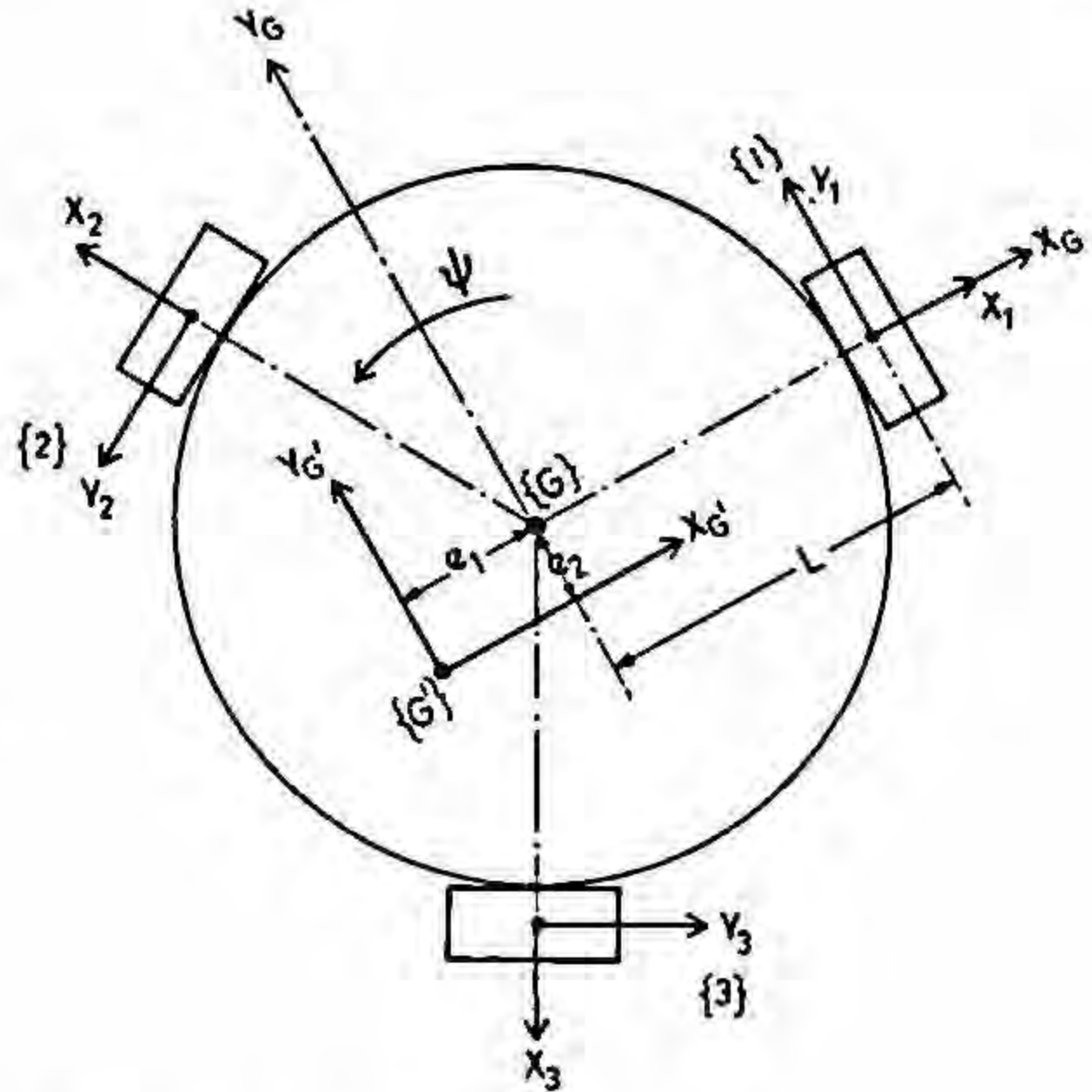


FIG. 2. WMR with co-ordinate frames.

$$F_t = \mu_a(\lambda) N \tag{2}$$

where N is the normal load and we note that $0 \leq |F_t| \leq \mu_{a\text{peak}} N$.

2.2. Bearing friction model

For our simulations, we used a friction model that captures the stiction and slip modes of wheel-bearing sliding friction³. The friction force can be written as a function of wheel angular velocity, θ , as

$$\omega_f = \text{sgn}(\dot{\theta}) \left\{ A_0 + A_1 e^{-\beta_1 |\dot{\theta}|} + A_2 (1 - e^{-\beta_2 |\dot{\theta}|}) \right\} \tag{3}$$

where A_0, A_1, A_2, B_1 and B_2 are constant parameters.

2.3. Backlash model

To represent the motion through a machine element with backlash, three distinct phases are required—detection of rotation direction change, holding the previous output position when the reversed motion is still within the backlash zone and that of setting the output to the new value after the backlash zone has been traversed. This is used to modify the output of the wheel dynamics.

3. Model of the WMR with nonlinearities

The omni-wheel has two degrees of freedom as opposed to conventional wheels which have one degree of freedom. For the WMR with three omni-wheels, shown in Fig.2, one can find the relationship between the wheel velocities, and the Cartesian velocities, by using the no slip condition at the three wheels as in Agullo *et al*¹ $\dot{\theta} = [R]\underline{V}$. When the rolling constraint is not satisfied, the WMR system has six degrees of freedom, $\{X, Y, \Psi\}$ and $\{\theta_1, \theta_2, \theta_3\}$. This is in contrast to the 'ideal' model which has only three degrees of freedom. The dynamic equations of motion for the WMR with the effects of wheel slip are obtained as

$$[M]\underline{\dot{V}} + \Psi [Q] \underline{V} = r [R]^T \{E\} - [R]^T \{f_v\} \tag{4}$$

$$[I] \ddot{\theta} + r \{E\} = \underline{\tau} - \{f_w\}. \tag{5}$$

The traction force model is used to obtain F_t . We incorporate the effects of bearing friction $f_{w_i}(\theta, \dot{\theta})$, $i = 1, 2, 3$ in the joint space dynamics. The effects of backlash are introduced by modifying the output of the dynamic model, and hence do not appear in the equations of motion directly.

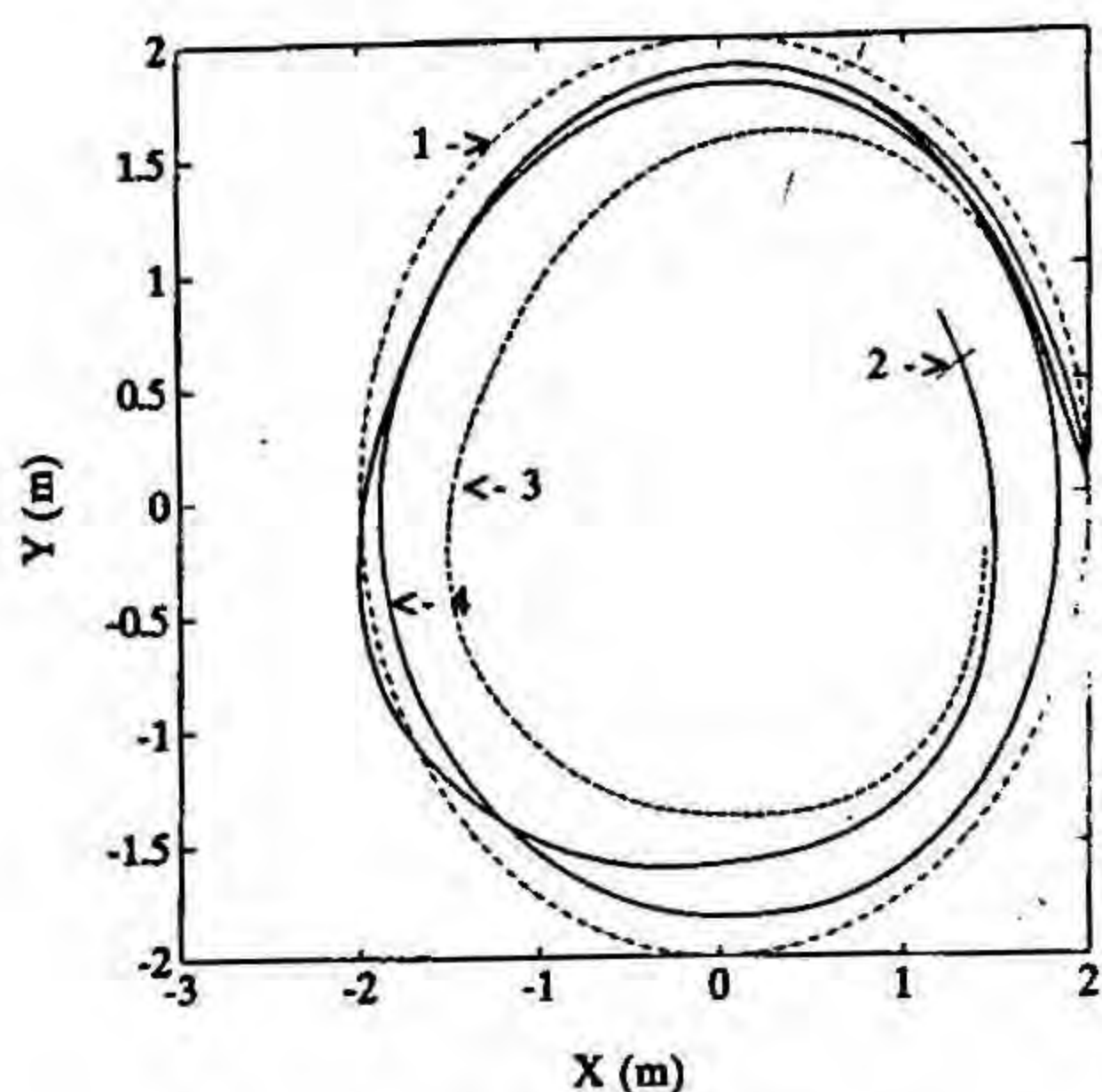


FIG. 3. WMR tracking performance.

Table I
WMR tracking performance

Sl. no.	$\mu_{a_{peak}}$	$R_{error_{max}}$	K_p	K_v	K_i
1	0.80	0.62	1.00	$2\sqrt{K_p}$	0
2	0.80	0.57	1.00	$2\sqrt{K_p}$	0.10
3	0.80	0.17	5.00	$2\sqrt{K_p}$	0

We can make the following observations from the dynamic equations of motion: (a) the individual wheel dynamics are coupled with the WMR dynamics through the tractive forces, (b) the ideal rolling condition is not used, and (c) the wheel torques are the only input to the system.

4. Simulation

The dynamic model of the WMR with the nonlinear effects, eqns 4 and 5, were used in the simulation studies. The WMR dynamic parameters are, $M_p = 50.00$ kg, $I_p = 5.00$ kg m², and $I_i = 2.00$ kg m²,

A model-based control law was used and the gains, K_p , K_v and K_i , are varied and the performance is shown in Fig.3 for a circular Cartesian trajectory of radius 2 m. In the plots discussed here, the bearing friction model (eqn 3), had the parameters, $A_o = 0.50$, $A_1 = 5.00$, $A_2 = 1.00$, $B_1 = 1.00$ and $B_2 = 5.00$. The adhesion coefficient peak value μ_a peak was 0.80. The effects of backlash were neglected. Plot 1 is the reference trajectory. Plot 2 was obtained using $K_p = 1.00$, $K_v = 2\sqrt{K_p}$ and $K_i = 0.10$. Plots 3 and 4 used K_p values of 1 and 5, respectively, with $K_v = 2\sqrt{K_p}$ and $K_i = 0.10$ (Table I). It may be observed that a higher control gain value leads to less deviation.

References

1. DWARAKANATH, S., JAYARAJAN, B. AND GHOSAL, A. Design and fabrication of a mobile robot platform with omnidirectional wheels. *Int. Conf. On Automation, Robotics & Computer Vision (ICARCV'90)*, Singapore, Sept. 18-21, 1990.
2. DUGOFF, H., FANCHER, P. S. AND SEGEL, L. An analysis of tire traction properties and their influence on vehicle dynamic performance, *SAE Trans.*, Paper No. 700377, 1970.

3. CANUDAS DE WIT, C., NOEL, P., AUBIN, A. AND BROGLIATO, B. Adaptive friction compensation in robot manipulators: Low velocities, *Int. J. Robotics Res.*, 1991, 10, 189-199.
4. AGULLO, J., CARDONA, S. AND VIVANCOS, J. Dynamics of vehicles with directionally sliding wheels, *Mech. Machine Theory*, 1989, 24, 53-60.

Thesis Abstract (Ph. D.)

Flow in pipes of uniform and non-uniform cross-section with physiological applications by K. Padmavathi

Research supervisor : A. Ramachandra Rao

Department : Mathematics

1. Introduction

Laminar flow in pipes and channels with uniform and non-uniform cross-sections plays an important role in many engineering and physiological flow problems. Flow of blood through catheterised and stenosed blood vessels are two such applications with intense biomedical and fluid dynamic interest. Catheters are of extensive clinical usage in modern medicine for continuous, accurate and direct measurement of pressure or pressure gradient in blood vessels with less trauma. Insertion of a catheter into a blood vessel increases frictional resistance to the flow and thereby alters pressure distribution in the blood vessels. Understanding the flow structure in a blood vessel in the presence of a catheter helps one to estimate the error in the measurement and also to improve the efficiency in the pressure measurement by minimizing the effect of the presence of the catheter on the flow. The study of the flow in variable cross-sectional pipes provides a deeper insight into the pathology of a proliferative disease of blood vessels called atherosclerosis. In the recent years, the study of flow characteristics in pipes with elliptic cross-section has drawn the attention of the researchers due to its numerous applications. In high heat load systems such as nuclear reactors, compact heat exchangers, etc., one comes across the flow in elliptic pipes. On the other hand, in cardiovascular system, the blood vessels are of elliptic cross-section when the transmural pressure is very low (for example, pulmonary arteries) and in the regions prior to bifurcations¹⁻³.

2. Present study

The present study deals with the mathematical modelling of the flow through stenosed and catheterised blood vessels by considering laminar and fully developed flows in a non-uniform single pipe and in between two non-intersecting cylinders with uniform or non-uniform cross-sections, respectively. In order to theoretically model the catheter movement in a blood vessel we consider the steady flow of an incompressible viscous fluid between two eccentric circular cylinders and two confocal elliptic cylinders in relative motion under the influence of a constant pressure gradient. The inner cylinder is assumed to be moving with a uniform velocity along its axis and blood is assumed to behave like a homogeneous Newtonian fluid which is quite satisfactory in large blood vessels. Exact solutions for the velocity field are presented using bipolar coordinates for eccentric circular cylinders case and elliptic cylindrical coordinates for the case of confocal elliptic cylinders.

The steady and pulsatile flows of an incompressible viscous fluid in an elliptic pipe of slowly varying cross-section are considered to model flow in a stenosed blood vessel. Ideas of lubrication theory are used and the analytical solutions for a low Reynolds number flow are presented. Using the geometric parameter representing slow variation in the cross-section of the tube as a perturbation parameter, solutions at various orders for velocity and pressure gradient are obtained for a flow with a prescribed flow rate. The steady flow in between two confocal elliptic cylinders with a non-uniform outer one and pulsatile flow between two uniform confocal elliptic cylinders are considered to study flow characteristic in catheterised blood vessels with and without stenosis, respectively. To study the pulsatile flow in a single cylinder, the method of solution described for the corresponding steady flow problem is used. An exact solution for the velocity field is presented for the pulsatile flow in uniform confocal elliptic cylinders.

The microstructure of the blood is mechanically significant for flows through small blood vessels (arterioles, venules and capillaries). Thus the flow of blood through small blood vessels is modelled by considering it to be a non-Newtonian fluid such as power law fluid, Cassons fluid, micropolar fluid, couple stress fluid, etc. We consider the steady flow of a micropolar fluid in an elliptic pipe of variable cross-section and pulsatile flow of a micropolar fluid in a channel of variable cross-section in order to model flow in small blood vessels with constriction. The problem of flow in a channel is studied by using rectangular Cartesian coordinates. The method of solution is similar to that described earlier.

The problem of two phase flows modelling the flows of two or more immiscible fluids is of great practical importance in an optimal design of pipes, boilers, partial condenser tubes, etc., in a large variety of engineering applications. In blood flow, the suspensions have a tendency to concentrate in the core of the tube leaving a cell-free plasma layer near the wall. Thus blood flow in narrow tubes is modelled by a two-layered fluid flow with a Newtonian fluid near the walls and a Newtonian fluid of different viscosity or a fluid with microstructure in the core of the tube. The steady flow of two immiscible fluids in an elliptic pipe of uniform cross-section is considered to model the flow through a narrow blood vessel. Two different cases with a Newtonian fluid in the peripheral region and either a Newtonian fluid of different viscosity or a micropolar fluid in the core of the tube are considered. Exact solutions are obtained for velocity field in both the cases. For all the problems considered, the analytical expressions for the physical quantities such as volume flux, wall shear stress, friction factor, etc., are derived.

3. Results and discussion

For each of the problems considered, the structure of the flow is analysed through the numerical computation of the physically significant quantities such as pressure gradient, velocity field, resistance offered to the flow and wall shear stress. For the flow in eccentric circular cylinders, results for the cases of concentric and fully eccentric (*i.e.*, the cylinders have a generator in common) are obtained by taking appropriate limits. Further when the flow is due to pure relative motion, in the absence of the pressure gradient, the volume flux is observed to be maximum when the cylinders are fully eccentric and minimum when they are concentric. This is opposite to the result reported by MacDonald⁴ for the flow due to pressure gradient when the cylinders are at rest. The effect of the ratio of the radii, eccentricity, and the relative motion of the inner cylinder on the flow are discussed. The critical velocity of the inner cylinder for which the flux becomes zero and flow separation are also discussed. For the flow in confocal elliptic cylinders, the results for the case in which the inner cylinder reduces to a strip joining foci are obtained in the limit as the minor axis of the cross-sectional ellipse tends to zero. The effect of the relative velocity of the inner cylinder on the flow is discussed in detail.

For the steady flow in a variable cross-sectional elliptic pipe, there is a decrease in pressure gradient and an increase in axial velocity in order to maintain the constant flow rate. Contribution of nonlinear terms in Navier-Stokes equations becomes more significant for the flows with larger Reynolds numbers and larger area constrictions. Axial velocity, wall shear stress and resistance offered to the flow increase with an increase in the eccentricity of the tube. The steady flow in confocal elliptic cylinders with non-uniform cross-section has similar characteristics to that of the flow in a single non-uniform pipe except that there is an increase in axial velocity, resistance offered to the flow and wall shear stress.

For the pulsatile flow of a Newtonian fluid in an elliptic pipe of variable cross-section and in two uniform confocal elliptic cylinders, the solutions involve modified Mathieu and Mathieu functions with complex arguments. The method of the computation of these functions is discussed in detail. The validity of solutions for low and high values of Womersley parameter is examined. For the flow in a single cylinder it is observed that the pressure gradient decreases and the axial velocity increases with an increase in the value of the Womersley parameter. For the flow in confocal elliptic cylinders, the results for the corresponding circular annulus case are obtained in limit as eccentricity goes to zero. It is observed that there is a decrease in velocity with an increase in Womersley parameter.

The flow structure for both steady and pulsatile flows of a micropolar fluid is similar to the corresponding flow of a viscous fluid except for a relative decrease in pressure gradient and an increase in centreline velocity. The effect of the micropolar parameters such as coupling number, etc., on the flow is discussed. For the two-layered flow in an elliptic pipe, the results for the case of circular cylinder from the results of the first model and

the results of the first model from those of the second model are derived by employing appropriate limits. A reversal of Fahraeus-Lindqvist effect is observed.

References

1. PEDLEY, T. J. *The fluid mechanics of large blood vessels*, 1980, Cambridge University Press.
2. CARO, C. G AND SAFFMAN, P. G. Extensibility of blood vessels in isolated rabbit lungs, *J. Physiol.*, 1965, 178, 193-210.
3. ATTINGER, E. O. Transmission in pulmonary arteries, *Circ. Res.*, 1963, 12, 623-641.
4. MACDONALD, H. M. Fully developed incompressible flow between non-coaxial circular cylinders, *ZAMP*, 1982, 33, 737-751.

